STARS

Electronic Theses and Dissertations, 2004-2019

2017

Multi-axial Thermomechanical Characterization of Shape Memory Alloys for Improved Stability

Douglas Nicholson
University of Central Florida

Part of the Mechanical Engineering Commons

Find similar works at: https://stars.library.ucf.edu/etd

University of Central Florida Libraries http://library.ucf.edu

University of
Central Florida

STARS
Showcase of Text, Archives, Research & Scholarship

MULTI-AXIAL THERMOMECHANICAL CHARACTERIZATION OF SHAPE MEMORY ALLOYS FOR IMPROVED STABILITY

by

DOUGLAS E. NICHOLSON
B.S. Florida Atlantic University, 2008
M.S. University of Central Florida, 2011

A dissertation submitted in partial fulfillment of the requirements
for the degree of Doctor of Philosophy
in the Department of Mechanical and Aerospace Engineering
in the College of Engineering and Computer Science
at the University of Central Florida
Orlando, Florida

Spring Term
2017

Major Professor: Raj Vaidyanathan

ABSTRACT

Shape memory alloys (SMAs) are a unique class of materials wherein shape recovery occurs against external stress by means of a reversible thermoelastic solid state phase transformation typically between cubic austenitic B2, trigonal R and monoclinic martensitic B19' phases. The ability to do work while transforming from one phase to another due to a temperature change enables their use as high-force actuators in automotive and aerospace applications with both sensory and actuation functions. Superelastic NiTi is also of interest due to its successful use in biomedical devices such as stents. Both R-phase and martensite can detwin, reorient and undergo a thermal or stress induced transformation. For these reasons, it is difficult from ordinary macroscopic measurements to decouple elastic and inelastic contributions (from their respective phases) from the overall deformation. *In situ* neutron diffraction is ideally suited to probing these microstructural and micromechanical changes while they occur under external stress fields.

Despite SMAs typically operating under multi-axial stress states in applications, most previous *in situ* neutron diffraction based investigations on SMAs have been limited to homogenous stress states as a result of uniaxial loading. The current investigation spatially maps thermoelastic deformation mechanisms during heating and loading of shape memory and superelastic NiTi by recourse to *in situ* neutron diffraction, performed at Oak Ridge and Los Alamos National Laboratories. SMA spring actuators were also used to experimentally validate the ability of a recently developed model to predict the evolutionary deformation response under multi-axial loading conditions.

By recourse to *in situ* neutron diffraction martensite variant structures were tracked during isothermal, isobaric, and isostrain loading in shape memory NiTi. Results show variant structures were equivalent for the corresponding strain and more importantly, the reversibility and equivalency was immediately evident in a variant structure that was first formed isobarically but then reoriented to a near random self-accommodated structure by isothermal deformation. Variant structures formed isothermally were not significantly affected by a subsequent thermal cycle under constant strain.

During uniaxial/torsional loading and heating, thermoelastic deformation mechanisms in non-uniform states of stress in superelastic NiTi were spatially mapped. The preferred selection of R-phase variants formed by variant reorientation and detwinning processes were equivalent for the corresponding strain (in tension and compression) and the selection of such variant structures was reversed by isothermal loading. R-phase variant selection was consistent between uniaxial and torsional loading when the principal stress directions of the stress state were considered (for the crystallographic directions considered here). R-phase variants were tracked and the similarity in general behavior between uniaxial and torsional loading, in spite of the implicit heterogeneous stress state associated with torsional loading, pointed to the ability of the reversible thermoelastic transformation in NiTi to accommodate both stress and strain mismatch associated with deformation.

Overall, various thermomechanical combinations of heating and loading sequences in SMAs yielded the same final texture (preferred selection of variants), which highlights the ability to take different paths yet still obtain the desired actuator response while minimizing irrecoverable deformation mechanisms. Based on the ability to obtain a texture for a given strain

after varying loading and heating histories, it can be inferred that the results presented in this dissertation could be obtained by following any sequence of loading and heating over multiple cycles. Therefore, the loading and heating path which minimizes the activation of irrecoverable processes and most efficiently produces the desired response should be considered in the design and fabrication process of SMA actuators and superelastic devices. Such loading and heating paths have implications for minimizing the number of cycles required to train an SMA, which limits the amount of work required for stabilizing their evolutionary response thereby increasing the fatigue life and overall durability of the SMA. This finding is valuable to the aerospace and medical device industries where SMAs find current application.

ACKNOWLEDGMENTS

I would like to express my deep gratitude to my advisor Dr. Raj Vaidyanathan for mentoring me throughout every step of both my masters and doctoral experience. His advice and guidance have proven to be invaluable in making me the person and engineer I am today. My gratitude is extended to Dr. Seetha Raghavan, Dr. Jeffrey Kauffman and Dr. Linan An for their contribution to this dissertation by serving on my committee.

I would also like to express gratitude to

- Drs. Ron Noebe, Santo Padula II and Othmane Benafan (formerly at UCF) at NASA Glenn Research Center (GRC), for their guidance and mentoring. Special thanks goes to Santo Padula II who could have practically been considered a co-advisor on my dissertation.

- Dr. Don Brown, Dr. Bjørn Clausen and Thomas Sisneros at Los Alamos National Laboratory (LANL) and Dr. Ke An, Dr. E. Andrew Payzant, Dr. Jeff Bunn and Harley Skorpenske at Oak Ridge National Lab (ORNL), for helpful technical discussions and experimental help.

 - Drs. Dayakar Penumadu and Robin Woracek at the University of Tennessee Knoxville, for helpful technical discussions and assisting with diffraction experiments.

- Jim Mabe and Tad Calkins at The Boeing Company who, more recently, have been mentoring me in applying the skills I developed in graduate school, to the aerospace industry.

Finally and above all I would like to thank my loving wife Kelci, as well as my parents, family and friends for, their love and support, always being there for me and for their encouragement to make it through this important step in my life.

TABLE OF CONTENTS

LIST OF FIGURES

LIST OF TABLES

LIST OF ACRONYMS/SYMBOLS

A_f	Austenite finish
A_s	Austenite start
FEM	Finite element method
GRC	Glenn Research Center
GSAS	General Structure Analysis System
HTSMA	High temperature shape memory alloy
IPF	Inverse pole figure
LANL	Los Alamos National Laboratory
LCT	Lower cycle temperature
M_f	Martensite finish
M_s	Martensite start
MRD	Multiples of random distribution
NiTi	Nickel-Titanium (alloy)
NRSF2	Neutron Residual Stress Mapping Facility
SMA	Shape memory alloy
SMARTS	Spectrometer for Materials Research at Temperature and Stress
UCT	Upper cycle temperature

CHAPTER ONE: MOTIVATION AND ORGANIZATION

1.1 Motivation

The overall objective of this work is to facilitate the engineering of stable SMAs for aerospace and biomedical applications by improving the fatigue life and durability of such alloys. Towards this goal, a set of carefully designed neutron diffraction experiments were performed wherein the evolving texture, phase fractions, and lattice strains can be determined during loading and heating of shape memory and superelastic NiTi. The lattice strain, texture and phase fraction evolution captured *in situ* at stress and temperature under operating conditions using neutron diffraction can provide insight into the phase transfromation and associated deformation mechanisms in these alloys.

The first part of this dissertation seeks to investigate various thermomechanical combinations of heating and loading sequences in SMAs that yield the same final martensite texture (preferred selection of variants), which highlights the ability to take different paths yet still obtain the desired actuator response while minimizing irrecoverable deformation mechanisms. These sequences will be presented in the context of their implications on minimizing the number of cycles required to train an SMA, which limits the amount of work required for stabilizing their evolutionary response thereby increasing the fatigue life and overall durability of the SMA.

Specifically, results show the variant structures were equivalent for the corresponding strain and more importantly the reversibility and equivalency was immediately evident in a variant structure that was first formed isobarically but then reoriented to a near random self-accommodated structure by isothermal deformation. Therefore, the loading and heating path

which minimizes the activation of irrecoverable processes and most efficiently produces the desired actuation response may be obtained through methods proposed here. Such implications would directly benefit the actuator design and fabrication process.

In most applications a SMA typically operates under a multi-axial stress state, however most previous *in situ* neutron diffraction based investigations have been limited to uniaxial loading. Thus, the second set of experiments seeks to track deformation mechanisms in non-uniform states of stress during multi-axial loading of superelastic NiTi by recourse to both conventional and newly developed 3D resolved [1, 2] *in situ* neutron diffraction techniques. Results showed a fully-reversible, (i) thermally-induced phase transformation between the cubic B2 austenite and trigonal P3 R-phases between room temperature and 45°C in the unloaded condition and (ii) stress-induced phase transformation between the R-phase and monoclinic B19' phases during isothermal tensile loading (up to 500 MPa) at room temperature. The presence of the R-phase can significantly alter the overall behavior of the SMA. The R-phase, like martensite can detwin, reorient and undergo a thermally or stress induced transformation. For these reasons, it is difficult from macroscopic measurements to decouple elastic and inelastic contributions (from respective phases) to the overall deformation.

Furthermore, the R-phase has not been extensively studied when compared to the martensite and austenite phases. A better understanding of the R-phase can even aid in the development of R-phase actuators (e.g., Ref. [3]). Experimentally measured strains correlated well with the single crystal Bain strains calculated from crystallographic theory for this alloy and allowed for the identification of specific R-phase variants. Experimental observations of reorientation/detwinning in the R-phase agreed well with predictions of variant conversion in

respective R-phase variants (up to 200 MPa). From these results it can be inferred that the R-phase to B19′ transformation can be utilized as effectively as the more commonly used B2 to B19′ transformation, in superelastic devices. Given that the R-phase has the ability to reorient and detwin, the R-phase to B19′ transformation has the potential benefit of reduced stress and strain mismatch often observed between B2 and B19′ during transformation. Reducing stress and strain mismatch between respective phases could reduce the formation of plasticity formed during cycling through the phase transformation and extend the lifecycle of superelastic devices.

Specific R-phase variants were tracked and spatially resolved measurements in the principle stress, radial and hoop directions during uniaxial and torsional loading (up to 500 MPa) were obtained. The ability to track specific R-phase variants in principle stress directions offered hiterto unexplored insight into preferred selection of variants in SMAs during multi-axial loading. As discussed above, variant selection has a direct implication on stabilizing SMA behavior, specifically the similarity in general behavior between uniaxial and torsional loading, in spite of the implicit heterogeneous stress state associated with torsional loading, pointed to the ability of the reversible thermoelastic transformation in NiTi to accommodate both stress and strain mismatch associated with deformation. All aforementioned efforts have the added benefit of improving the fundamental understanding of thermomechanical deformation in shape memory and superelastic alloys. These findings are valuable to the aerospace and medical device industries where SMAs find current application.

1.2 Organization

The content of this dissertation consist of a compilation of papers divided into chapters and is organized in manner that supports the aforementioned motivation, as follows.

Chapter 2 provides and introduction to; SMA actuators and superelasticity; and the neutron diffraction instruments and data analysis, used in this dissertation.

Chapters 3 and 4 present application relevant case studies of SMA actuators operating under multiaxial conditions in complex forms. Specifically,

Chapter 3 presents the use of SMA spring actuators to experimentally validate the ability of a recently developed model to predict the evolutionary deformation response under multi-axial loading conditions.

Chapter 4 demonstrates heating and loading the paths to optimize the performance of trained SMA torsional actuators. This chapter serves to establish connections between torsional SMA actuators designed for application and neutron diffraction results to be presented in later chapters.

Chapter 5 investigates asymmetry and control mode effects in polycrystalline shape memory NiTi investigated by performing *in situ* neutron and synchrotron x-ray diffraction during reverse mechanical loading and constant strain thermal cycling.

Chapter 6 builds connections between isothermal and isostrain loading results presented in Chapter 5. Furthermore, the results are extended to include isobaric loading, thus providing a comprehensive investigation of texture evolution of SMA under general isobaric, isothermal and isostrain loading paths.

Chapter 7 transitions from the investigations of B19′ martensite in shape memory NiTi (in previous chapters) to R-phase in superelastic NiTi, wherein R-phase like B19′ can reorient, detwinn and undergo a phase transformation. Specifically, Chapter 7 provides an investigation of the R-phase during stress- and temperature-induced phase transformations.

Chapter 8 tracks and spatially maps specific R-phase variants (identified in Chapter 7) in the principle, radial and hoop directions under hetereogenous states of stress, during torsional loading.

Chapter 9 provides a summary of the conclusions from each chapter in a manner that highlights the impact of this dissertation.

CHAPTER TWO: INTRODUCTION

This chapter provides an introduction to shape memory alloys (SMAs) which includes their use as actuators and superelastic properties. The second section in this chapter provides an introduction to in situ neutron diffraction and the diffractometers and tools that were used in investigations throughout this dissertation.

2.1 Shape memory alloys

2.1.1 Shape Memory Alloy Actuators

Shape memory alloys (SMAs) have the ability to recovery their predeformed shape against external loads thus enabling work output in actuator applications. With recoverable strains exceeding 4%, near equiatomic NiTi has been the most extensively used system for SMA actuator technologies thus far. In shape memory NiTi the recovery process occurs by way of a reversible thermoelastic martensitic phase transformation from a monoclinic (B19') martensite phase to a cubic (B2) austenite phase [4-6]. The ability of SMA to recover a pre-deformed shape is often referred to as the shape memory effect. Figure 2.1 illustrates the one-way shape memory effect.

During cooling under no-load from A to B the transformation from the parent cubic austenite phase to martensite produces a self-accommodated martensite variant structure [5]. Isothermal loading from B to C has been well studied [5, 7, 8] and can be partitioned into multiple loading regimes of different moduli (indicated by the vertical dashed red lines in Figure 2.1) with corresponding dominant deformation mechanisms: (I) elastic deformation with limited detwinning and variant conversion; (II) martensite variant reorientation and detwinning; and (III) elastic deformation of detwinned and reoriented martensite. Following elastic unloading from C

to D at D the system remains deformed and the martensite remains reoriented and detwinned. Upon isobaric heating from D to A under no-load the detwinned and reoriented martensite transforms back to austensite producing shape recovery.

The shape memory effect can occur against external load (up to 500 MPa) thus producing work output. The ability to do work while transforming from one phase to another due to a temperature change enables their use as high-force actuators in automotive and aerospace applications with both sensory and actuation functions. This behavior is often referred to as load-biased two-way shape memory effect or isobaric loading (thermal cycling under constant load). Figure 2.2 illustrates a typical isobaric response observed in SMAs. Figure 2.2 shows the transformation temperatures associated isobaric load as determined by the intersection of lines tangent to the heating and cooling curves. The transformation temperatures A_s, A_f, M_s and M_f are the austenite start, austenite finish, martensite start and martensite finish, respectively.

Prior to isobaric loading the SMA is typically loaded isothermally below the M_f to the desired stress. This stress is typically within region I or II (as shown in Figure 2.1) to prevent or minimize the onset of irrecoverable mechanisms during thermomechanical cycling. After isothermal loading, the stress is held constant while the SMA is heated to above A_f which produces a transformation strain (or recoverable strain) associated with the shape recovery against the external load. Finally, the SMA is cooled below the M_f and the original strain or shape is recovered. There is often irrecoverable strain associated with this process. Deformation mechanisms contributing to irrecoverable strain have generally been attributed to the accumulation of retained martensite (i.e., martensite existing above the A_f), dislocation based plasticity and/or deformation twinning [8-10].

7

Residual strains can be reduced or eliminated by appropriate training processes, thus producing a stable SMA actuation response [5-7, 11, 12]. SMA training typically involves performing multiple isobaric cycles under the applied load of the intended application. During this process residual strain accumulates with each cycle and increasingly saturates until desired stability is achieved. The number of cycles required to train varies between alloy systems and is dependent on the processing history performed prior to training [5, 6]. Training can also be achieved by appropriate isothermal deformation [7]. Stabilization of the isobaric response by training and processing is generally attributed to the preferential selection of martensite variants (texture), internal stress fields generated by plasticity, the formation of precipitates and/or deformation twinning.

Two-way shape memory behavior observed under isobaric loading can also occur under no-load (as demonstrated in Figure 2.2) and is often called intrinsic two-way shape memory. Intrinsic two-shape memory effect is generally attributed to internal stress fields generated by plasticity, the formation of precipitates and/or deformation twinning [7] which bias the selection of martensite variants (texture) during the phase transformation. Intrinsic two-way shape memory effect often forms during training and is observed when thermal cycles are performed following the removal of the load used to train.

2.1.2 Superelasticity

As described in the previous section, SMAs produce the shape memory effect by way of a temperature induced phase transformation. The stress induced phase transformation observed in SMAs is often called superelasticity. Superelastic NiTi has been successfully commericalized for biomedical applications including endovascular stents, orthodontic wires and for eye glass

frames, among others. In NiTi, this phase transformation typically occurs between cubic B2, trigonal P3 and monoclinic B19', phases commonly referred to as austenite, R-phase and martensite, respectively. Furthermore, both the R and martensite phases can accommodate deformation by reorientation and detwinning of P3 [13-15] and B19′ variants, respectively. Figure 2.3 illustrates superelasticity in SMAs. Typically, superelasticity occurs when the SMA is above the A_f otherwise full recovery will not be obtained. Loading from A to B produces up to 8% strain as cubic B2 austenite or R-phase transforms to stress induced martensite. Upon unloading from B to A, stress induce martensite transforms back to cubic B2 austenite or R-phase and the strain is fully recovered. Irrecoverable strain can occur during a superelastic cycle which can be reduced or eliminated during training. Similar to training of an SMA actuator (see Section 2.1), training of superelastic SMA can be achieved by repeated cycling. During training of superelastic SMA, isothermal cycles are performed between austenite and martensite until the desired stability is achieved.

2.2 Neutron Diffraction

In situ neutron diffraction during multi-axial loading and heating of SMA is utilized extensively to meet the objectives provided in the previous chapter. Neutron diffraction imaging provides an attractive alternative to electron and x-ray based techniques in which penetration depths can be limited to at most several microns below the surface. The increased penetration depth of neutrons (up to several centimeters) allows for microstructural and micromechanical characterization representative of the bulk of polycrystalline materials. Furthermore, *in situ* neutron diffraction can provide residual and internal strain, texture and phase fraction information during heating/cooling and loading. This section provides an overview of the

neutron diffraction instruments and data analysis used and an overview the specific experiments performed during this investigation.

2.2.1 SMARTS and the VULCAN engineering diffractometers

This investigation will include the use of "time-of-flight" neutron diffraction at the Spectrometer for MAterials Research at Temperature and Stress (SMARTS) at Los Alamos National Laboratory and the VULCAN engineering diffractometer at the Spallation Neutron Source (SNS) at Oak Ridge National Laboratory (ORNL). Figure 2.4 shows the diffraction geometry used at both SMARTS and VULCAN. At both SMARTS and VULCAN the loading axis forms a 45° angle with the incident neutron beam. Two detector banks are positioned at opposing 90° angles relative to the beam which allows for reflections from lattices planes perpendicular and parallel (denoted as longitudinal and transverse, respectively, in Figure 2.4) to the loading axis to be captured. At both instruments *in situ* loading and heating is accomplished by a servo-hydraulic load frames and an induction heating system, respectively. During uniaxial loading macroscopic strain measurements were made by extensometry (10 mm gauge length and strain resolution of $5x10^{-5}$).

VULCAN has the unique capabilities of axial/torsional loading and increased flux. The high flux and continuous scanning available at VULCAN allow for microstructural evolution during the phase transformation to be captured [16, 17]. Recently, an axial/torsion gripping system specifically for VULCANs load frame was created and initial neutron diffraction measurements on NiTi under torsional loading were made [18].

2.2.2 Neutron Residual Stress Mapping Facility (NRSF2)

A portable axial/torsion electromechanical load frame developed by the University of Tennessee, Knoxville (UTK) will be utilized at the Neutron Residual Stress Mapping Facility (NRSF2) at the High Flux Isotope Reactor (HFIR) at ORNL. As opposed to VULCAN and SMARTs which use "time-of-flight" diffraction, the reactor based NRSF2 uses monochromatic neutrons and the Bragg scattering angle (2θ) is varied to observe reflections from specific crystallographic directions. Further details regarding the experimental setup can be found in.[1]The small diffraction volumes ($0.5 \times 0.5 \times 0.5$ mm^3) achievable at NRSF2 allows for spatially resolved measurements in heterogeneous stress states that develop under torsional loading. Furthermore, the unique ability to change the orientation of the axial/torsion load frame relative to the incident beam and detector bank at NRSF2 provides the opportunity to diffract from crystallographic planes with plane normals near the directions of maximum normal stress (two-dimensional planes $\pm45°$ relative to the longitudinal direction) during torsional loading (e.g., in Ref. [1]). Figure 2.5 shows possible diffraction geometries at NRSF2 with the portable axial/torsion load frame in a cross-section of the cylindrical specimen. Figure 2.5a shows the loading direction a vertical position relative to the incident beam. In this configuration, a spatial resolution of 0.5 mm w.r.t. the radius can be obtained. Reflections are from lattice planes parallel to length of specimen and reflections from the radial and hoop directions can be decoupled (as illustrated in Figure 2.5a).

Figure 2.5b shows a cross-section of a cylindrical specimen with the loading axis tilted 43° about the x-axis. Note, ideally the loading axis would be tilted to 45° to observe reflections from lattices planes perpendicular to principle stress directions under torsional loading. In this

configuration, a spatial resolution of 2.0 mm w.r.t. the radius can be obtained. Reflections are from lattice planes 43° to length of specimen and reflections from the maximum and minimum principle directions of stress under torsional loading can be decoupled (as illustrated in Figure 2.5b).

2.2.3 Data Analysis

Residual and internal strain, texture and phase fraction information obtained by recourse to *in situ* neutron diffraction are observed qualitative in diffraction spectrum as follows. Figure 2.6 shows a representative peak shift, broadening and intensity change in a neutron diffraction spectrum acquired from reflections from specific crystallographic direction. Peak shifts indicate lattice strain and changes in peak intensity indicate changes texture or phase fraction. Peak broadening can indicate the presents of lattice defects, elastic anisotropy, twinning, instrument and strain broadening [19], among others.

In order to provide quantitative information, single peaks from a diffraction spectrum (as shown Figure 2.6) are fit with a Gaussian or Lorentzian profile function or a convolution of both resolved by Windor, Jorgens and Von Dreele which is implemented via General Structure Analysis System (GSAS) software [20, 21]. The peak location (d-spacing) d^{hkl}, peak intensity I^{hkl} and Full Width Half Max (FWHM) from the fit are used for further analysis. Lattice strain ε_{hkl} for a specific crystallographic *hkl* plane can be obtained as follows:

$$\varepsilon_{hkl} = \frac{d^{hkl} - d_0^{hkl}}{d_0^{hkl}} \tag{3.1}$$

in which d_o^{hkl} and d^{hkl} are the initial d-spacing and d-spacing measured at a specific temperature, stress or spatial location within the sample, respectively.

In order to obtain strain, phase fraction and texture information representative of a complete neutron diffraction spectrum the spectrum are analyzed using Rietveld refinement implemented by GSAS [21]. Using a least square approximation a theoretical line profile is generated to fit a diffraction spectrum or set of diffraction spectra. Rietveld refinement varies texture, phase fraction and lattice parameters until a "least squares fit" with the measured spectrum is obtained. Using the following mathematical model for the intensity Y_c at every point in the measured spectrum

$$Y_c = Y_b + \sum_h SKF_h^2 P(\Delta T_h) \tag{3.2}$$

where Y_b is the background intensity, S is the scale factor, K is a correction factor containing a description of the changes in predicted intensity due to texture, F_h is the structure factor and $P(\Delta T_h)$ is the profile function dependent on ΔT_h the profile point from the reflection position. Up to an 10th order spherical harmonic description was implemented in the Rietveld refinement code in GSAS. To obtain volume fractions at SMARTS and VULCAN rietveld refinement is performed with phase volume fractions constrained to be equal between both detector banks (i.e., spectra acquired from lattice planes perpendicular and parallel to the length of the sample). Inverse pole figures (IPFs), which represent the distribution of a selected direction in the specimen relative to the crystal axes in multiples of random distribution (1 corresponding to random distribution), can be generated from the Rietveld refinements as previously outlined [20] and plotted with generic mapping tools [22].

13
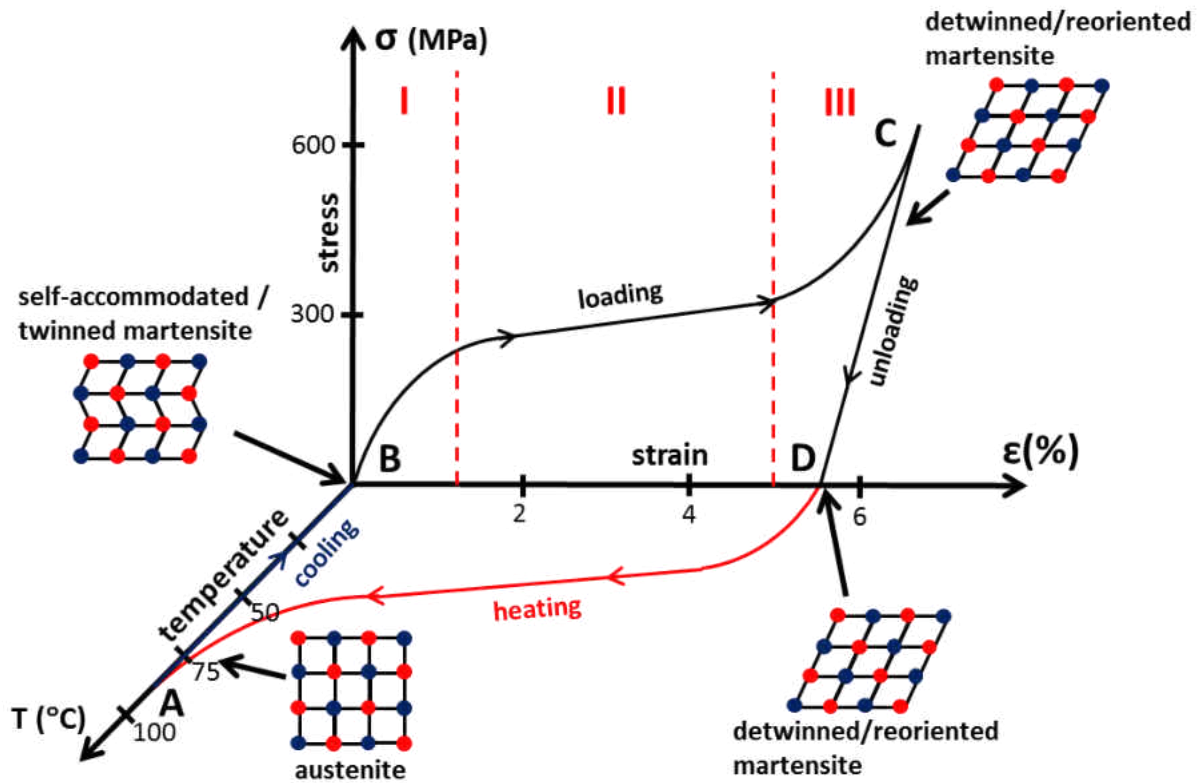
Figure 2.1: Stress-strain-temperature response of shape memory alloy showing the shape memory effect: (A to B) isobaric cooling from cubic austenite to self-accommodated martensite under no-load; (B to C) isothermal deformation of martensite by; region I - elastic deformation of self-accommodated martensite, region II – martensite variant reorientation and/or detwinning and region III – elastic deformation of detwinned/reoriented martensite; (C to D) elastic unloading of martensite; and (D to A) heating from detwinned/reoriented martensite to austenite producing shape recovery under no-load.
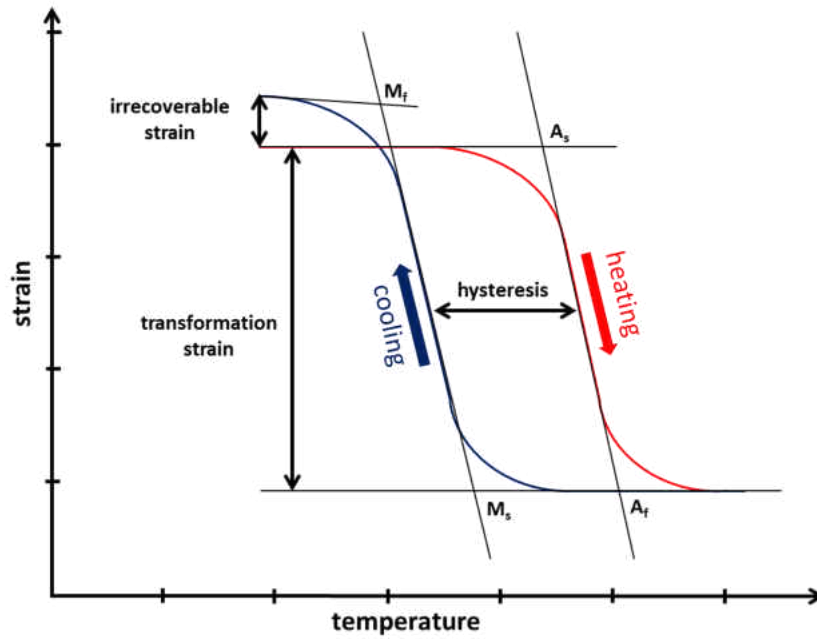
Figure 2.2: Stress-temperature response during isobaric loading (thermal cycling under constant load) of a typical shape memory alloy.
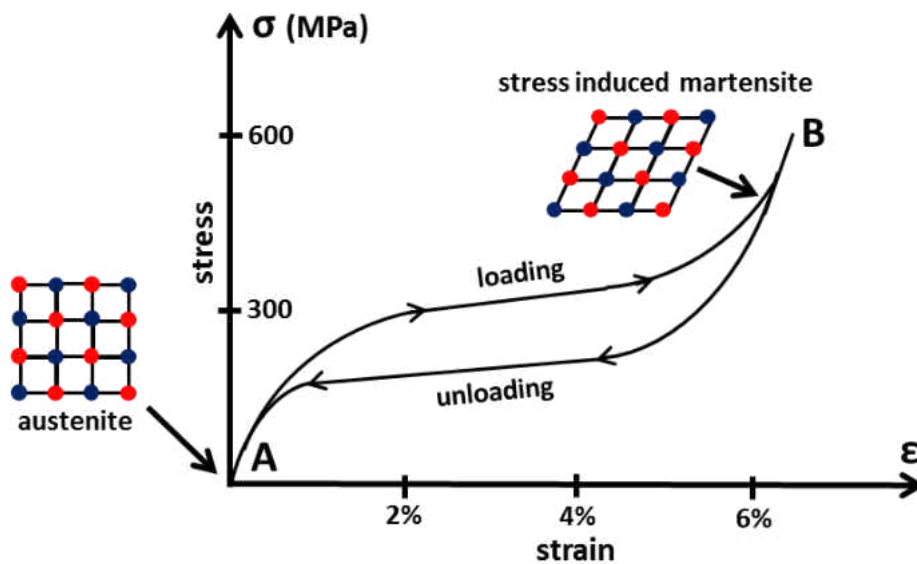
Figure 2.3: Stress-strain response during isothermal loading above the A_f of a typical superelastic shape memory alloy.

15
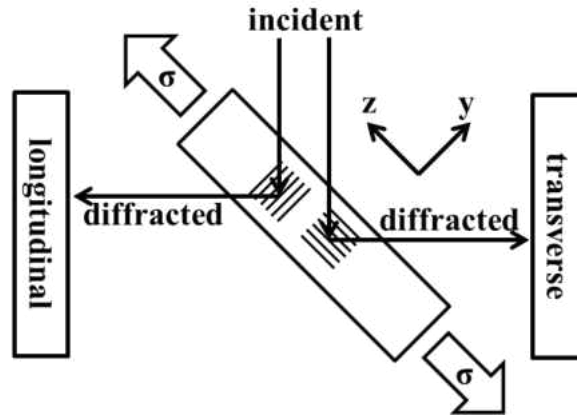
Figure 2.4: The diffraction geometry used at both SMARTS and VULCAN. Two detector banks capture reflections from lattice planes perpendicular and parallel (longitudinal and transverse, respectively) to the specimens loading axis.
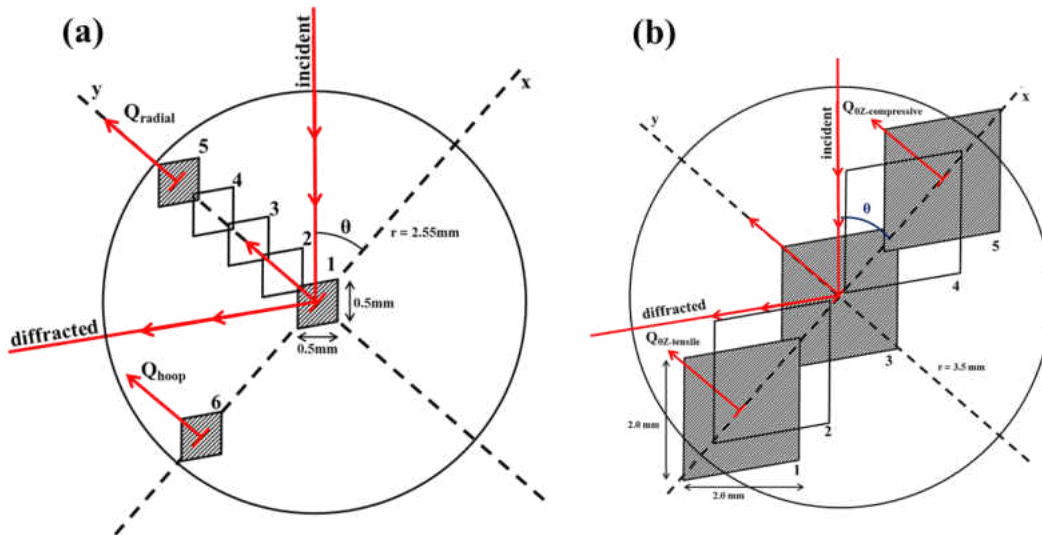
Figure 2.5: Possible diffraction geometries at NRSF2 with portable axial/torsion load frame in a cross-section of the cylindrical specimen: (a) with load frame vertical showing outlines of the six diffraction gauge volumes ($0.5 \times 20 \times 0.5$ mm^3) within the cylinder (diffraction vectors Q_{radial} and Q_{hoop}, correspond to locations 1-5 and 6, respectively) and (b) with load frame tilted to 43° about the x-axis showing outlines of five diffraction gauge volumes ($2 \times 2 \times 2$ mm^3) within the cylinder (diffraction vectors $Q_{\theta z\text{-}tensile}$ and $Q_{\theta z\text{-}compression}$ represent principle stress directions under torsional shear).

16
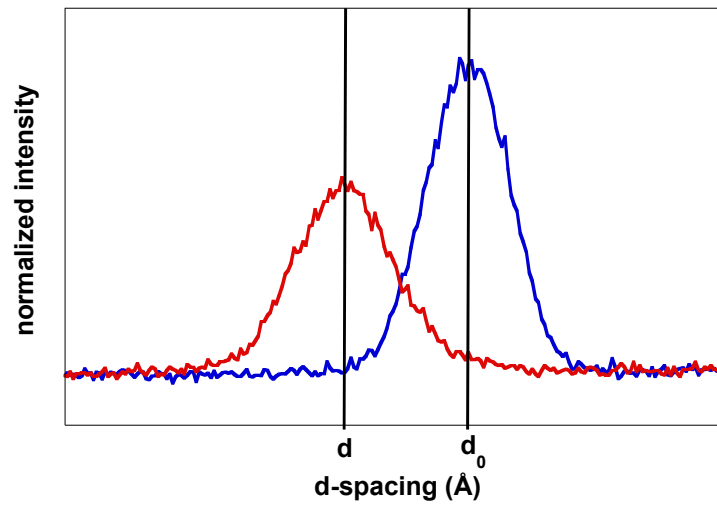
Figure 2.6: Representative peak shift, broadening and intensity change in a neutron diffraction spectrum acquired from reflections from specific crystallographic direction.

CHAPTER THREE: THERMOMECHANICAL BEHAVIOR OF SHAPE MEMORY NITI SPRINGS: EXPERIMENTALLY VALIDATED MODEL

To facilitate the implementation of shape memory alloys (SMAs) in commercial applications, a framework was developed for a multi-axial, multi-mechanism based constitutive model for the comprehensive representation of the evolutionary response of SMAs under general thermomechanical loading conditions. In this chapter, SMA spring actuators were used to experimentally validate the ability of this aforementioned model to predict the evolutionary response under multi-axial conditions. Under complex and evolving stress states the boundary conditions imposed are expected to have significant effects on SMA behavior. Thus there is a need to experimentally assess the effects of various constraints on the thermomechanical behavior of SMA spring actuators. Towards this goal, a modular test setup was assembled with the objective of acquiring stroke, temperature, rotation and moment data in real time during joule heating and forced convective cooling of SMA springs under constant axial load. This work specifically targets the role of rotational constraint during thermomechanical cycling of a NiTi (nominal composition 49.9 at.% Ni) SMA spring actuator. The following two cases of rotational constraint and corresponding experimental configurations were considered: (i) the ends of the spring were allowed to freely rotate and the angle of twist (relative to the initial condition) was measured and (ii) the ends of the spring were constrained from rotation and the reaction moment was measured. During both cases, the axial displacement (position of axially free end measured relative to the initial condition) of the SMA spring was tracked during actuation. Results demonstrating the capability of the model to capture the experimental response are summarized here and additional details regarding the model can be found in Ref. [23].

18

3.1 Introduction

Shape memory alloys (SMAs) have the ability to produce large work output in compact spaces by means of fully reversible solid-state phase transformation [4, 5, 24]. With the ability to recover large strains against external load, SMAs can be used as solid-state actuators. In recent decades SMA actuators have been traded against conventional actuation systems in aerospace applications as means of reducing weight, cost and complexity of the overall system [25-30]. Additionally, with the ability to operate in complex forms, e.g., beams, springs, flexures, couplers, etc. SMA can be used to effect systems in ways not yet realized or possible with conventional actuation systems (e.g. in the case of, variable geometry chevrons for jet engine [29] or as slat cove fillers in high-lift flight configurations [31] to reduce noise during take-off and landing). Despite the aforementioned benefits and many potential applications, the commercial success of SMA in the aerospace industry has been limited in part by a lack of full understanding of their behavior under general, multi-axial loading conditions. To facilitate the implementation of shape SMAs in commercial applications, a framework was developed for a multi-axial, multi-mechanism based constitutive model for the comprehensive representation of the evolutionary response of SMAs under general thermomechanical loading conditions [23, 32, 33]. In this work, SMA spring actuators were used to experimentally validate the ability of this aforementioned model to predict the evolutionary response under multi-axial conditions.

Typically, when operated as actuators SMAs are thermally cycled under constant load (henceforth called isobaric loading). During cyclic isobaric loading irrecoverable strain may accumulate with each cycle. Deformation mechanisms contributing to irrecoverable strain have generally been attributed the accumulation of retained martensite (i.e., martensite existing above

the A_f), dislocation based plasticity and/or deformation twinning [8-10]. Residual strains can be reduced or eliminated by appropriate training processes, thus producing a stable SMA actuation response [5, 7, 10, 34]. SMA training typically involves performing multiple isobaric cycles under the applied load of the intended application. During this process residual strain accumulates with each cycle and increasingly saturates until desired stability is achieved. During training of uniaxial wires or torsional loaded thin-walled tubes, with near homogenous stress states, there is no significant geometry change that results from the accumulation of residual strain. This is not the case for more complex modes of SMA actuation such as a beam in bending or axial loaded spring. During training of SMA axially loaded springs, accumulated residual strain causes an increase in length and pitch and contraction of coil diameter [33, 35]. With a heterogeneous stress state that evolves with cycling, SMA spring actuators provide a "worst case" scenario for SMA model validation. Under complex and evolving stress states the boundary conditions imposed are expected to have significant effects on SMA behavior. Thus there is a need to experimentally assess the effects that boundary conditions have on the thermomechanical behavior of SMA spring actuators. Towards this goal, a modular test setup was assembled with the objective of acquiring stroke, temperature, rotation and moment data in real time during joule heating and forced convective cooling of SMA springs under constant axial load.

This work specifically targets the role of rotational constraint during thermomechanical cycling of a NiTi SMA spring actuator. The following two cases of rotational constraint and corresponding experimental configurations were considered: (i) the ends of the spring were allowed to freely rotate and the angle of twist (relative to the initial condition) was measured and

(ii) the ends of the spring were constrained from rotation and the reaction moment was measured. During both cases, the axial displacement (position of axially free end measured relative to the initial condition) of the SMA spring was tracked during actuation. Results demonstrating the capability of the model to capture the experimental response are summarized here and additional details regarding the model can be found in Ref. [20].

3.2 Experimental Procedures

3.2.1 Spring Fabrication

The material used in this work was a binary NiTi alloy (nominal composition 49.9 at.% Ni), produced by Special Metals (now SAES Smart Materials, New Hartford, NY). This alloy is part of suite of NiTi-based SMAs developed by NASA Glenn Research Center and has been extensively studied elsewhere [7, 36-39]. Wire was Electro Discharge Machined (EDM) (to a wire diameter of 2.16 mm) from the same extrusion used to calibrate the SMA model. The wire was wound onto a mandrel with a helical grove (with the geometric parameters of the modeled spring) at room temperature. A sleeve was slid over the wire and mandrel to ensure that the wire maintained its desired spring shape throughout the shape-setting process. The spring was shape-set at 450°C for 30 min. and then ice-quenched. It has previously been shown that the shape-setting process does not have a significant effect on subsequent thermomechanical behavior in this particular material system [40]. Figure 3.1 shows the geometry of the NiTi shape memory alloy spring actuators used in the experiments presented here. The as-shape-set spring consisted of three active coils (four in total), with a coil diameter of 23.1 mm and a free length of 19 mm. This process was repeated to produce a total of two identical springs, one for each of the two aforementioned Cases.

3.2.2 Experimental Setup

A modular test setup (as shown in Figure 3.2) for the purpose of testing SMA springs (with various end constraints) was designed and assembled. A detailed description of the experimental setup can be found in Ref [3]. The following two configurations were used to experimentally validate Case 1 and Case 2. For Case 1, one spring mount was coupled to the torque cell (with a range of 0-176.5 N·mm), to measure the torque produced during actuation when the spring was constrained from rotating. For Case 2, one spring mount was coupled to a rotary encoder, to measure the degree of twist produced during actuation when the spring was free to rotate. For both cases care was taken to ensure the boundary conditions mirrored (as close as possible) the boundary conditions applied in the simulation (i.e., rigid with no conductive heat loss at the point of contact with each spring mount).

3.2.3 Thermomechancial Testing

Using the setup described in Section 3.2.2, the following tests were performed. Two stress-free thermal cycles (between room temperature and 165 °C) were performed (to relieve any residual stresses produced by processing, machining or installation of the spring) prior to the experiment after the spring was installed in the setup. Following the two no-load thermal cycles an axial tensile load of 8.8 N was applied to the spring at room temperature. Under this constant load, up to 20 thermal cycles were performed between an LCT=35 °C and UCT=165 °C. This thermomecahincal loading procedure was performed for Case 1 and Case 2 using an as shape set spring for each case.

3.3 Results and Discussion

In all experimental cases an 8.8N axial load was applied at room temperature. This load was chosen specifically as it was analytically shown (using methodology presented in Ref. [41]) to produce approximately 100 MPa maximum effective stress in the spring. This analytical result was in good agreement with model which showed a maximum effective stress of 107.7 MPa under the 8.8N applied axial load. The good agreement was expected due the material deformation being mostly elastic with limited variant reorientation and detwinning when isothermally loaded up to 100 MPa. Following the initial isothermal loading to 8.8 N of axial load, the load was held constant and the spring was thermally cycled between 30°C and 165°C.

Figure 3.3a shows the axial displacement at 30°C (martensite) and 165°C (austenite), for both Cases 1 and 2 (with the ends of the spring are rotationally constrained and unconstrained, respectively) during thermal cycling under an 8.8 N applied load. Figure 3.3b shows the axial stroke (i.e., the difference between the displacement at 30°C and 165°C) for both Cases 1 and 2 (with the ends of the spring are rotationally constrained and unconstrained, respectively). Initially both cases produced the same amount of displacement and stroke; however after the stroke stabilized (after approximately 5 cycles) the rotationally unconstrained spring produced 2-3 mm more stoke than the rotationally constrained spring. The difference in stroke appears to increase with additional cycling and continued evolution (up to ~5 mm after 20 cycles). The angle of twist produced at the ends of the rotationally unconstrained (Case 2) spring increased with evolution and cycle, as shown Figures 3.3c. The moment produced at the ends of the rotationally constrained spring (Case 1) increased with each cycle, as shown in Figure 3.3d.

23

Overall, Figure 3 shows a summary of the experimental results for thermal cycling of a NiTi spring actuator under 8.8 N for both Cases (1) and (2). Results for both cases show that the displacement increased (without bound, however the rate of increase of displacement decreased) during each thermomechanical cycle (for up to the 20 thermomechanical cycles tested). The stroke for each case was the same (within error) and increased, for the first 3 to 5 cycles. For Case (1) the stroke stabilized after approximately 5 cycles. For Case (2) the stroke began decreasing after approximately 5 cycles. Hence, over the entire 20 cycles the rotationally unconstrained case produced a larger stroke. For both cases, the angle of twist and reaction moment (so called secondary responses), respectively, also increased with each thermomechanical cycle. Increases in the secondary responses were larger (near an order of magnitude) in austenite than in martensite. This result can be attributed to favorable selection of martensite variants which minimizes the secondary responses observed in martensite during cycling.

Figure 3.4 shows geometry evolution of a NiTi spring actuator at the LCT and UCT during the initial three thermal cycles (between 30°C and 165°C) under a constant load of 8.8N (with the ends constrained from rotating). Both pictures of the experimental spring actuator and corresponding model are shown for comparison (reproduced from Ref. [23]). During the initial thermal cycle under load [from point (2) to (4)], a large amount of deformation was observed due to the transient response. The transient response in NiTi is typically attributed to reorientation and detwinning of martensite variants during cooling on the first thermal cycle under isobaric load. This response has previously investigated in Ref. [42] and observed e.g., in Ref. [32, 43, 44], among others. Here for the case of axial loaded springs the transient response produces a

large change of the spring's geometry. As observed from points (2) to (4) in Figure 3.4, the spring length and pitch significantly increase and the coil diameter decreases. The behavior was observed experimentally and captured well by the model (which was calibrated using only uniaxial results). With continued cycling (from points 2 to 8) the formation of residual strain was observed as cycle-to-cycle increase of the springs length, which was also captured well by the model.

The ability of the models ability to capture the experimental response can be summarized in Figure 3.5. Figure 3.5 shows the displacement at the LCT and UCT and stroke during the initial 10 thermal cycles (between 30°C and 165°C) under a constant load of 8.8N (with the ends constrained from rotating) of a NiTi spring actuator, comparing a) experiment and b) model [23]. Overall, the model captured the axial displacement response of NiTi spring actuator well (with up to 15% error).

3.4 Conclusions

To facilitate the implementation of shape SMAs in commercial applications, a framework was developed for a multi-axial, multi-mechanism based constitutive model for the comprehensive representation of the evolutionary response of SMAs under general thermomechanical loading conditions. In this work, SMA spring actuators were used to experimentally validate the ability of this aforementioned model to predict the evolutionary response under multi-axial conditions. The following two cases of rotational constraint and corresponding experimental configurations were considered – (i) the ends of the spring were allowed to freely rotate and the angle of twist was measured and (ii) the ends of the spring were

constrained from rotation and the reaction moment was measured – and the following conclusions were made.

1.) The rotationally unconstrained spring produce (up to 5%) more stroke than the rotationally constrained (for the number of cycles performed here).

2.) For both cases, the angle of twist and reaction moment (so called secondary responses), respectively, also increased with each thermomechanical cycle. Increases in the secondary responses were larger (near an order of magnitude) in the austenite than in the martensite. This result can be attributed to favorable selection of martensite variants which minimized the secondary responses observed in martensite during cycling.

3.) The model captured well, geometric changes (e.g., axial displacement and stroke; increases in pitch; and contraction of coil diameter) corresponding to the transient and evolutionary behavior observed during thermomechanical cycling of NiTi.

This successful experimental validation of the simulated response of SMA spring actuators proved the feasibility of modeling and designing SMA actuators, in complex forms, to operate over an extended number cycles. Additionally, the effects of boundary conditions SMA spring actuators were experimentally captured and should be considered during the modeling and design process.
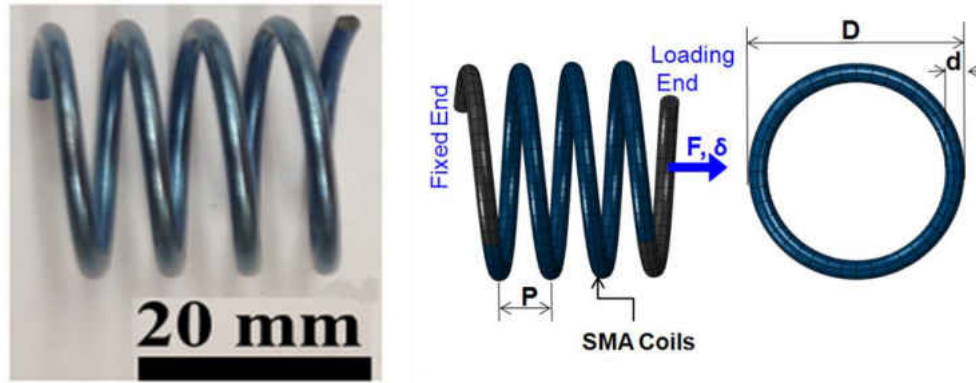
Figure 3.1: Geometry of the NiTi shape memory alloy spring actuators used in the experiments presented here.
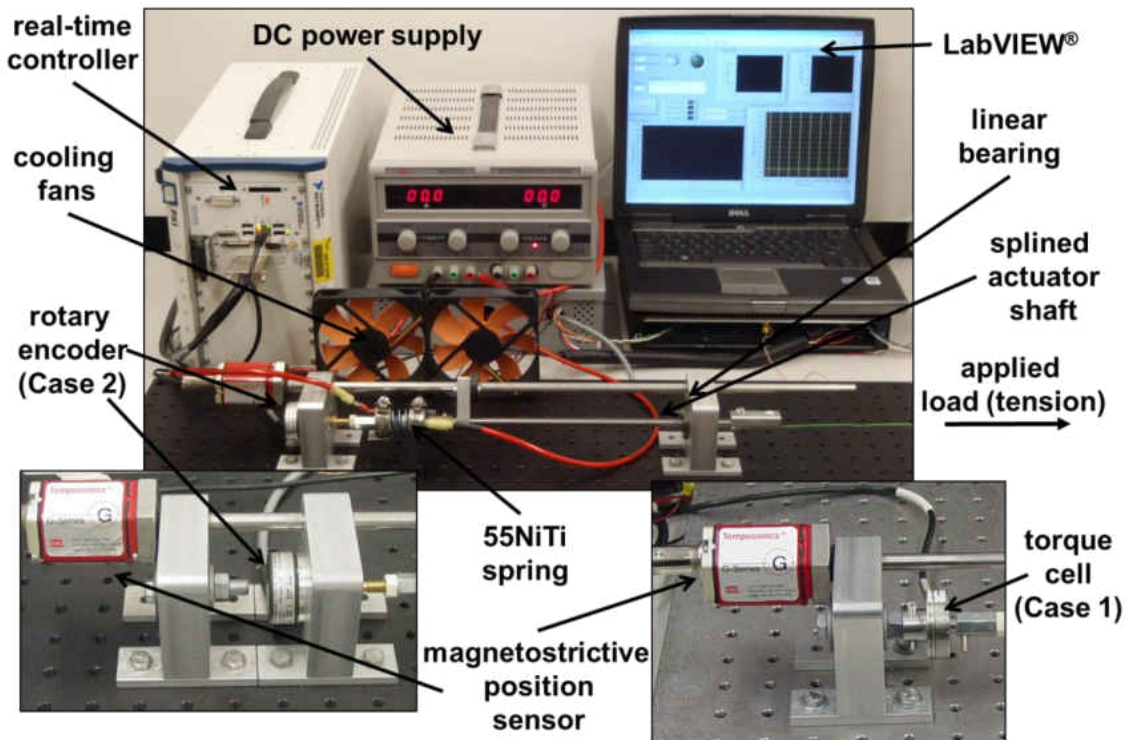
Figure 3.2: Modular experimental setup for thermomechanical testing of shape memory alloy spring actuators. Configurations are shown for two cases: Case (1) with the ends of the spring free to rotate and Case (2) with the ends of the springs constrained from rotating.
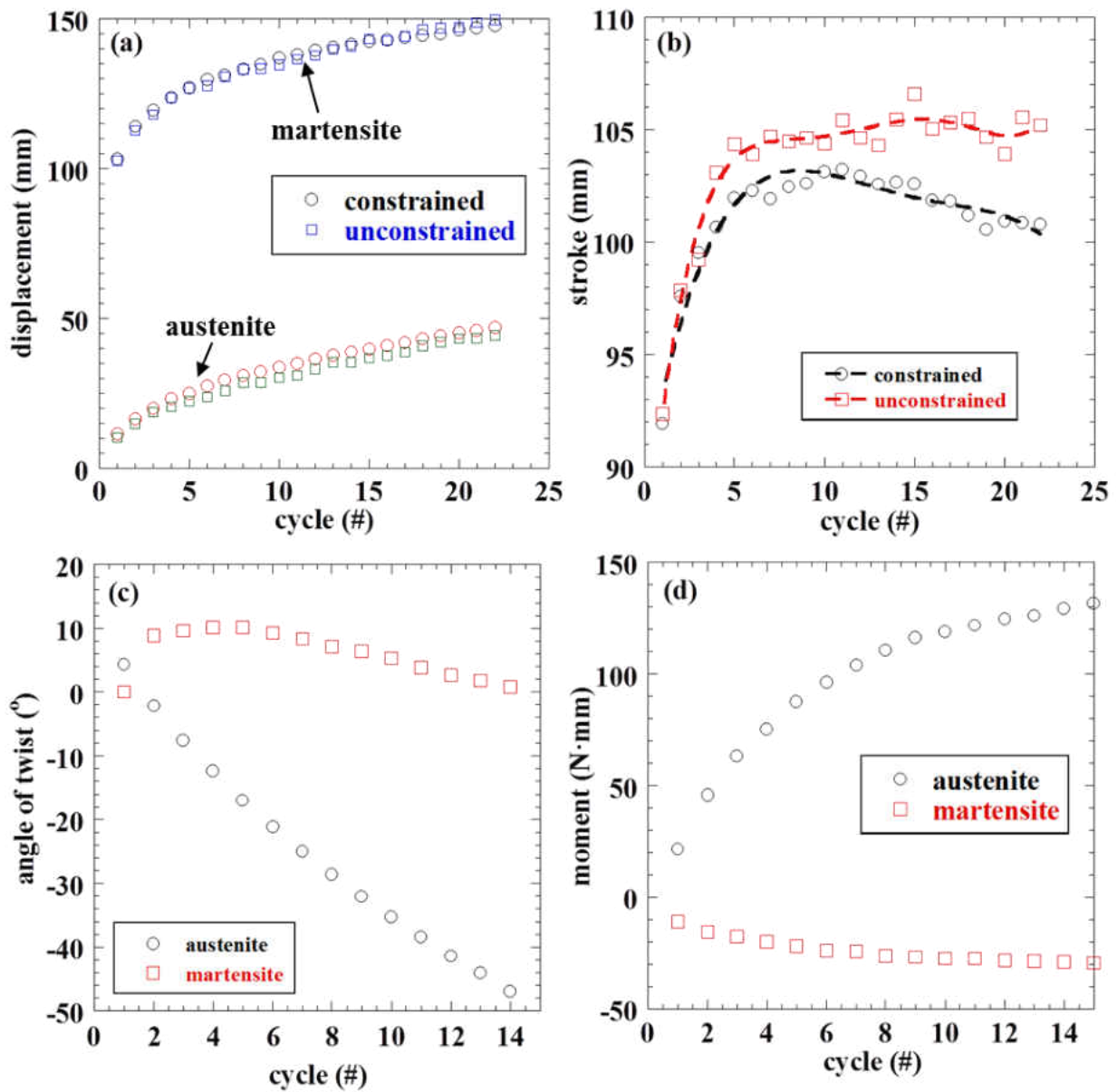
Figure 3.3: Thermal cycling of a near-equiatomic spring actuator under an 8.8 N applied load. The axial displacement response is shown for both cases (with the ends of the spring are rotationally constrained and unconstrained): (a) displacement vs. cycle for austenite and martensite; and (b) actuation displacement (stroke) vs. cycle. The secondary responses are also shown: (c) angle of twist vs. cycle for the rotationally unconstrained; and (d) moment vs. cycle for the rotationally constrained.
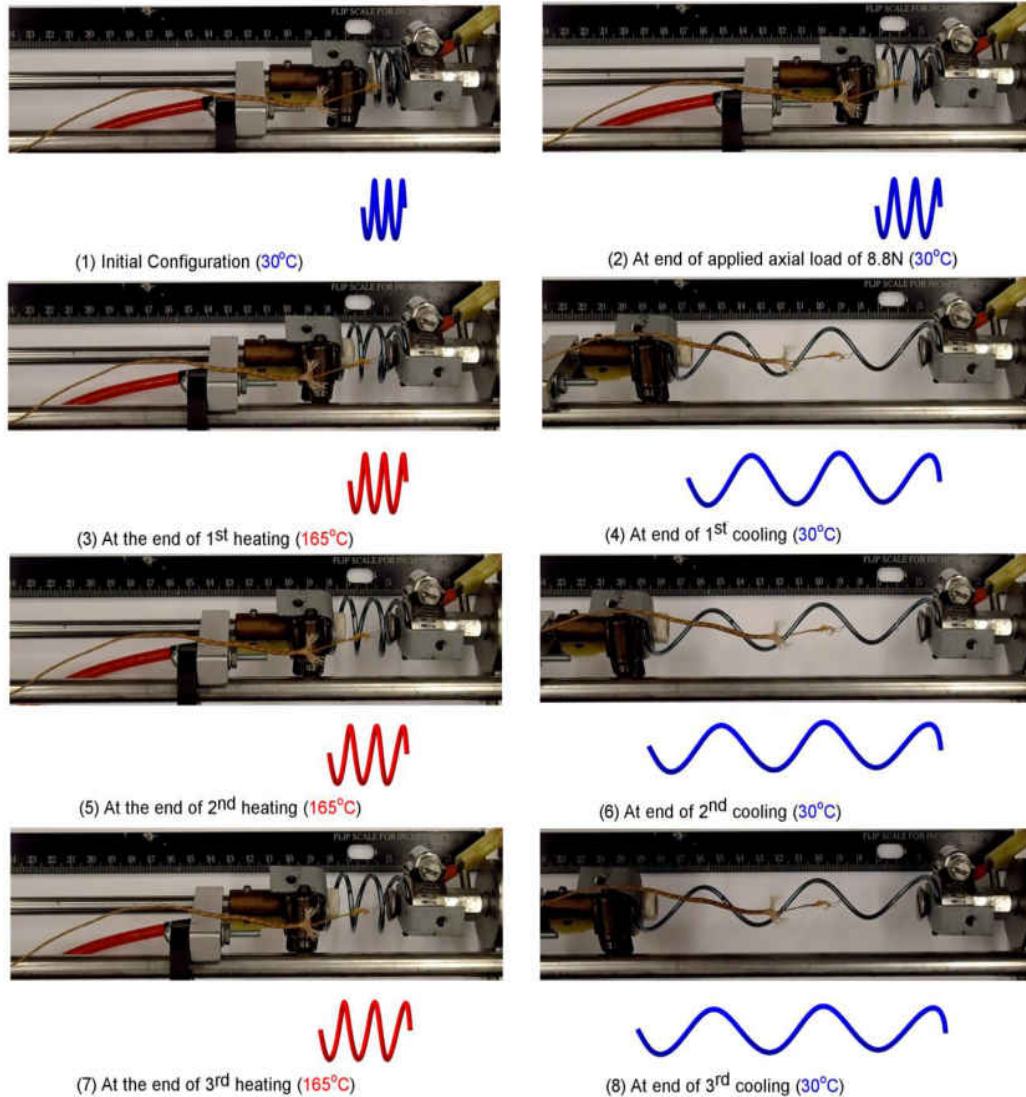
Figure 3.4: Geometry evolution of an NiTi spring actuator at the LCT and UCT during the initial three thermal cycles (between 30°C and 165°C) under a constant load of 8.8N (with the ends constrained from rotating). Both pictures of the experimental spring actuator and corresponding model are shown for comparison [23].
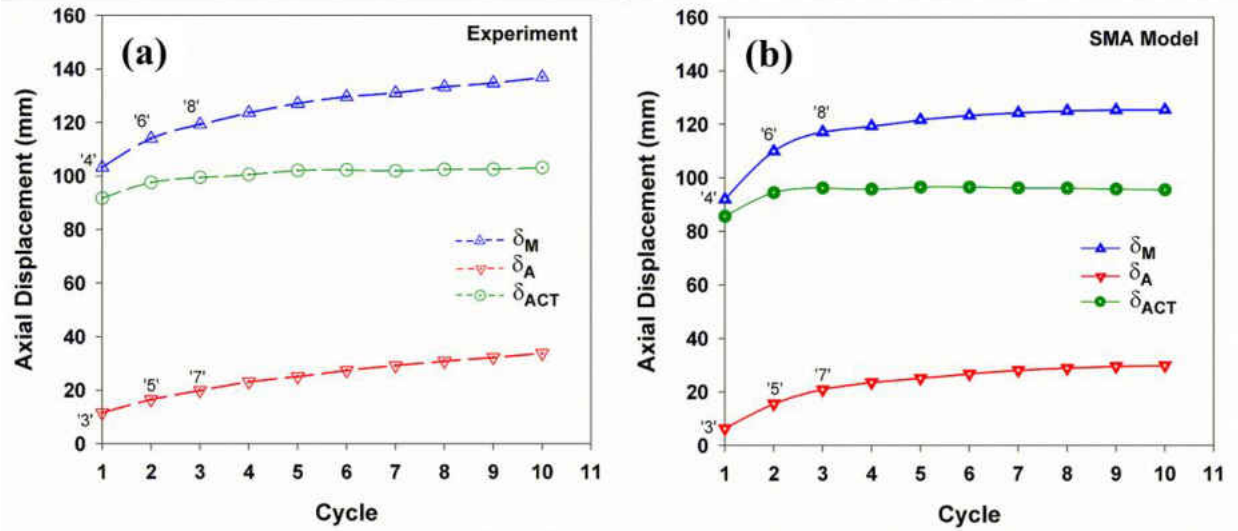
Figure 3.5: Displacement at the LCT and UCT and stroke during the initial 10 thermal cycles (between 30°C and 165°C) under a constant load of 8.8N (with the ends constrained from rotating) of an NiTi spring actuator, comparing a) experiment and b) model [23].

CHAPTER FOUR: HEATING AND LOADING PATHS TO OPTIMIZE THE PERFORMANCE OF TRAINED SHAPE MEMORY ALLOY TORSIONAL ACTUATORS

This chapter (originally produced in Ref. [30]) serves to establish connections between torsional SMA actuators designed for application and neutron diffraction results to be presented in later chapters. In this work, near-equiatomic NiTi shape memory alloy (SMA) torsional tube actuators were trained for two-way shape memory effect (TWSME) by repeated thermal cycling under an isobaric load. Performance of the trained actuators was assessed by thermally cycling through a complete phase transformation under a range of isobaric loads that varied from negative to positive and included loads near zero. To assess the actuation performance of the trained SMA components, extended isobaric thermal cycling and cycling under varying loads to constant strain limits was performed. Additionally, isothermal loading was applied in the fully martensitic state prior to and following training.

Results are discussed in the context of the correlation between uniaxial isobaric and isothermal loading and texture measurements obtained by in situ neutron diffraction at stress and temperature. These results show various thermomechanical combinations of heating and loading sequences that yield the same final martensite texture in SMA, which highlights the ability to take different paths yet still obtain the desired actuator response while minimizing irrecoverable deformation mechanisms. The implications of extending these uniaxial results to the design and fabrication and ultimately improving the performance of torsional SMA actuators are discussed.

4.1 Introduction

Shape memory alloys (SMA) have the ability to recover their shape against external load which enables their use as high work output, light-weight, compact actuators for aerospace, automotive and other industrial applications [25, 45, 46]. The ability to recover shape against load occurs by way of a thermally (shape memory) or stress (superelastic) induced solid-state phase transformation [4, 5]. Commercial viability of SMA actuators has been limited due to dimensional instabilities associated with repeated thermal cycling through the phase transformation under load. Furthermore, SMA actuators are typically designed to operate in one direction against an external bias force or a second antagonistic SMA element that adds complexity, reduces performance and increases the overall size and weight of the actuation system.

Training of SMA by repeated isobaric (thermal cycling under constant load) or isothermal (stressing at constant temperature) [7] loading has been shown to produce stable two-way shape memory effect (TWSME), which eliminates the need for external bias forces or antagonistic SMA elements that can be both heavy and require added complexity. Training has also been shown to increase dimensional stability in the isobaric and isothermal response under repeated thermal cycling and loading, respectively.

Isothermal [7, 36, 47] and isobaric [16, 43] loading of SMA has been extensively studied, however investigations of the interaction between the two loading paths are limited. Furthermore, there has been a limited amount of work which investigates isostrain (thermally cycling under constant strain) [40, 48] loading and thermally cycling against spring and varying loads. Often in applications, an SMA actuator will experience many or all of the aforementioned

load paths within its operating space, e.g., an SMA actuated wing flap under varying aerodynamic loads. Therefore, there is a need to map and understand the interactions between these various heating and loading paths. With this in mind, the overall objective of this work is two-fold. The first objective involves mapping heating and loading paths in untrained and trained SMA torsional actuators to ultimately optimize and improve their performance in applications. The second objective is to provide insight into the fundamental understanding of the mechanisms governing the interactions between relevant heating and loading paths.

4.2 Experimental Techniques

Near-equiatomic NiTi (nominal composition 49.7 at. % Ni) was cold drawn (~40 % reduction in area) into tubing with an outside and inside diameter of $D = 7.11$ mm and $d = 4.27$ mm, respectively. The as-drawn tube was low temperature annealed and straightened. The tubing was then cut to a length of 241.3 mm and 19.05 mm long splines were machined onto each end which resulted in a gauge length of $L=203.2$ mm.

All thermomechanical loading was performed in a test fixture instrumented to measure torque and angle. The tubes were heated by internal cartridge heaters which spanned the total length of the tube. Three K-type thermocouples were used to acquire temperature with one thermocouple in the center of the gauge and the other two thermocouples within 25.4 mm of the respective ends of the gauge section. All reported temperatures are the mean of these three thermocouples. The tubes were fixed at one end and free to rotate at the other and torque was applied by mechanical pulley system with attached dead weight or springs. All rotations (θ) and torques (T) will be reported as shear strain and shear stress, respectively, calculated at the surface as follows: shear strain $\gamma = D\theta/(2L)$ and shear stress $\tau = 16TD/[\pi(D^4-d^4)]$.

All thermal cycling was performed between a lower cycle temperature (LCT) and upper cycle temperature (UCT) of 35 and 145°C unless otherwise stated. After installing the tubes into the test fixture two no-load thermal cycles were performed to relieve any residual stresses produced by machining or installation. The torque and angle were then zeroed. The tube was isothermal loaded to ±7% (positive followed by negative) shear strain, then back to +7% shear strain and finally unloaded to zero shear stress. Two isobaric thermal cycles were performed at each of the following shear stress values 0, 206, 109, 79, 34 and 0 MPa, in order as listed.

Following this characterization, training by repeated isobaric thermal cycling was performed. Following training, two no-load thermal cycles were performed and the angle was zeroed to the angle at the UCT on the 2nd cycle. Two isobaric thermal cycles were performed at each of the following shear stress values 206, 109, 79, 34, 0 and -24MPa, in order as listed. Note, positive values indicate the direction in which torque was applied during training and negative values indicate the opposing direction. The isothermal loading path performed prior to cycling was repeated, i.e., the tube was isothermal loaded to ±7% (positive followed by negative) shear strain, then back to +7% shear strain and finally unloaded to zero shear stress.

A 2nd as-trained tube was thermally cycled 10 times under zero shear stress with a constant shear strain limit at 3.2% shear strain. During thermal cycling the tube was free to rotate at shear strains <3.2%, thus the constant strain limit restricted actuation when reached on cooling. A 3rd as-trained tube was thermally cycled 500 times to a LCT = 40±2°C and UCT = 92±4°C against a varying torsional spring load. Note, temperature limits were varied as necessary to maintain shear strain values at the LCT and UCT. The shape and magnitudes of the applied spring load will become apparent in the results section. On the 500th cycle the sample

was cooled to room temperature under zero load. The tube was isothermally loaded at room temperature to the same torsional spring load line. The tube was then heated to 56.7°C then cooled back to room temperature. The following uniaxial experiments were performed *in situ* at SMARTS at LANL and the VULCAN engineering diffractometer at ORNL. More details regarding the experimental setups at VULCAN and SMARTS can be found in Ref. [2, 17] and [49], respectively, and in Section 2.2.1 in Chapter 2.

Two samples were machined from a near-equiatomic binary NiTi (nominal composition 49.9 at. % Ni) to cylindrical dog-bone samples with threaded ends and a gauge diameter of 5.08 mm. This material and sample geometry has been extensively utilized in previous work and more details can be found in Ref. [7-10, 16, 36, 40]. During each of the following experiments strain was monitored by extensometry. Two no-load thermal cycles between room temperature and 200°C were performed prior to each of the following experiments to relieve any residual stresses produced by machining or installation. The first specimen was isothermally loaded to 4% tensile strain (at a strain rate of 10^{-4}) at room temperature at SMARTS. The second specimen was isobarically loaded under 100 MPa between an LCT = 35°C and UCT = 165°C at VULCAN. To acquire adequate statistics a hold time of 30 min and 15 min was used at SMARTS and VULCAN, respectively. Inverse pole figures (IPFs) were generated from Rietveld refinements of the neutron diffraction spectra. IPFs represent the distribution of a selected direction in the specimen relative to the crystal axes in multiples of random distribution (where 1 corresponds to random distribution). More details about analyzing texture by recourse to Rietveld refinement can be found in Ref. [50].

4.3 Effect of Training

4.3.1 Isobaric Performance

Performance of the tubes was assessed by thermally cycling through complete phase transformation under a range of isobaric loads that varied from negative to positive and included loads near zero. Figure 4.1a shows the shear strain at the UCT (as indicated by ◊) and LCT (as indicated by □) on the 2nd of two isobaric cycles at shear stresses of 206, 109, 79, 34 and 0 MPa, before training. Also shown is the shear strain at the UCT (as indicated by ♦) and LCT (as indicated by ■) on the 2nd of two isobaric cycles at shear stresses of 206, 109, 79, 34, 0 and -24MPa, after training. Note, all values shown in Figure 4.1a were normalized such that the shear strain at zero shear stress was zero at the UCT, respectively, before and after training. The transformation temperatures of the trained tube were acquired by tangent-intersect method of the strain-temperature response. The austenite start, austenite finish, martensite start and martensite finish were found to be $A_s = 64.1$, $A_f = 85.5$, $M_s = 59.3$ and $M_f = 39.8$, respectively under no applied torque.

The points acquired at the UCT were linearly fit before and after training providing "apparent" shear moduli (henceforth referred to as austenite actuation moduli) of 15.04 and 11.92 GPa, respectively. The martensite response (henceforth, referred to as martensite actuation response) was non-linear and was fit with an exponential function (as indicated by "dotted" and "dashed" blue lines) for the purpose of depicting the regions bound by the responses, respectively, before and after training. Note, these shear moduli are considered "apparent" as they do not represent a conventional linear elastic response and other mechanisms may be

contributing to the response. The actuation moduli are used here only as a qualitative comparison of the macroscopic actuation behavior, before and after training.

Figure 4.2b shows the actuation strain (i.e., the absolute difference between the LCT and UCT points defined in 1a) before and after training. Two-way shape memory effect (TWSME) is defined as the actuation strain at no-load or zero shear stress (as shown in Figure 4.2). TWSME was negligible before training and was found to be 4.91% after training. TWSME is typically defined at no-load, however the internal stress fields creating the TWSME influence the actuation behavior over the complete range shear stresses examined here. This was observed as an increase and decrease in actuation strain at shear stresses below and above ~100 MPa, respectively. The majority of the change in actuation strain arises from change in the martensite actuation response due the redistribution of martensite variants by martensite variant reorientation and detwinning, formation of dislocation based plasticity and/or deformation twinning.

Overall, the martensite actuation response becomes stiffer after training at shear stresses greater than 0 MPa. At shear stresses near or less than 0 MPa, the martensite actuation response decreases significantly due to the preferential reorientation of martensite variants. The small decrease in the austenite actuation modulus after training was possibly due to the formation of retained martensite in the trained actuator. All such aforementioned deformation mechanisms are coupled and have previously been shown [7-10, 16, 36, 40]; to become active during thermomechanical cycling of near-equiatomic NiTi SMAs; and create internal stress field which generate TWSME and stabilize the cyclic isobaric response.

Typically, the area between the austenitic and martensitic responses (as shown figure 4.1a) provides a simple model of the space in which an SMA actuator can reliably operate under isobaric and spring loads. To facilitate the following discussion this space will be referred to as the operating space. The operating space before and after training consist of Regions I+II+III and Regions III+IV, respectively. Reliability under spring loads relative to the operating space defined here will be demonstrated in the subsequent Section "Application Relevant Loading Paths".

4.3.2 Isothermal Response

Figure 4.2 shows isothermal forward and reverse loading (forward followed by reverse) to ±7% shear strain at room temperature prior to (as indicated by the black line) and following training (as indicated by the red "dashed" line). Note, forward and positive indicate the direction in which load was applied during training. Before training, primarily elastic loading of self-accommodated martensite was observed on initial forward loading from 0 to ~1% shear strain. From ~1% to ~5% shear strain, variant reorientation and detwinning of self-accommodated martensite occurs which resulted in a deflated modulus plateau. From ~5% to 7% shear strain, elastic loading of reoriented/detwinned martensite occurs which resulted in a re-hardening behavior. Note, the deformation mechanisms (i.e. elastic deformation of self-accommodated and reoriented martensite and variant reorientation and detwinning) governing the isothermal response of martensitic NiTi are coupled throughout all regions, and can include contribution from irreversible plastic deformation [8] of loading and modulus refers to an "apparent" modulus. This behavior and the mechanisms governing it have been extensively studied and more details can be found in Refs. [7, 8, 36].

Upon reverse loading from 7% back to ~4% shear strain, primarily elastic unloading/loading of reoriented martensite with some variant reorientation and detwinning was observed. From ~4% to ~-5% shear strain, variant reorientation and detwinning occurs which resulted in a deflated modulus plateau. Note, the onset of variant reorientation and detwinning occurs at an increased shear stress (approximately -150 MPa) on reverse loading as preferentially oriented martensite is now reorienting back to self-accommodated. After passing through zero shear strain, continuing to ~-5% shear strain, martensite variants preferentially reoriented to the reverse loading. Then, from ~-5% to -7% shear strain, the onset of elastic loading of reoriented/detwinned martensite occurs which resulted in a re-hardening behavior. The aforementioned reverse loading process from 7% to -7% shear strain was then repeated in the forward direction from 7% to -7% shear strain.

The shear stress-strain response was symmetric between the reverse response and 2nd forward response, i.e., at -7% and 7% the shear stress was -284.8 and 283.6 MPa, respectively. This is not the case for uniaxial tension-compression reverse loading of NiTi in which tension-compression asymmetry was observed, see Ref. [51]. Positive and negative rotational symmetry is expected under torsional loading, however this symmetry was not expected when reverse loading was followed by forward loading. This result indicates that martensite variant reorientation processes are near fully reversible by isothermal loading within the limits investigated here.

After training, two no-load thermal cycles were performed and the shear strain was zeroed to the angle at the UCT on the 2nd cycle. Upon cooling to room temperature TWSME produced 4.95% shear strain, as shown in Figure 4.2. From this point forward and reverse

loading (forward followed by reverse) to ±7% shear strain at room temperature was repeated (indicated by the red "dashed" line). Initial loading from 4.95% to 7% shear strain shows primarily elastic loading of reoriented martensite. At 7% shear strain the magnitude of shear stress was 166.2 MPa which was approximately the same (i.e., 169.6 MPa) at the same point, prior to training. This indicates that martensite variants were preferentially selected in the trained actuator as biased by internal stress fields. Also, this preferential variant selection was equivalent to the variant selection formed under isothermal loading at 4.95% shear strain prior to training.

Upon reverse loading from 7% to -7% then back to 7% shear strain the response was similar to the response prior to training. Although the response was similar, the shear stress-strain response was slightly asymmetric between the reverse response and 2nd forward response, i.e., at -7% and 7% the shear stress was -248.6 and 299.2 MPa, respectively. This indicates that martensite variant reorientation was redistributed by the internal stress fields and associated mechanisms which were created during training. However, these internal stress fields and associated mechanisms did not have a significant effect on elastic loading/unloading and did not limit the overall available martensite variant reorientation and detwinning in the trained actuator.

4.4 Correlations between Isothermal and Isobaric Loading Paths and Texture

The martensite variant reorientation and detwinning process observed can be correlated to changes in textures observed through IPFs. Figure 4.3a shows the IPF after two no-load thermal cycles at zero stress-strain prior to any loading that is representative of a self-accommodated martensitic structure. Also shown is the IPF acquired at 4% strain and 305 MPa stress following isothermal loading indicative of preferential selection of martensite variants by variant reorientation and detwinning processes.

40

Figure 4.3b shows uniaxial isobaric loading under 100 MPa tensile stress between a LCT = 35°C and UCT = 165°C. The sample was loaded to 100 MPa tensile stress with a conjugate 0.2% strain at room temperature. Also, shown is the IPF at 100 MPa and 0.2% strain at room temperature indicative of elastically loaded self-accommodated martensite variants. The sample was then heated to 165°C while maintaining a constant tensile stress of 100 MPa. Upon cooling from 165°C to 35°C the strain increases to 3.9%. After cooling, the IPF at 100 MPa tensile stress and 0.2% strain at room temperature is shown, again, indicative of preferential selection of martensite variants by variant reorientation and detwinning processes.

The preferential variant selection observed following isothermal loading and isobaric loading to ~4% tension appears nearly equivalent. The martensite variant structure formed at 4% strain required isothermal loading to 305 MPa whereas a near equivalent martensite variant structure formed was formed at 3.9% strain by isobaric loading at 100 MPa. Thus, it appears an equivalent martensite variant structure for a given strain can be obtained at a lower stress under isobaric loading as opposed to a higher stress under isothermal loading.

This result manifests in the relationship between the martensite actuation response and isothermal response of the untrained and trained torsional actuators and was demonstrated in Figure 4.2 as follows. Figure 4.2 shows the martensite actuation response, after training from Figure 4.1a (as indicated by ■), transcribed over the isothermal response. The martensite actuation response obtained by isobaric loading was more compliant than the isothermal response under the same range of shear stresses >0 MPa and shear strains >5%. Furthermore, the martensite actuation strain response significantly decreases at shear stresses near and less than 0 MPa (up to -30 MPa) due to martensite variants preferentially reorienting to the reversed

principle stress directions during reverse torsional isobaric loading. However, upon reverse isothermal loading from 7% to 0% shear strain, the onset of variant reorientation and detwinning did not occur until ~-150 MPa shear stress was reached.

The notion of equivalent martensite variant structure to equivalent strain – independent of strain obtained by isobaric or isothermal loading – was observed in the torsional actuators. This was demonstrated as follows in Figure 4.2. In the untrained tube the initial 7% shear strain was obtained by isothermal loading at room temperature. In the trained tube the initial 7% shear strain was obtained by TWSME to 4.95% shear strain, then isothermal loading from 4.95% to 7% shear strain. Both cases resulted in the same shear stress at 7% shear strain (within error). Then the isothermal response (which included significant variant reorientation and detwinning) was the same (within error) during unloading from 7% to 0% shear strain. Thus, the shear strain obtained by TWSME under no-load isobaric loading placed the state of the tube in the same position w.r.t. martensite variant orientation for the given shear strain obtained by isothermal loading in the untrained actuator.

4.5 Application Relevant Loading Paths

Often in applications, an SMA actuator will experience many or all of the aforementioned load paths within its operating space and lifecycle. Examples include SMA actuated wing flaps under varying aerodynamic loads and utilizing strain limits to increase stability of the operating space and extend the life of the SMA actuator. This section demonstrates application relevant loading paths such as; thermal cycling against strain limits; thermal cycling against positive and negative spring loads; and isothermal loading beyond the operating space. These load paths were

42

performed on a torsional SMA actuator representative of the trained actuator and corresponding operating space, as described in Figure 4.1.

4.5.1 Spring Loaded Thermal Cycling

Figure 4.4a shows the 175th to 500th thermal cycle to a LCT = 40±2°C and UCT = 92±4°C performed on a torsional actuator against a varying torsional spring load. Note, temperature limits were varied as necessary to maintain shear strain values at the LCT and UCT. More specifically, the temperatures limits needed to be increased with cycling to obtain the same strain values. This behavior decreased with cycling and was bound by the reported tolerances. The spring load had a maximum shear stress of 47.1 MPa and minimum shear stress of -32.6 MPa at 1.0% and 3.0% shear strain, respectively, and passed through zero shear stress at ~1.8% strain. The spring load was non-linear and stiffer regions of positive shear stress. The minimum shear stress and shear strain were obtained at a temperature near the M_f which indicates that this was approximately the maximum shear strain that could be obtained during cooling. This limit obtained upon cooling under a spring load was consistent with the limit defined by the martensite actuation response of the trained actuator described in Figure 4.1a (and transcribed in Figure 4.4a).

4.5.2 Isothermal Loading Beyond the Operating Space

The tube was cooled under no-load following the 500th cycle under a spring load. This resulted in a TWSME of 4.85% shear strain (as indicated by ● in Figure 4.4b). Figure 4.4b shows negative isothermal loading at room temperature from the resulting TWSME to the extended spring load (indicated by ---) under which the 500 thermal cycles were performed. In

order to assess the thermal stability at this point the tube was heated from room temperature to 56.7°C (just below the A_s) then cooled back to room temperature, as shown in Figure 4b. Some actuation strain was obtained and recovered during this process due to anisotropic thermal expansion of preferentially oriented martensite variants. The tube was then unloaded at room temperature resulting in 4.73% shear strain. This demonstrates that isothermal load paths can be utilized to exceed the operating space (shown in Figure 4.1) defined by isobaric loading. This was possible because the onset of martensite variant reorientation occurs at higher stresses under isothermal loading than under isobaric loading (within the limits investigated here).

4.5.3 Strain Limited Thermal Cycling

The decay in TWSME described in the previous section can be managed by limiting the shear strain obtained on cooling. This helps maintain constant strain limits throughout the life of the actuation system and helps protect against overloading in the forward direction. Figure 4.5a shows the shear strain-temperature response for 1st and 10th no-load thermal cycle (between 35 and 135°C) against a constant shear strain limit at 3.2%. During thermal cycling the tube was free to rotate at shear strains <3.2%, thus the constant strain limit restricted actuation when reached on cooling in the martensitic state. Figure 4.5b shows the maximum blocking stress observed against the 3.2% strain limit on each of the 10 cycles. From Figure 4.5 it becomes apparent that the blocking stress did not significantly affect the isobaric behavior; however the blocking stress decayed with cycling.

4.6 Conclusions and Future Work

The performance of untrained and trained NiTi torsional tube actuators was assessed by thermally cycling through complete phase transformation under a range of isobaric loads that varied from negative to positive and included loads near zero. To assess the actuation performance of the trained SMA components, extended isobaric thermal cycling and cycling under varying loads to constant strain limits was performed. Additionally, isothermal loading was applied in the fully martensitic state prior to and following training. Results were discussed in the context of the correlation between uniaxial isobaric and isothermal loading and texture measurements obtained by *in situ* neutron diffraction at stress and temperature and the following conclusion were made.

1) Isobaric performance of the trained actuators was increased at low positive and low negative shear stress by TWSME formed during training.

2) Martensite variant reorientation and detwinning processes are near fully reversible by isothermal loading within the limits investigated here. Training redistributed the available martensite variant reorientation and detwinning but did not reduce or limit it.

3) A martensite variant structure for a given strain can be obtained at a lower stress under isobaric loading as opposed to a higher stress under isothermal loading. This notion was used to demonstrate that isothermal load paths can be utilized to exceed the operating space defined by isobaric loading.

4) Shear strain obtained by TWSME placed the state of the tube in the same position w.r.t. martensite variant orientation for the given shear strain obtained by isothermal loading in the untrained actuator.

5) Degradation of TWSME occurs during extended thermal cycling under low positive and low negative shear stresses. This degradation can be managed by applying constant strain limits and reduced or recovered by thermally cycling under significantly positive loads.

The aforementioned conclusions should be considered when developing, designing and modeling with SMA torque tube actuators. Several application relevant loading paths were demonstrated here with regard to the above conclusions e.g.; thermal cycling against strain limits; thermal cycling against positive and negative spring loads; and isothermal loading beyond the operating space.

Future work should consider performing *in situ* diffraction studies directly on untrained and trained torsional tube actuators w.r.t. the principle directions of stress. Isothermal training has previously been shown to reduce the amount of time required to train uniaxial SMA actuators. The feasibility of applying the aforementioned relationships between isothermal and isobaric loading to the training process of SMA torsional tube actuators should be assessed.
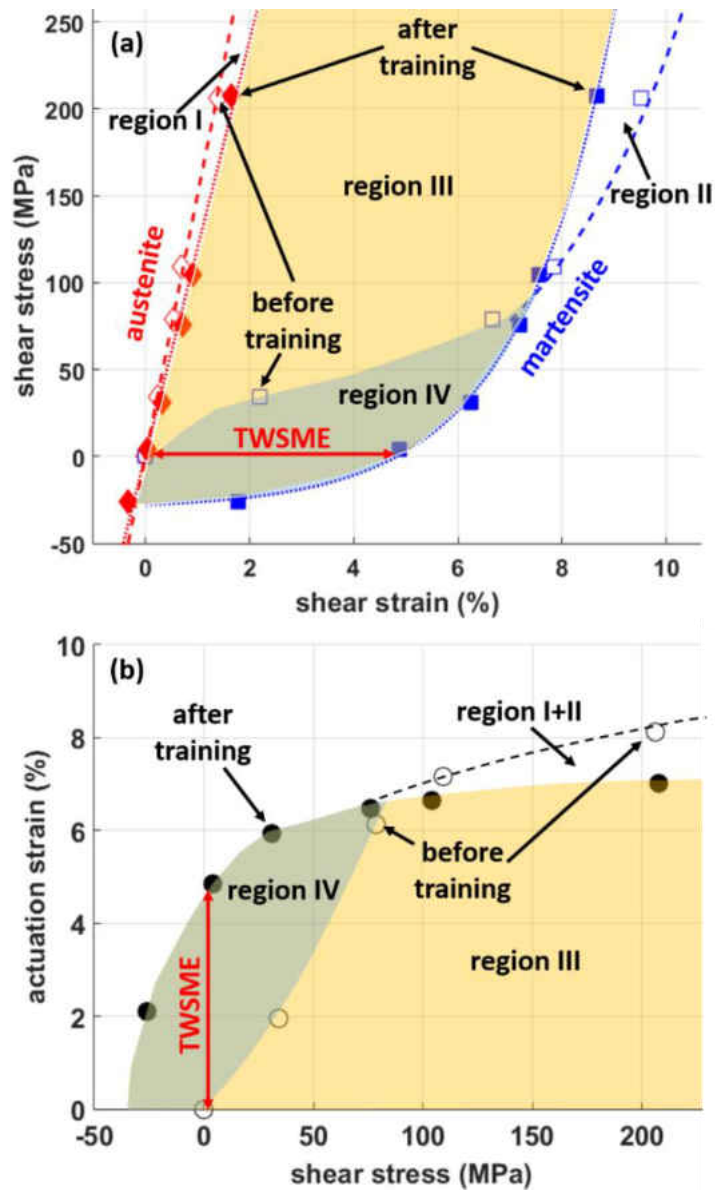
Figure 4.1: Operating space defined by the isobaric performance of a NiTi torsional actuator before and after training: a) shear strain at the UCT and LCT on the 2nd of two isobaric cycles at varying shear stresses; and b) actuation/transformation shear strain (i.e., the absolute difference between LCT and UCT points defined in Figure 4.1a).
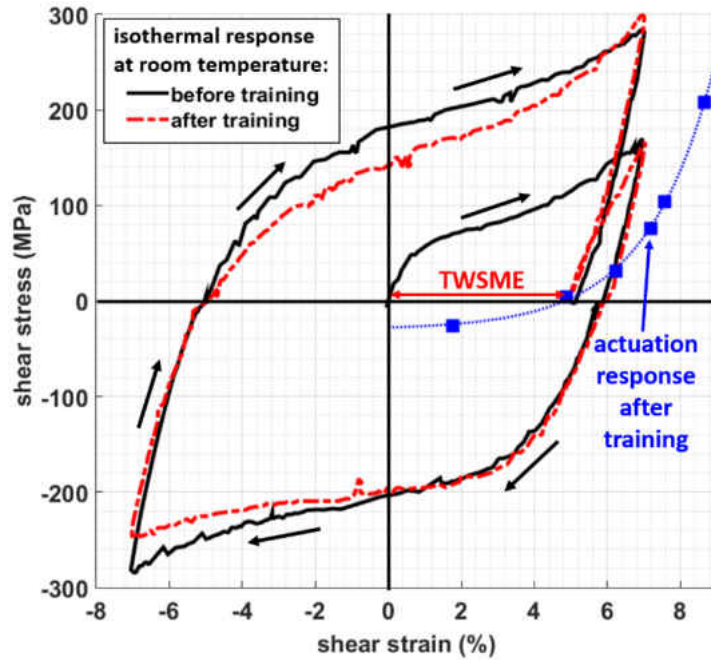
Figure 4.2: Isothermal forward and reverse loading (forward followed by reverse) to ±7% shear strain of a NiTi torsional actuator at room temperature prior to (as indicated by the black line) and following training (as indicated by the red "dashed" line). Also shown is the martensite actuation response after training from Figure 4.1a (as indicated by ■).
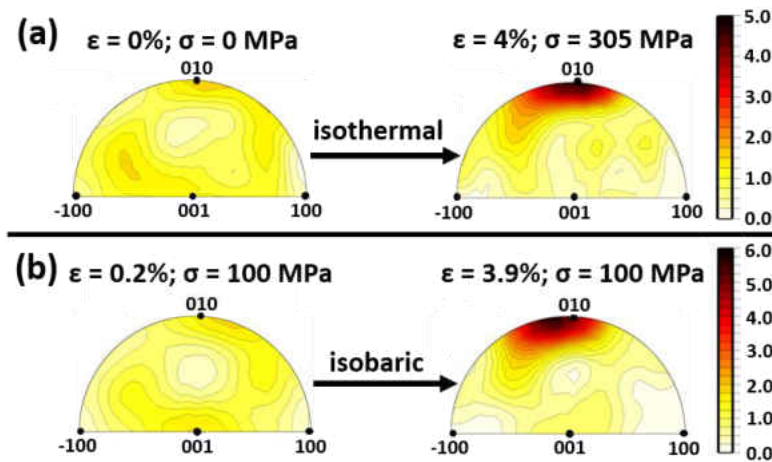
Figure 4.3: Representative variant reorientation and detwinning processes correlated to changes in textures observed through inverse pole figures: a) isothermal loading 4% tensile strain at room temperature; and b) isobaric loading under 100 MPa between 35°C and 165°C.
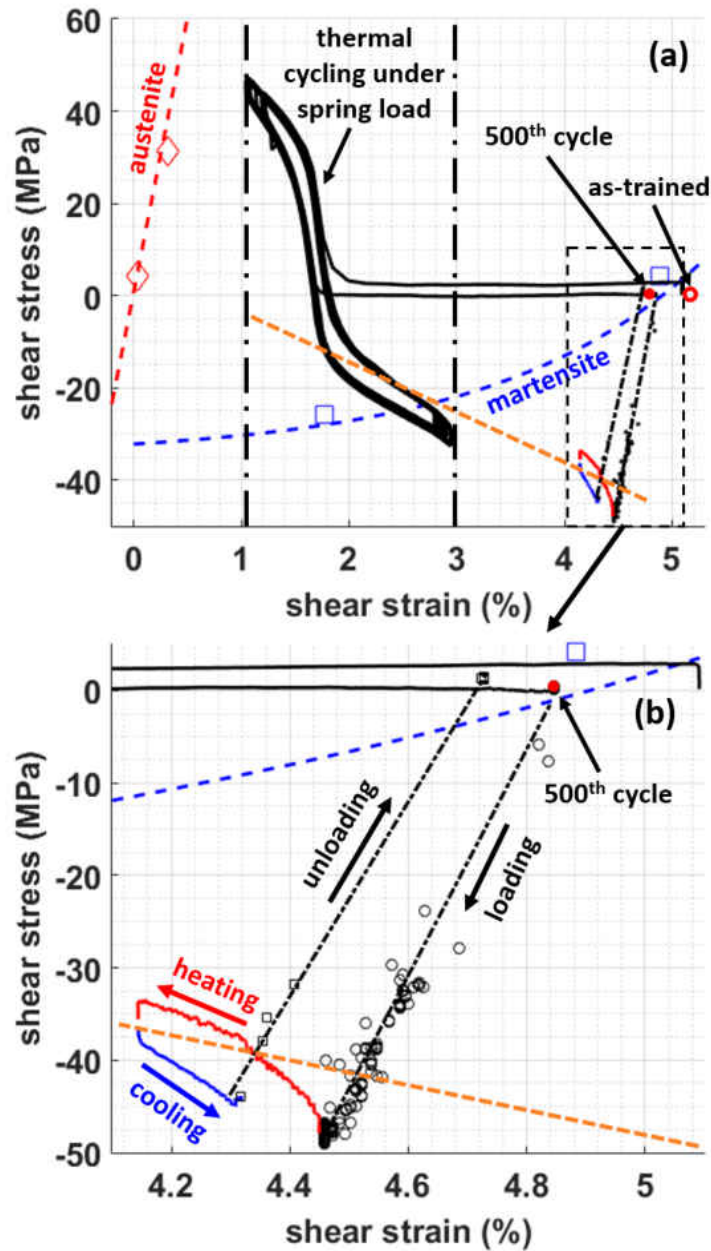
Figure 4.4: Application relevant load paths performed on a NiTi torsional actuator w.r.t. to the operating space shown in Figure 4.1: a) thermal cycling against positive and negative spring loads (up to 500 cycles); and b) isothermal loading beyond the operating space followed by heating and cooling.

49
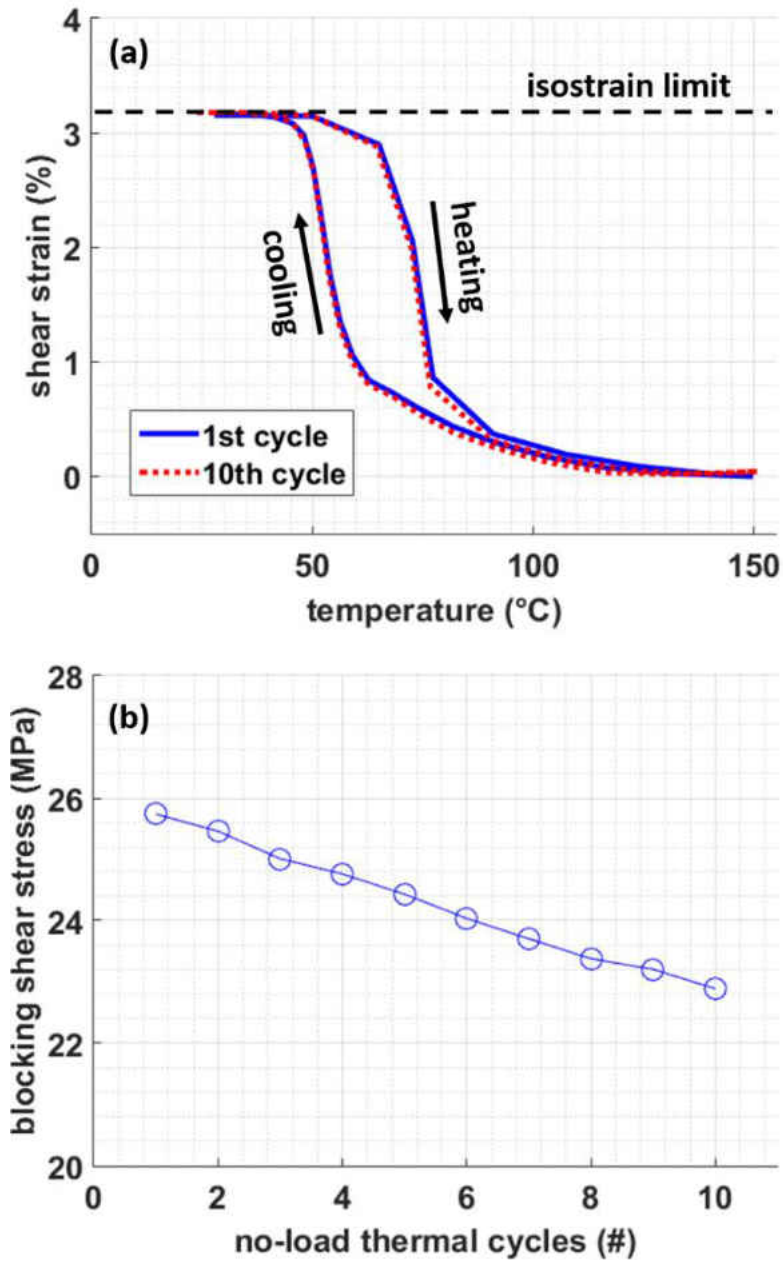
Figure 4.5: No-load thermal cycling (between 35 and 135°C) of a NiTi torsional actuator against a constant shear strain limit of 3.2%: a) shear strain-temperature response for 1st and 10th cycle and b) maximum blocking stress observed against the shear strain limit on each of the 10 cycles.

CHAPTER FIVE: ASYMMETRY AND CONTROL MODE EFFECTS DURING THERMOMECHANICAL LOADING OF POLYCRYSTALLINE SHAPE MEMORY NITI

Asymmetry and control mode effects in polycrystalline shape memory NiTi were investigated by recourse to in situ neutron and synchrotron x-ray diffraction performed during reverse mechanical loading and constant strain thermal cycling. Strain-controlled isothermal reverse loading (to ±4%) at room temperature demonstrated that preferred martensite variant selection correlated well with the macroscopic uniaxial strain and did not correlate with the compressive or tensile state of stress. During cyclic reverse loading (up to 10 cycles), no significant cycle-to-cycle evolution of the variant structure formed at a given strain was observed, despite cyclic hardening observed in the macroscopic stress-strain response. Stress-controlled cyclic reverse loading (to ±400 MPa for up to 10 cycles) showed that variant selection correlated well with strain that evolved (by cyclic hardening) during cycling. Additionally, thermal cycling (to above and below the phase transformation) under constant-strain (up to 2% tensile) showed that martensite variants structures correlated well with strain and did not evolve following thermal cycling, despite relaxation of stress in both martensite and austenite. Results are presented in context of variant reorientation and detwinning processes in martensitic NiTi and the fundamental thermoelastic nature of such processes. Discussion of the results is extended to include isobaric loading and inferences are made regarding the overall behavior of NiTi under general loading conditions.

5.1 Introduction

Polycrystalline NiTi shape memory alloys (SMAs) have the ability to recovery their pre-deformed shape against external loads as result of being heated through a reversible solid-state phase transformation from a low-symmetry B19' martensite phase to a higher-symmetry B2 austenite phase [4, 52, 53]. In the process of returning to the pre-deformed shape, SMAs can recover a considerable amount of deformation (up to 8% strain) against large stresses (up to 500 MPa). This ability to do work while transforming from one phase to another enables their use as high-force actuators with both sensory and actuation function [54]. To facilitate the implementation of SMAs in commercial applications a better understanding of relationship between isothermal, isostrain (thermal cycling under constant stress) and isobaric (thermal cycling under constant load) response and the associated effects of each control mode is required [32]. Asymmetry observed during reverse loading and the ability to obtain a similar microstructure though either isobaric or isothermal loading could be utilized to for designing optimal loading paths for processing and in application [7, 30]. The ability to take different paths yet still obtain the desired actuator response while minimizing irrecoverable deformation mechanisms could be utilized to minimize the number of cycles required to train an SMA, which limits the amount of work required for stabilizing their evolutionary response thereby increasing the fatigue life and overall durability of the SMA.

Tension-compression asymmetry in B19' NiTi is well known and has been studied extensively for both the monotonic [36] and cyclic [51, 55] responses. Deformation mechanisms which have been observed include elasticity, detwinning, variant reorientation and dislocation based plasticity, however the ability to quantify the contribution of each mechanism throughout

the response remains a challenge. At low strains (less than ~1%) elasticity of self-accommodated B19', detwinning and variant reorientation are all active deformation mechanisms. Progress in decoupling the contributions of each mechanism included the determination of the anisotropic elastic stiffness constants of B19' NiTi using *ab initio* calculations [56] and *in situ* neutron diffraction experiments [36]. From these diffraction experiments it was also determined that detwinning and variant reorientation processes can occur at strains less than 0.2%.

As tensile strain is increased (greater than ~1% and less than ~6%) detwinning and variant reorientation becomes the dominant deformation mechanism [36]. Inverse pole figures (IPFs) provided a qualitative assessment of texture. An increase in multiples of random distribution (MRD) near the $(010)_M$ and $(111)_M$ poles (w.r.t. the loading axis) was observed in tension and compression, respectively. Transmission electron microscopy (TEM) investigations showed that $\langle 011 \rangle_M$ type II and $(0\text{-}11)_M$ type I twinning are the dominant lattice invariant shears in this region [55, 57, 58]. Dislocations in both junction plane areas and martensite twin plates have been observed. At tensile strains greater than ~6% strain hardening occurs as a result of $(001)_M$ and $(20\text{-}1)_M$ deformation twins becoming active and increasing dislocation density [59]. As tensile strain continues to increase in tension (~6% to ~12%) an increase in MRD near the $(\text{-}150)_M$ and $(010)_M$ poles occurs [7]. At strains greater than ~12%, in MRD near the $(\text{-}150)_M$ and $(010)_M$ poles decreases and increases near the $(230)_M$ pole, possibly as a result of $(001)_M$ and $(20\text{-}1)_M$ deformation twins and dislocation based plasticity becoming the dominant deformation mechanisms.

During tension-compression (i.e., the case in which tension is applied first) cyclic loading in strain control up to ±4% strain it was shown by TEM that $\langle 011 \rangle_M$ type II twinning is the

primary lattice invariant shear before cycling while (11-1)$_M$ type I twinning is most frequently observed after cycling [55]. It was also reported that after cycling a high density of dislocations developed in both junction plane areas and within the martensite twins. It was concluded that these aforementioned deformation mechanisms contributed to the observed cyclic hardening.

Constant-strain thermally cycling of SMA; is most commonly implemented during the shape-setting process [40]; and can also be used to limit strain to increase the lifecycle of an SMA actuator [30] and in applications requiring large forces in compact areas [48], e.g., a static rock splitter for planetary exploration [60]. During *in situ* neutron diffraction shape-setting experiments of polycrystalline NiTi (49.9 at.% Ni), tensile strain (up to 7.3%) was at held constant while the specimen was thermally cycled (up to 450°C) [40]. While heating, blocking stresses were generated and reached a maximum of 400 MPa at 200°C and subsequently relaxed to near zero as heating continued to 450°C. At room temperature following the shape-set the specimen showed zero macroscopic stress and a self-accommodated microstructure (observed by recourse to IPFs). Constrain-strain thermal cycling (between 30 and 300°C) of in $Ni_{50.3}Ti_{29.7}Hf_{20}$ resulted in blocking stresses up to 1.5 GPa on the first cycle which decayed and saturated near 1.1 GPa following subsequent cycles (up to 20) [48].

The objective of the current work seeks to provide microstructural and macroscopic insight into asymmetry and control mode effects in shape memory NiTi. This is achieved by recourse to *in situ* neutron and synchrotron x-ray diffraction wherein information representative of the bulk, i.e., phase fraction, texture evolution and lattice strain, was followed during stress and strain-controlled isothermal reverse loading and constant-strain thermally cycling of near-equiatomic polycrystalline NiTi. Results are presented in context of variant reorientation and

detwinning processes in martensitic NiTi and the fundamental thermoelastic nature of such processes. Discussion of the results is extended to include isobaric loading and inferences are made regarding the behavior of shape memory NiTi under general loading conditions.

5.2 Experimental Procedures

5.2.1 Material

The material used in this work was a binary NiTi alloy (nominal composition 49.9 at.% Ni), produced by Special Metals (now SAES Smart Materials, New Hartford, NY). This alloy is part of suite of NiTi-based SMAs developed by NASA Glenn Research Center and has been extensively studied elsewhere [7, 36-39]. Ten-millimeter rods were produced in the hot-rolled/hot-drawn and hot-straightened condition. Transformation temperatures were determined by differential scanning calorimetry as follows: martensite finish (M_f), martensite start (M_s), austenite start (A_s) and austenite finish (A_f) to be 46, 71, 86 and 102±2°C, respectively.

5.2.2 *In situ* Neutron Diffraction

The following experiments were performed *in situ* in "time-of-flight" mode using SMARTS at LANL. The experimental setup at SMARTS is only summarized here and additional details can be found in Ref. [49] and in Section 2.2.1 in Chapter 2. Figure 5.1 shows the detector coverage at SMARTS that was utilized in the work presented in this chapter. In addition to the experimental setup described in Section 2.2.1 in Chapter 2, a more recently added third detector bank was utilized. The third detector bank (indicated by 3 in Figure 5.1) was positioned at a 30° angle below the plane formed by the other two detector banks and incident beam, at a 0° angle

(in-plane) relative to the incident beam. Results presented henceforth will correspond to reflections from lattices planes perpendicular to the loading axis unless otherwise stated.

Cylindrical dog-bone samples were machined to 5.08 mm in diameter and a 15.24 mm gauge length with threaded ends. Prior to all experiments two no-load thermal cycles between room temperature and 200°C were performed after installation into the load frame in order to insure an initial self-accommodated microstructure. Compression-tension (i.e., compression followed by tension) and tension-compression reverse cyclic (i.e., tension followed by compression) loading was performed in strain control to ±4% for 10 cycles at room temperature, on two respective specimens. Neutron diffraction spectra were acquired at 2% strain increments on the 1st, 2nd and final cycle. Tension-compression reverse cyclic loading reverse cyclic loading was performed in stress control to ±400 MPa for 10 cycles at room temperature, on a third specimen. Neutron diffraction spectra were acquired at ±400 MPa stress increments on the 1st, 2nd, 5th and final cycle. Constant-strain thermal cycling was performed on two specimens at 1 and 2% tensile strain, respectively. The specimens were loaded to their respective strains at room temperature in strain-control and then the strain was held constant while the specimen was thermally cycled between 40°C and 165°C for 10 cycles. Neutron diffraction spectra were acquired at lower cycle temperature (LCT) and upper cycle temperature (UCT) on the 1st, 2nd, 5th and final cycle. To insure adequate statistics for analysis a hold time of 30 min was used to acquire each spectrum. Extensometry (10 mm gauge length and strain resolution of $5x10^{-5}$) was used for macroscopic strain measurements. During strain and stress-controlled experiments a strain rate of 10^{-4} s^{-1} and stress rate of 40 MPa/min, respectively, was maintained. Table 1 summarizes by specimen, all of the experiments that were performed here.

Details regarding Rietveld refinement and IPFs can be found in Section 2.2.3 in Chapter 2. IPFs presented henceforth were generated from diffracting planes perpendicular to the loading direction, unless otherwise stated. Axial Distribution Plots (ADP) correspond to a radial slice (indicated by --- in Figure 5.1b) of the pole figure (cylindrical symmetry in the specimen was assumed) and provided a second representation of analyzing texture in this work. The ADP represents MRD (y-axis) of a specified crystallographic direction oriented at an angle (φ) between the normal to the specified plane and a chosen axis in the specimen, in this case the loading direction.

5.2.3 *In Situ* Synchrotron X-ray Diffraction

Additional constant-strain thermally cycling experiments were performed using *in situ* synchrotron x-ray diffraction at the High Energy Materials Science (HEMS) beam line at the high brilliance synchrotron radiation storage ring PETRA III at DESY in Hamburg, Germany. Details of the implementation of HEMS for investigations of NiTi-based alloys can be found in Ref. [61, 62] and are only summarized here. Measurements were taken with a photon energy of 100 KeV ($\lambda = 0.12427$ Å) using a beam cross-section of 500 x 500 μm^2 with a sample-to-detector distance of 1.572 m. Debye-Scherrer diffraction rings were capture using a MAR345 image plate detector (345 mm area diameter) with 100 mm pixel size. Diffraction spectra were generated by integrating diffraction rings over azimuthal intervals of 10° to insure adequate grain statistics.

Cylindrical compression specimens, 10 mm in length and 5 mm in diameter were loaded in displacement control using a BÄHR DIL805 dilatometer. One specimen was loaded in displacement control in compression to a strain (measured at the grips) of 0.6%, then specimen was held at constant displacement and thermally cycled between 40°C and 165°C (at a heating

and cooling rate of 10 °C/min) for five cycles. This specimen was included in the summary of all experiments in Table 1.

5.3 Results and Discussion

5.3.1 Strain-controlled Reverse Loading

Figure 5.2 shows IPFs corresponding to the first cycle of tension-compression (tension followed by compression) isothermal strain-controlled reverse loading of B19′ martensitic NiTi at room temperature. Initially at zero stress and strain a near self-accommodated microstructure was established as indicated by a maximum intensity of 1.74 in the corresponding IPF. Tensile loading of the specimen to 4% strain resulted in preferred selection of tensile variants as indicated by an increase in intensity (to a maximum of 5.06) near the 010 pole, observed in the corresponding IPF at 4%. Upon load reversal (from 4% back to 0% strain) preferred tensile variants reoriented back to near self-accommodated as indicated by a decrease in intensity (to a maximum of 2.11) observed in the corresponding IPF at 0%. Then, compressive loading of the specimen to -4% strain resulted in preferred selection of compression variants as indicated by an increase in intensity (to a maximum of 2.64) near the 111 pole, observed in the corresponding IPF at -4%. Upon load reversal (from -4% to 0% strain) preferred compression variants reoriented back to near self-accommodated as indicated by a decrease in intensity (to a maximum of 1.92) observed in the corresponding IPF at 0%. The ability to return a near self-accommodated microstructure following preferential selection of tensile and compressive variant demonstrates the isothermal reversibility of variant reorientation and detwinning in NiTi (within the limits investigated here). Overall, at 0% strain initially and following the 1st and 2nd load reversal a similar texture (as indicated by maximum intensities of 1.74, 2.11 and 1.92,

respectively) despite having significant differences in stress (i.e., 0, -299 and 268 MPa, respectively). This result demonstrates that martensite variant selection in NiTi correlates well with the macroscopic uniaxial strain and does not correlate with the compressive or tensile state of stress (within the limits investigated here).

At 2% strain on loading and unloading the maximum intensity observed in the corresponding IPFs was 3.21 and 3.61 (observed near the 010 pole), respectively. At -2% strain on loading and unloading the maximum intensity observed in the corresponding IPFs was 1.76 and 2.11 (observed near the 111 pole), respectively. The hysteresis observed, i.e., an increased amount of preferred variant selection on unloading verses loading, at an equivalent strain, was attributed to elastic unloading of martensite and the stress required to activate variant reorientation and detwinning processes upon load reversal.

Figure 5.3a shows the evolution of the stress-strain response for the first 10 cycles of compression-tension isothermal strain-controlled reverse loading (to $\pm$ 4% strain) of B19′ martensitic NiTi at room temperature. During cyclic strain-controlled reverse loading stress increased at maximum compressive and tensile strain values and decreased at intermediate strain values, which indicates strain hardening. Figure 5.3b shows the evolution of stress at the minimum and maximum strains of the first 10 cycles of isothermal strain-controlled reverse loading to $\pm$ 4% strain of B19′ martensitic NiTi at room temperature. Figure 5.3b shows an equivalent evolution in both tension-compression and compression-tension reverse loading, indicating the strain hardening behavior and overall evolution was independent of the initial loading direction. Cyclic strain hardening observed here was consistent with Ref. [55] wherein the observed behavior was attributed martensite variant reorientation, twin boundary movement

within martensite plates, formation of stacking faults on (001) planes, shear along (110) planes and the accumulation of dislocations in both junction plane areas and martensite twin plate.

Figure 5.4 shows the IPFs corresponding to the first 10 cycles of compression-tension isothermal strain-controlled reverse loading of B19′ martensitic NiTi at room temperature. Note that the IPFs shown in Figure 5.4 correspond to the macroscopic response shown in Figure 5.3a. At the following strains 0% initial, 4% compressive, 0% on the 1st load reversal (positive stress), 4% tensile and 0% on the 2nd load reversal (negative stress), the maximum intensities observed in corresponding IPFs were found to be 1.76, 3.00, 1.93, 5.18 and 2.30, respectively (comparable to 1.74, 2.64, 1.92, 5.06 and 2.11, respectively, at equivalent positions w.r.t. the tension-compression response as shown in Figure 5.2). This result provides additional validation that martensite variant structures were equivalent for corresponding strain whether the specimen was loaded in compression or tension and reversibility by isothermal deformation was realized when preferentially selected variants reverted back to self-accommodated when loading was reversed. Furthermore, these results are independent of the initial loading direction (i.e., compression-tension or tension-compression reverse loading).

At -4% strain on cycles 1, 2 and 10 maximum intensities (near the 111 pole) observed in the corresponding IPFs were 3.00, 2.60 and 2.37, respectively, and the corresponding stress values observed were -515, -588 and -646 MPa, respectively. At 4% strain on cycles 1, 2 and 10 maximum intensities (near the 010 pole) observed in the corresponding IPFs were 5.18, 4.98 and 5.02, respectively, and the corresponding stress values observed were 385, 435 and 532 MPa, respectively. At zero strain during unloading on cycles 1, 2 and 10 maximum intensities (near the 010 pole) observed in the corresponding IPFs were 1.76, 2.30 and 2.43, respectively, and the

corresponding stress values observed were 0, -234 and -162 MPa, respectively. At zero strain during loading on cycles 1, 2 and 10 maximum intensities (near the 010 pole) observed in the corresponding IPFs were 1.93, 1.99 and 2.28, respectively, and the corresponding stress values observed were 330, 278 and 219 MPa, respectively. Therefore, during cyclic strain-controlled reverse loading the maximum intensities observed in the corresponding IPFs; decreased at the maximum compressive strain; remained the same (within error) at the maximum tensile strain; and increased (during loading and unloading) at 0% strain with each cycle. Overall, the equivalence between strain and preferred variant selection and reversibility of such variant selection was unaffected. The subtle differences in maximum intensity observed in IPFs corresponding to an equivalent strain may be attributed to the following notions; i) elastic unloading of martensite and the stress required to activate variant reorientation and detwinning processes upon load reversal shifts the reference of the equivalent strain w.r.t. it's corresponding variant structure; and ii) martensite variants preferentially select (to a limited extent) to accommodate internal stresses that develop due to dislocation based plasticity (including the mechanisms described in Ref. [55]) during cycling.

5.3.2 Stress-controlled Reverse Loading

In order to provide additional insight into the effects of control mode on the deformation response stress-controlled reverse loading was also investigated. Figure 5.5 shows the IPFs corresponding to the first 10 cycles of tension-compression isothermal stress-controlled (to ±400MPa) reverse loading of B19′ martensitic NiTi at room temperature. During initial loading from 0 to 400 MPa, preferred tension variants were selected as indicated by an increase in maximum intensity in the corresponding IPF (Figure 5.5a, cycle 1) to 6.88 (near the 010 pole)

and corresponded to a strain of 5.7%. Upon reverse loading from 400 MPa to -400 MPa, variants reverted back to near self-accommodated as indicated by decrease in the maximum intensity observed in the corresponding IPF (Figure 5.5b, cycle 1) to 1.76 and corresponded to strain of -2.0%. The result that self-accommodation was observed near -2.0% strain as opposed to zero strain during unloading after a load reversal was also observed in the previous Section (IIIA) during stress-controlled reverse loading. This behavior was attributed to elastic unloading of martensite and the stress required to activate variant reorientation and detwinning processes upon load reversal.

Figure 5.6 shows the evolution of the stress-strain response for the first 10 cycles of tension-compression isothermal stress-controlled reverse loading (to ±400MPa) of B19′ martensitic NiTi at room temperature. During cyclic stress-controlled reverse loading strain hardening was observed as indicated by decreasing strain values at maximum tensile (400 MPa) and compressive (-400 MPa) stress values. The corresponding IPFs at (a) 400 MPa and (b) -400 MPa for cycles 1, 2, 5 and 10 are shown in Figure 5.5. At 400 MPa on cycles 1, 2, 5 and 10 maximum intensities (near the 010 pole) observed in the corresponding IPFs were 6.88, 6.05, 5.64 and 5.52, respectively, and the equivalent strains values observed were 5.8, 5.0, 4.5 and 4.3%, respectively. At -400 MPa on cycles 1, 2, 5 and 10 maximum intensities observed in the corresponding IPFs were 1.76, 1.73, 1.78 and 1.88, respectively, and the equivalent strains values observed were -2.0, -1.4, -1.0 and -0.9%, respectively. During cyclic (up to 10 cycles) stress-controlled reverse loading the maximum intensities observed in the corresponding IPFs decreased (near 010 pole) at the maximum tensile stress (400 MPa) and remained the same (within error) at the maximum compressive stress (-400 MPa).

During cycling, at the maximum tensile stress (400 MPa) of each cycle, a decreasing maximum intensity observed in the IPFs correlated well with decreasing macroscopic strain. This result was consistent with the correlations between variant selection and macroscopic strain observed during strain-controlled reverse loading (presented in Section IIIa). At the maximum compressive stress the variant structure remained near self-accommodated during cycling despite strain decreasing compressive strain. This result can be attributed to the strain required activate variant reorientation and detwinning upon load reversal and elastic unloading of martensite which may shift the reference of the equivalency relationship between macroscopic strain and martensite variant selection.

5.3.3 Constant Strain Thermal Cycling

Isobaric and Isothermal of shape memory NiTi have been extensively investigated however isostrain (thermal cycling under constant strain) loading has been limited to a few investigations, e.g., those in Ref. [40, 48]. Constant strain thermal was investigated here and results are presented in context of isothermal loading results from previous sections. Figure 5.7a shows the macroscopic stress temperature response during thermal cycling between 40°C and 165°C under a constant strain of 2%. Initial isothermal loading from zero to 2% tensile strain (from points 1 to 2) at room temperature produced a macroscopic stress of 261 MPa. The specimen was held at constant strain of 2% (in strain control) and heated (from points 2 to 3) to a UCT = 165°C producing a blocking stress of 440 MPa. In order to insure adequate statistics for the diffraction spectra the specimen was held at the UCT for 30 min. During this time a relaxation of stress occurred as observed in Figure 5.7a. The specimen was then cooled (from

points 3 to 4) to an LCT = 40°C which relaxed the stress to -14.7 MPa, thus completing the first cycle.

Figure 5.8 shows the IPFs corresponding to thermal cycling between 40°C and 165°C under a constant strain of 2%. Upon initial isothermal loading (from points 1 to 2) to 2% strain preferred tensile variant selection was observed in the corresponding IPF as indicated by an increase in maximum intensity to 3.57 (compared to 3.21 observed at 2% tensile strain on initial loading in Figure 5.2) near the 010 pole. Following the first heating and cooling cycle this preferred martensite variant structure was not significantly affected as indicated by a maximum intensity of 3.21 (near the 010 pole) observed in the corresponding IPF, despite a significant relaxation in stress (from 261 MPa to -14.1 MPa). This result demonstrates that the martensite variant structure formed by isothermal loading was equivalent to given strain and the equivalency was not affected by thermal cycling under constant strain, despite large changes in the macroscopic state of stress. The relaxation of stress and decrease in maximum intensity observed in the IPFs can be attributed to martensite variants self-accommodating to the applied stress state during cooling.

Figure 5.7b shows the blocking stress observed at the LCT and UCT of each cycle during 10 thermal cycles under a constant strain of 2%. Following the first thermal cycle, the stress at the LCT had decreased to -14.7 MPa. This decreased stress value remained unchanged (within error) over the next 10 cycles. On the first thermal cycle, at the UCT, a blocking stress of 440 MPa was observed. During the next 10 cycles the blocking stress decreased with each cycle. While the rate of decrease slowed with each cycle this behavior did not appear to saturate for the number of cycles performed here. To explore possible mechanisms for the observed stress

relaxation with cycling the texture in B2 was investigated by recourse to IPFs. Figure 5.9 shows IPFs for B2 austenite taken at the UCT of each during thermal cycling (up to 10 cycles) between 40°C and 165°C under a constant strain of 2%. On the first cycle a maximum intensity of 1.68 was observed near the 110 pole in the corresponding IPF. The increased intensity near the 110 pole indicates a 110 fiber texture (assuming axial symmetry) in austenite. The texture observed here was most likely developed during process and was considered to be weak. The maximum intensity observed in the IPFs on cycles 1, 2, 5 and 10 (with corresponding stress of 440, 406, 343 and 304 MPa, respectively) at the UCT was found to be 1.68, 1.70, 1.75 and 1.79, respectively. Therefore, over the 10 thermal cycles under constant strain the texture in B2 remained unchanged (within error), despite a significant decrease in macroscopic stress. The decrease in stress could possibly be attributed to slip which should not produce a noticeable texture change (for strains up to 10%)[47].

The set of *in situ* neutron diffraction experiments performed during thermal cycling under a constant strain of 2% were repeated at 1% strain (for 5 cycles). The blocking stress at the LCT and UCT for constant strain thermal cycling at 1% strain can be seen in Figure 5.7b. The corresponding IPFs for B19′ taken at the LCT of each cycle can be seen in Figure 5.8. Overall, the response observed for 1% constant strain thermal cycling is comparable to the 2% case when the martensite variant structure and strain equivalence is considered. The corresponding IPFs for B2 taken at the UCT of each cycle can be seen in Figure 5.9. The maximum intensity observed in the IPFs during each cycle of the 1% was slightly lower than that which was observed for the 2% case. The slight texture increase for 2% case over the 1% case could be a result of twinning in B2. A comparable increase in maximum intensity observed in IPFs (near the 110 pole) during

isothermal loading of B2 have been observed in Ref. [47] and in this case was attributed to possible twinning and/or slip in B2.

To investigate further, constant strain thermal cycling at a lower constant strain value of 0.6% using in situ synchrotron x-ray diffraction. A lower strain value was chosen to reduce the contributions of variant and reorientation detwinning to the overall response and subsequently reveal other potential mechanisms. Additionally, synchrotron x-ray diffraction provided adequate diffraction statistics on the order of seconds as opposed to minutes compared to neutron diffraction thus eliminating possible time-dependent contributions, e.g. those contributing to stress relaxation observed at the UCT during neutron diffraction experiments. Figure 5.7a shows the macroscopic stress-temperature response during thermal cycling between 40°C and 165°C under a constant strain of 0.6% performed in situ using synchrotron x-ray diffraction. Note, no holding time at the UCT was required therefore no stress relaxation occurred due to holding. Figure 5.7b shows that the cycle-to-cycle relaxation of stress at the UCT for the ε=0.6 % case was significant, as the stress had decreased from 149.8 to 122.6 over 10 thermal cycles.

Figure 5.10 shows synchrotron x-ray diffraction spectra from diffracting planes perpendicular to the loading direction (azimuthal angle, ψ = 90°) at 165°C acquired during thermal cycling between 40°C and 165°C under a constant strain of 0.6% for select B2 peaks. Also, shown are the spectra acquired from the second no-load thermal cycle, at the UCT. Results show lattice strain indicated by peak shift between the no-load thermal cycle and subsequent thermal cycles under constant. This is expected and can be attributed to elastic loading of B2 under the blocking stress generated during the thermal cycling under constant strain. From cycles 1 to 5 no changes in peak intensity and no peak broadening or shifting was observed. Figure 5.11

shows the normalized intensities (I/I_0) of select B2 peaks at 165°C as a function of azimuthal

angle ψ (in 10° increments) during thermal cycling (up to 5 cycles) between 40°C and 165°C

under a constant strain of 0.6%. The 110 fiber texture can clearly be observed as peaks in 110

intensity near azimuthal angles 90° and 270°, both of which angles correspond to the

longitudinal direction in the specimen. No cycle-to-cycle change in intensity over the range of

azimuthal angles was observed (for all crystallographic directions shown here) which indicates

that no B2 texture changes occurred during cycling, despite a significant relaxation in the

macroscopic blocking stress. Overall, no changes in texture or peak broadening were observed

despite having a significant relaxation in stress (at the UCT of each cycle) during constant strain

thermal cycling (as shown in Figure 5.7b for the ε=0.6 % case). These results further point to

possible slip in B2, as was observed during isothermal and isobaric cycling of shape memory

NiTi in Refs. [47] and [43], respectively.

5.4 Inferences

Bain strains between B2 and B19′ were calculated here (as done previously in Refs. [4, 5,

44] using lattice parameters obtained here by Rietveld refinement) by recourse to

crystallographic theory for this alloy. The lattice parameters obtained by Rietveld refinement

were a = 2.91 Å, b = 4.65 Å, c = 4.13 Å and γ = 97.75 for monoclinic martensite and $d_{100,B2}$ =

3.03 for cubic austenite. The monoclinic angle is chosen to be between the minimum and

maximum lattice vector lengths. Typically in other literature b is chosen to be along the diad axis

which makes β the monoclinic angle. To be consistent with the output of the Rietveld

refinements generated by GSAS and corresponding IPFs, c was chosen to be along the diad axis

and γ becomes the monoclinic angle. The transformation matrix between the monoclinic martensite and cubic austenite is given by:

$$G = \begin{bmatrix} \dfrac{a}{d_{100,B2}} & \dfrac{b\cos(\gamma)}{\sqrt{2}d_{100,B2}} & 0 \\ 0 & \dfrac{b\sin(\gamma)}{\sqrt{2}d_{100,B2}} & 0 \\ 0 & 0 & \dfrac{c}{\sqrt{2}d_{100,B2}} \end{bmatrix}$$

(4.1)

and the transformation strain is given by:

$$\varepsilon_{hkl}^{var} = \frac{\left|RGR^{-1} \cdot v\right| - \left|v\right|}{\left|v\right|}$$

(4.2)

$$v = \begin{bmatrix} h \\ k \\ l \end{bmatrix}$$

where R is the rotation matrix and . The transformation strains determined by equations 4.1 and 4.2 were then mapped into the monoclinic IPF (as previously done in Refs. [44, 63], using transformation strains calculated from lattice parameters obtained here) as shown in Figure 5.12a. The Matlab script used to perform this calculation and to generate Figure 5.12a can be found in Appendix A-1.

The maximum tensile (~ 11% strain) and compressive (~ -7% strain) transformation strains occur near the -120 and 210 poles (as shown), respectively. To facilitate the following discussion Figure 5.12b shows representative IPFs (generated from lattice planes perpendicular to the loading direction) demonstrating preferred selection of martensite variants in polycrystalline specimen under of tensile and compressive uniaxial loading (as established in Figure 5.2). Ref. [64] showed that martensite variant conversion occurs in manner such that

correspondent variants which produce the largest conversion strains, will grow at the expense of others in order to maximize macroscopic strain (under applied stress) in the polycrystalline aggregate (and was later noted and demonstrated for NiTi in Refs. [44] and [53]). This notion can also be observed here in IPFs presented in Figure 5.12. Preferred variant selection under tensile loading was indicated by an increase in pole density near the 010 direction (as shown in Figure 5.7b) and the maximum variant conversion strain (~ 12%) was observed near the -120 direction (as shown in Figure 5.7a). Likewise, preferred variant selection under compressive loading was indicated by an increase in pole density near the 111 direction (as shown in Figure 5.7b) and the maximum variant conversion strain (~ -7%) was observed near the 210 direction (as shown in Figure 5.7a). The slight rotation between the observed preferred direction for variant selection (in the polycrystalline aggregate) and that of calculated maximum variant conversion strains can be attributed to intergranular interaction/constraint and the requirement to satisfy strain compatibility.

Figure 5.13 shows IPFs corresponding to diffracting planes with plane normal at $\Phi = 46.3°$ relative to the loading direction during the first cycle of isothermal tensile followed by compressive strain-controlled reverse loading of B19′ martensitic NiTi at room temperature. Note, the IPFs presented here were generated from Rietveld refinements of diffraction spectra captured by detector Bank 3 (as illustrated in Figure 5.1). Tensile loading of the specimen to 4% strain resulted in preferred selection of martensite variants in specimen directions that have minimal normal stress, as indicated by an increase in intensity (to a maximum of 2.53) near the 141 pole, observed in the corresponding IPF. This result further confirms the dependency between variant selection and strain and lack of correlation between variant selection and stress,

as martensite variants preferentially select (in specimen directions with minimal stress) to satisfy strain compatibility. Also note that the calculated conversion strains near the 141 pole are intermediate (as opposed to maximum) tensile values, as shown in Figure 5.12a. This result suggest that variants which maximize strain, are preferentially selecting to the direction of applied stress and those variants that are less favorable (i.e., variants that produce intermediate or minimal conversion strain values) are left available to reorient to accommodate intergranular constraint and strain compatibility. This behavior can be summarized through ADPs wherein MRD (y-axis) of a specified crystallographic direction are represented over a range of specimen directions (between loading and transverse direction for the case of Figure 5.14).

Figure 5.14a shows the ADPs for the 010 direction corresponding to the first cycle of tension followed by compression isothermal reverse loading of B19′ martensitic NiTi at room temperature. The ADPs presented here have three points of constraint, at $\Phi = 0°$ (loading direction), 46.3° and 90° (transverse direction) which correspond to detector banks 2, 3 and 1, respectively. The macroscopic response and IPFs corresponding to the loading direction ($\Phi = 0°$); and the IPFs corresponding to ($\Phi = 46.3°$) can be seen in Figure 5.2 and Figure 5.13, respectively. In Figure 5.14a, preferential martensite variant selection was observed as indicated by an increased and decreased intensity at $\Phi = 0°$ and $\Phi = 90°$, respectively as the specimen was strained to 4% tensile strain. This indicates the 010 crystallographic direction corresponds to preferred tensile variants and the result is consistent with those observed in the IPFs in Figure 5.2. At 4% tensile strain the decreased intensity at $\Phi = 90°$ caused by a reduction due to Poisson's ratio in the transverse direction. Upon load reversal (from 4% back to -4% strain) preferred tensile variants reoriented to preferred compression variants as indicated by a

decreased and increased intensity at $\Phi = 0°$ and $\Phi = 90°$, respectively. Figure 5.14b shows the ADPs for the 111 direction which corresponds to preferred compression variants (as was demonstrated in Figure 5.2). During this reverse loading (from 4% back to -4% strain) compression preferred variants grew at the expense of tension preferred variants, as indicated by an increased and decreased intensity at $\Phi = 0°$ and $\Phi = 90°$, respectively, in the ADP for the 111 direction. Upon the second load reversal (returning back to 0% from -4% strain) variant structure returned to near self-accommodated state as indicated by good agreement between 0% initial and 0% final strain, in both Figure5.14a and 5.14b. Also note that in both ADPs, corresponding to the 010 and 111 crystallographic directions, negligible changes were observed near $\Phi = 46.3°$. Overall, results observed through the ADPs provided additional evidence that variants which maximize strain, are preferentially selecting to the direction of applied stress at the expense of variants that are less favorable (or those which produce less variant conversion strain), in the polycrystalline aggregate.

5.5 Conclusions

Asymmetry and control mode effects in polycrystalline shape memory NiTi was investigated by recourse to *in situ* neutron and synchrotron x-ray diffraction performed during reverse mechanical loading and constant strain thermal cycling. *In situ* neutron and synchrotron x-ray diffraction, provided information representative of the bulk, i.e., phase fraction, texture evolution and lattice strain, was tracked during stress- and strain-controlled isothermal reverse loading and constant-strain thermally cycling of shape memory polycrystalline NiTi. Results were discussed in context of fundamental thermoelastic mechanisms in NiTi and the following conclusions were made.

1.) Reverse isothermal loading of martensite demonstrated that preferred martensite variant selection correlated with the macroscopic uniaxial strain and did not correlate with the compressive or tensile state of stress. Furthermore, variant structures were equivalent for the corresponding strain and more importantly, the reversibility and equivalency was immediately evident in a variant structure when variants reoriented to near self-accommodated when the load was reversed and macroscopic strain was returned to zero.

2.) During cyclic stress- and strain-controlled reverse isothermal loading cycling hardening was observed as maximum strain values decreased and stress values increased, with each cycle, in respective control modes. Despite evolution stress and strain conclusion (1) was maintained during isothermal cycling.

3.) During thermal cycling under constant-strain (up to 2% tensile) the maximum stress values decreased to zero at the LCT and gradually decreased with each cycle at the UCT. Despite relaxation of stress in both martensite and austenite conclusion (1) was maintained during constant strain thermal cycling. Additionally, no microstructural changes (specifically, of texture) were observed in the B2 phase during cycling, which pointed possible slip.

Isobaric loading (thermal cycling under constant stress) has been shown to abide with conclusion (1) (see Refs. [10, 44, 63], among others) w.r.t. preferred martensite variant selection. Furthermore, variant structures formed isobarically, were then reversed to near self-accommodated by isothermal loading in Ref. [65]. Overall, various thermomechanical combinations of heating and loading sequences in SMAs that yield the same preferred selection

of martensite variants demonstrates the ability to take different paths yet still obtain the desired response while minimizing irrecoverable deformation mechanisms. These conclusions have implications on minimizing the number of cycles required to train an SMA, which limits the amount of work required for stabilizing their evolutionary response thereby increasing the fatigue life and overall durability of the SMA. Therefore, the loading and heating path which minimizes the activation of irrecoverable processes and most efficiently produces the desired actuation response should be considered in the actuator design and fabrication process.

5.6 Figures
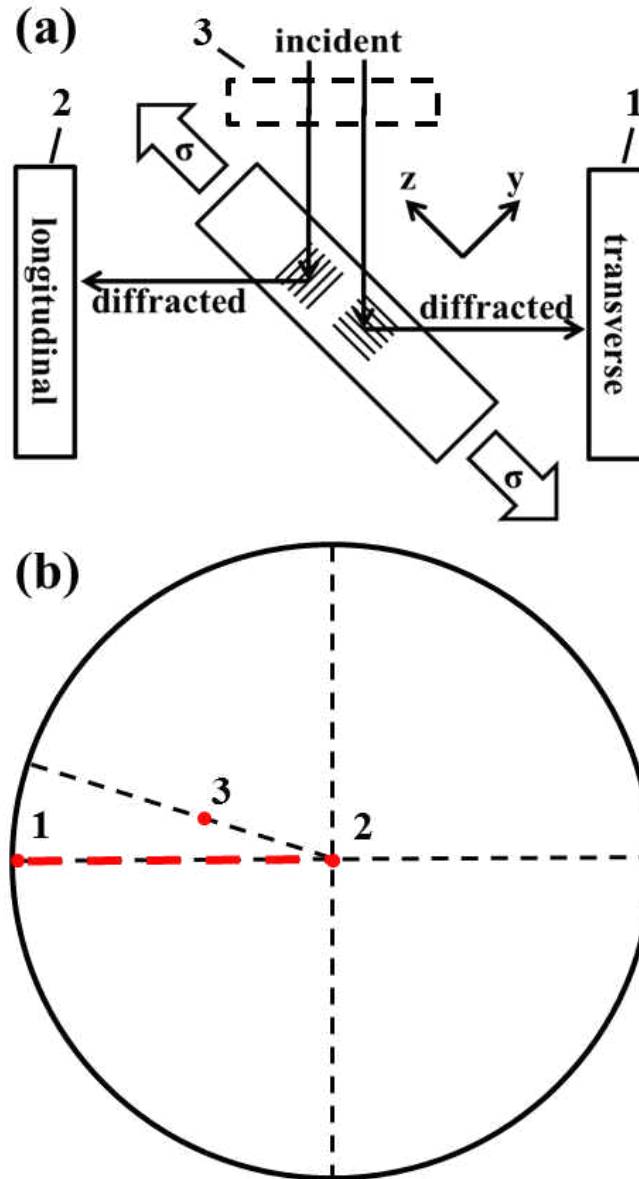
Figure 5.1: Detector coverage at SMARTS: (a) schematic of physical location w.r.t. incident and diffracted beams, and specimen; and (b) projected into a pole figure. All axial distribution plots generated in this paper correspond to the radial slice indicated by ---.
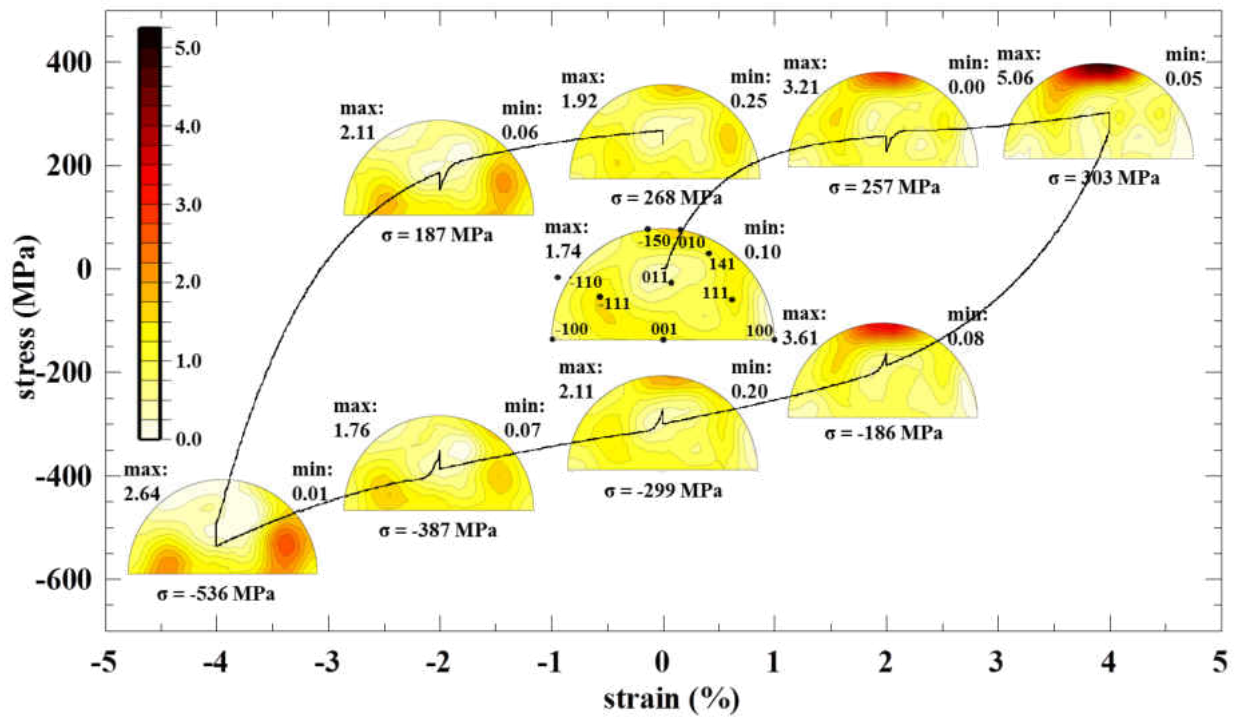
Figure 5.2: Inverse pole figures corresponding to diffracting planes perpendicular to the loading direction during the first cycle of tension-compression (i.e., tensile followed by compressive) isothermal strain-controlled reverse loading of B19′ martensitic NiTi at room temperature. For clarity in presentation, the scale chosen is unique to this figure.
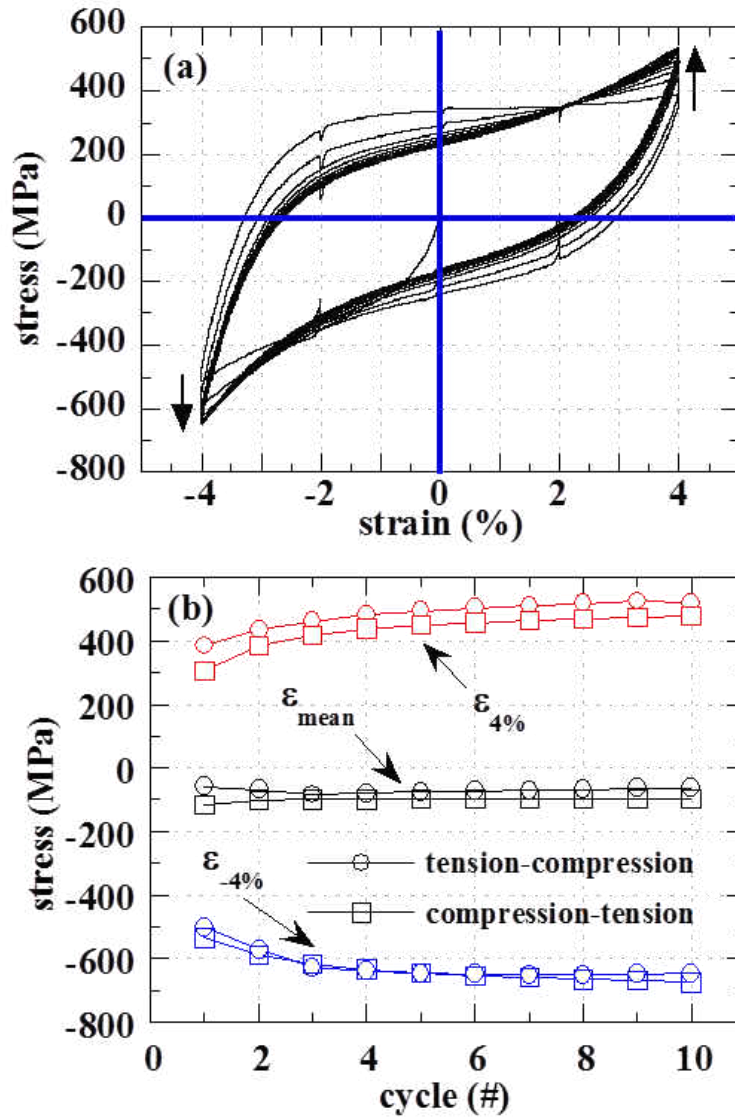
Figure 5.3: Evolutionary response of the first 10 cycles of isothermal strain-controlled reverse loading of B19′ martensitic NiTi at room temperature: (a) stress-strain response for compressive followed tensile loading and (b) stress at +/- 4% strain for both tensile followed by compressive and compressive followed by tensile loading.
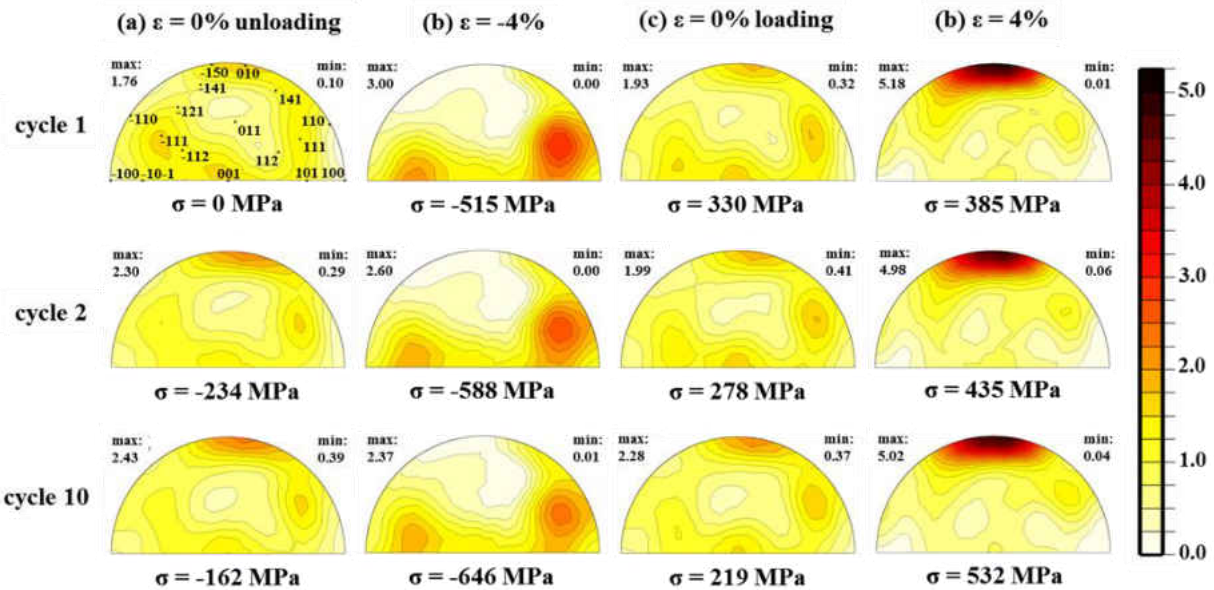
Figure 5.4: Inverse pole figures corresponding to diffracting planes perpendicular to the loading direction during the first 10 cycles of compressive followed by tensile isothermal strain-controlled reverse loading of B19′ martensitic NiTi at room temperature at: (a) ε = 0% strain for the initial point on cycle 1 and on the unloading curve for cycles 2 and 10; (b) ε = -4%; (c) ε = 4% and (d) ε = 0% strain on the loading curve. Note, the IPFs presented in this figure correspond the macroscopic response shown in Figure 5.2a. For clarity in presentation, the scale chosen is unique to this figure.
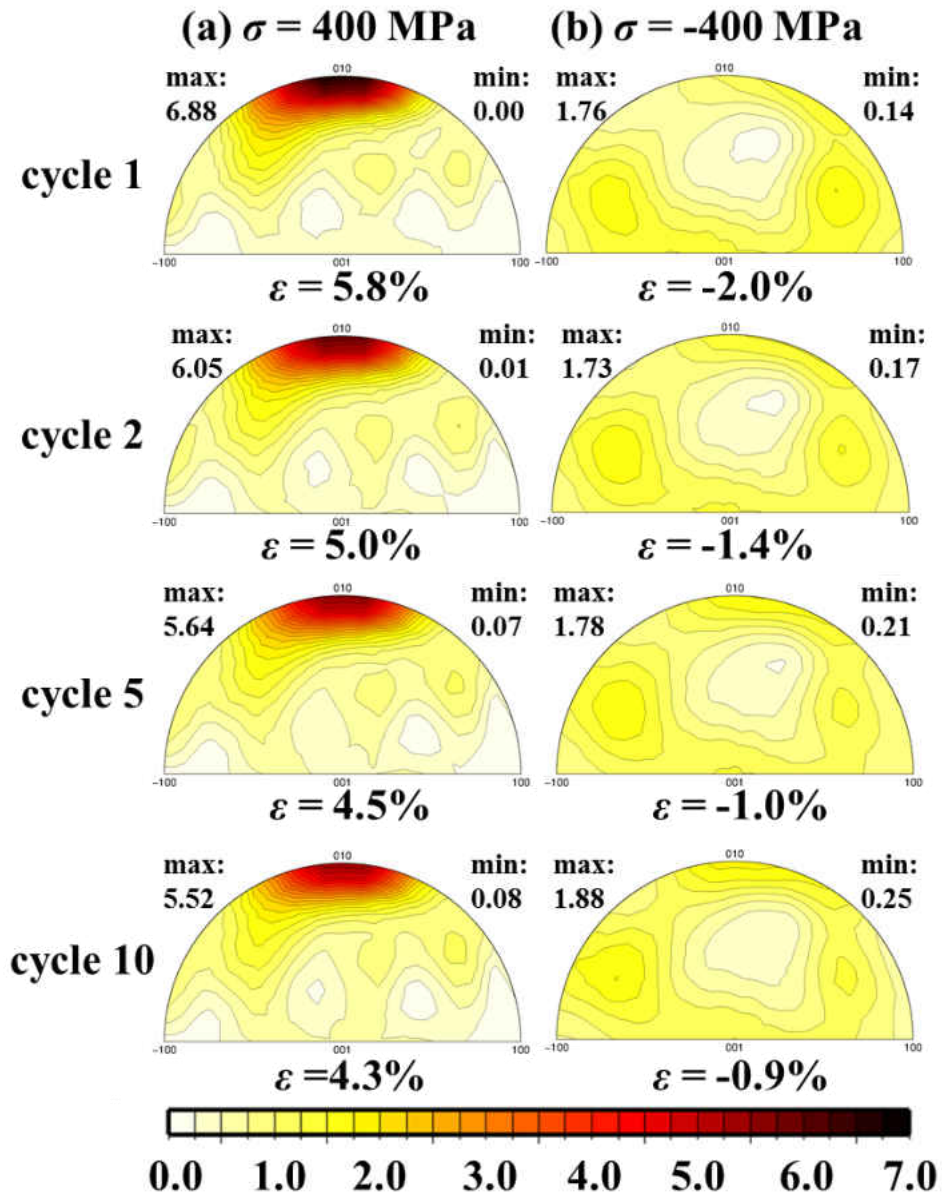
Figure 5.5: Inverse pole figures corresponding to diffracting planes perpendicular to the loading direction during the first 10 cycles of tensile followed by compressive isothermal stress-controlled reverse loading of B19′ martensitic NiTi at room temperature at: (a) σ = 400 MPa and (b) σ = -400 MPa stress. Note, the IPFs presented in this figure correspond the macroscopic response shown in Figure 5. For clarity in presentation, the scale chosen is unique to this figure.
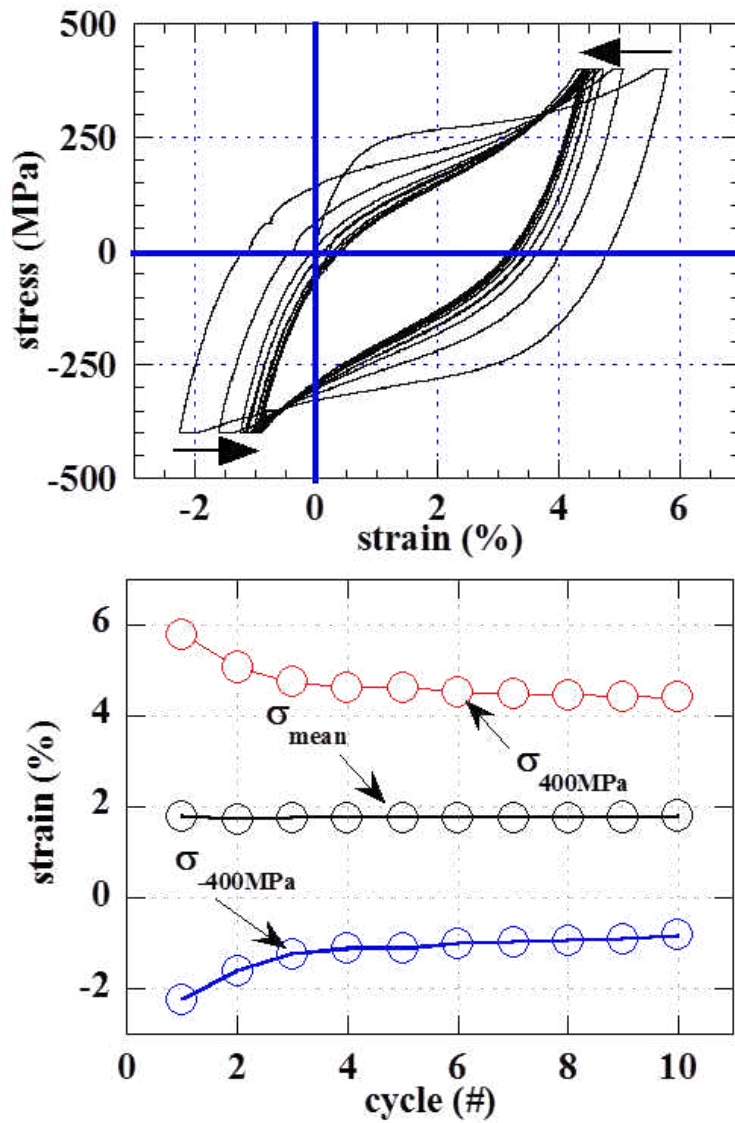
Figure 5.6: Evolutionary response of the first 10 cycles of isothermal tensile followed by compressive stress-controlled reverse loading of B19′ martensitic NiTi at room temperature: (a) stress-strain response and (b) strain at +/- 400 MPa.
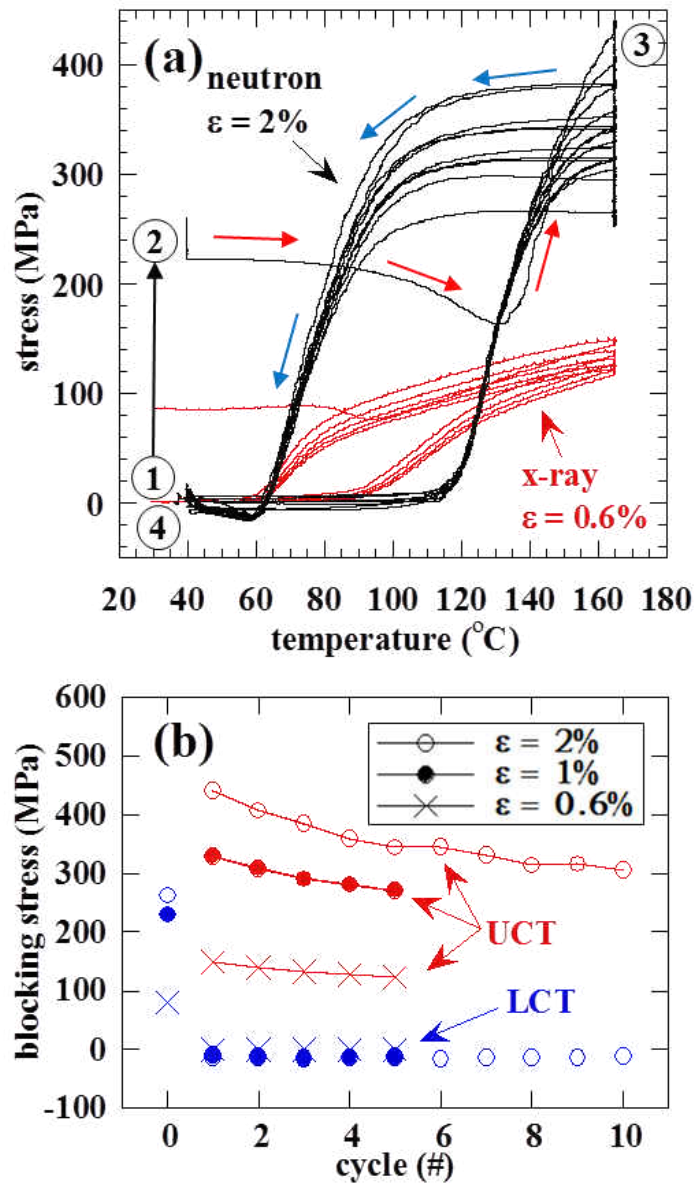
Figure 5.7: Thermal cycling between 40°C and 165°C under constant strain of shape memory NiTi: (a) stress-temperature response with 2% and 0.6% pre-strain performed at SMARTS and HEMS (see text for details on the diffraction instruments used), respectively and (b) blocking stress at the LCT and UCT verse cycle (#) for all cases.
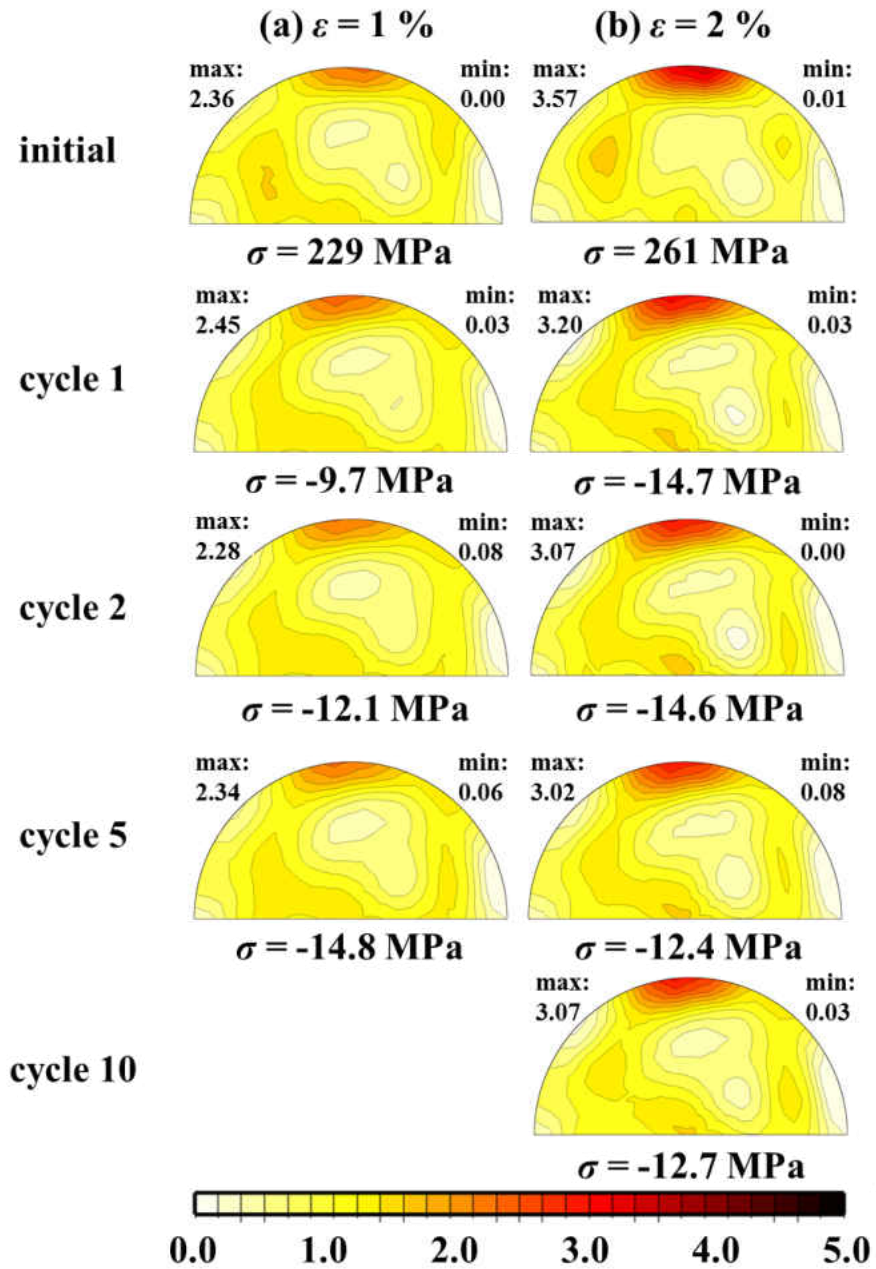
Figure 5.8: Inverse pole figures (of the B19′ phase at 40°C) corresponding to diffracting planes perpendicular to the loading direction during thermal cycling (up to 10 cycles) between 40°C and 165°C under a constant strain of (a) 1% and (b) 2%. For clarity in presentation, the scale chosen is unique to this figure.

(a) ε = 1 %

(b) ε = 2 %

cycle 1

σ =329 MPa
max: 1.53
min: 0.33

σ =440 MPa
max: 1.67
min: 0.33

cycle 2

σ = 308 MPa
max: 1.51
min: 0.32

σ = 406 MPa
max: 1.70
min: 0.30

cycle 5

σ = 270 MPa
max: 1.51
min: 0.31

σ = 343 MPa
max: 1.75
min: 0.26

cycle 10

σ = 304 MPa
max: 1.79
min: 0.22

0.0   1.0   2.0
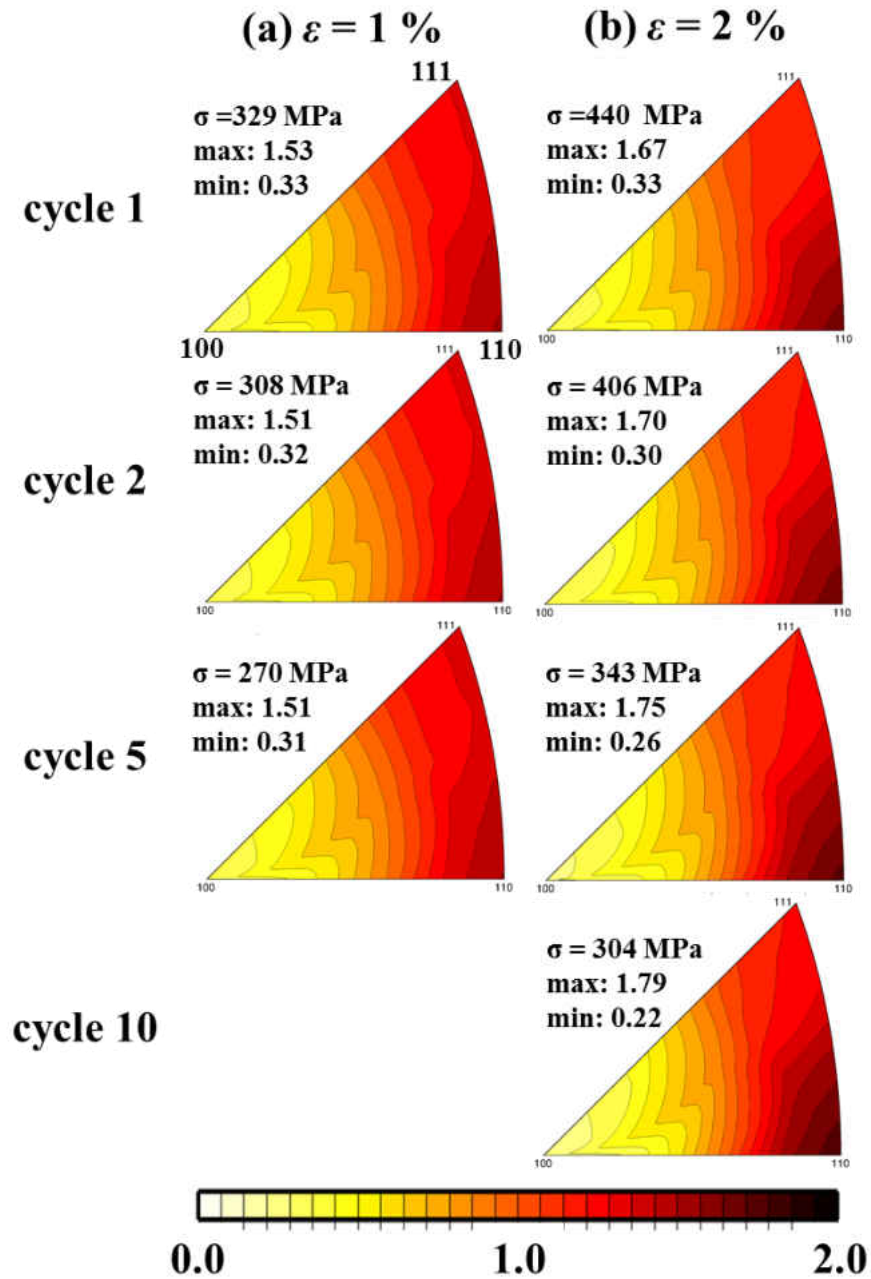
Figure 5.9: Inverse pole figures (of the B2 phase at 165°C) corresponding to diffracting planes perpendicular to the loading direction during thermal cycling (up to 10 cycles) between 40°C and 165°C under a constant strain of (a) 1% and (b) 2%, presenting. For clarity in presentation, the scale chosen is unique to this figure.
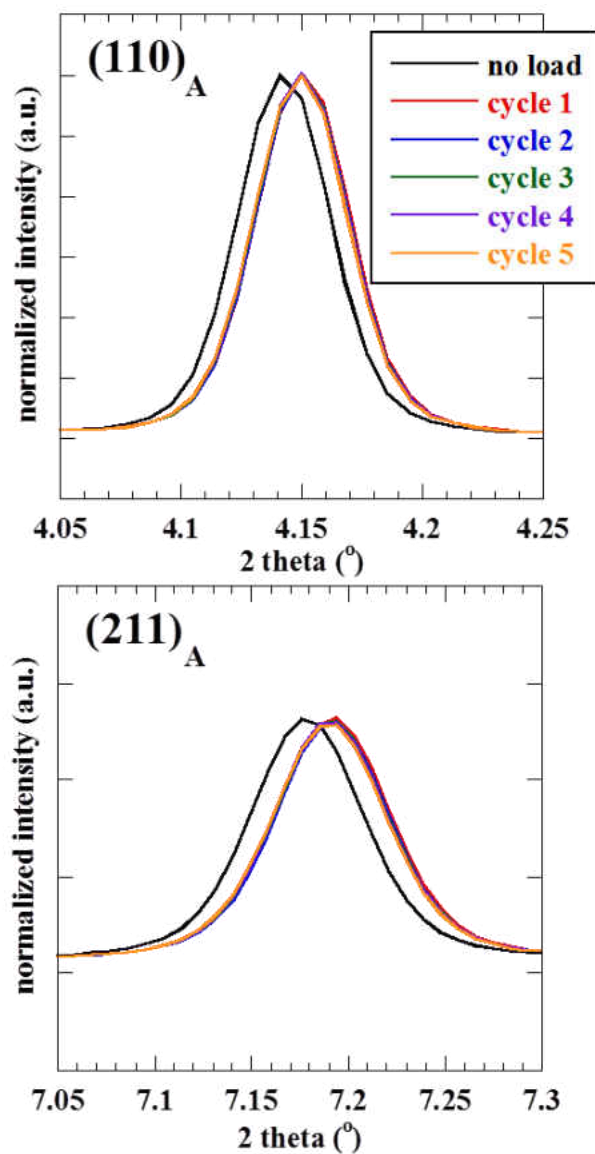
Figure 5.10: *In situ* synchrotron x-ray diffraction spectra corresponding to diffracting planes perpendicular to the loading direction (azimuthal angle, $\psi = 90°$) at 165°C during thermal cycling between 40°C and 165°C under a constant strain of 0.6% for select B2 peaks.
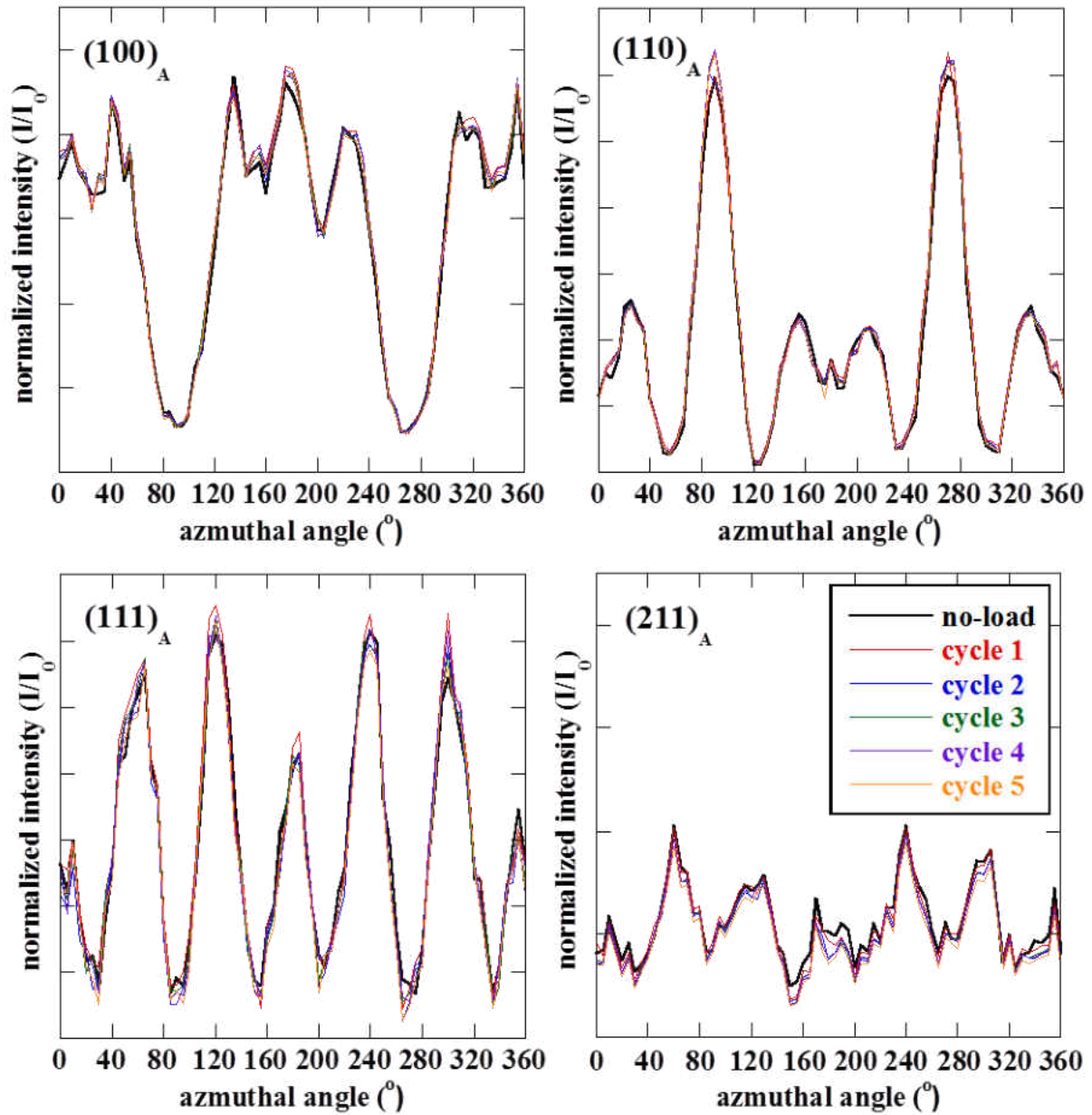
Figure 5.11: Normalized intensities (I/I_0) of select B2 peaks at 165°C as a function of azimuthal angle ψ (in 10° increments) during thermal cycling (up to 5 cycles) between 40°C and 165°C under a constant strain of 0.6%.
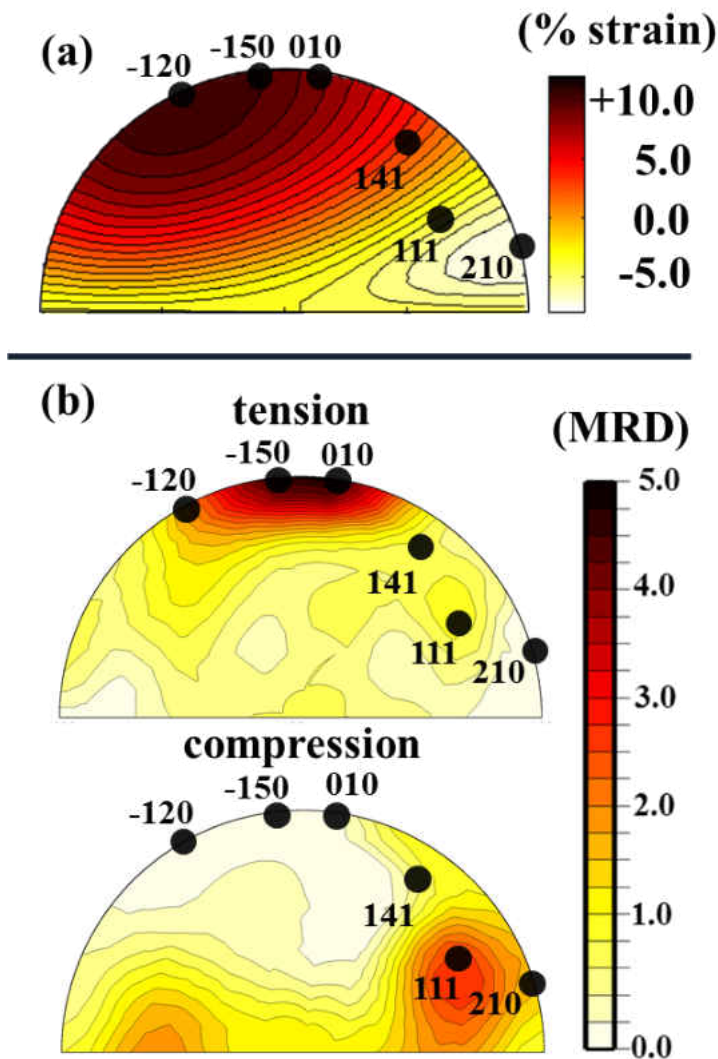
Figure 5.12: Association between (a) Bain strains calculated from crystallographic theory using lattice parameter obtained from Rietveld refinement and (b) tensile and compressive preferred B19′ variant selection obtained from experiment shown by recourse to inverse pole figures corresponding to lattice planes perpendicular to the loading direction. For clarity in presentation, the scales chosen are unique to this figure.
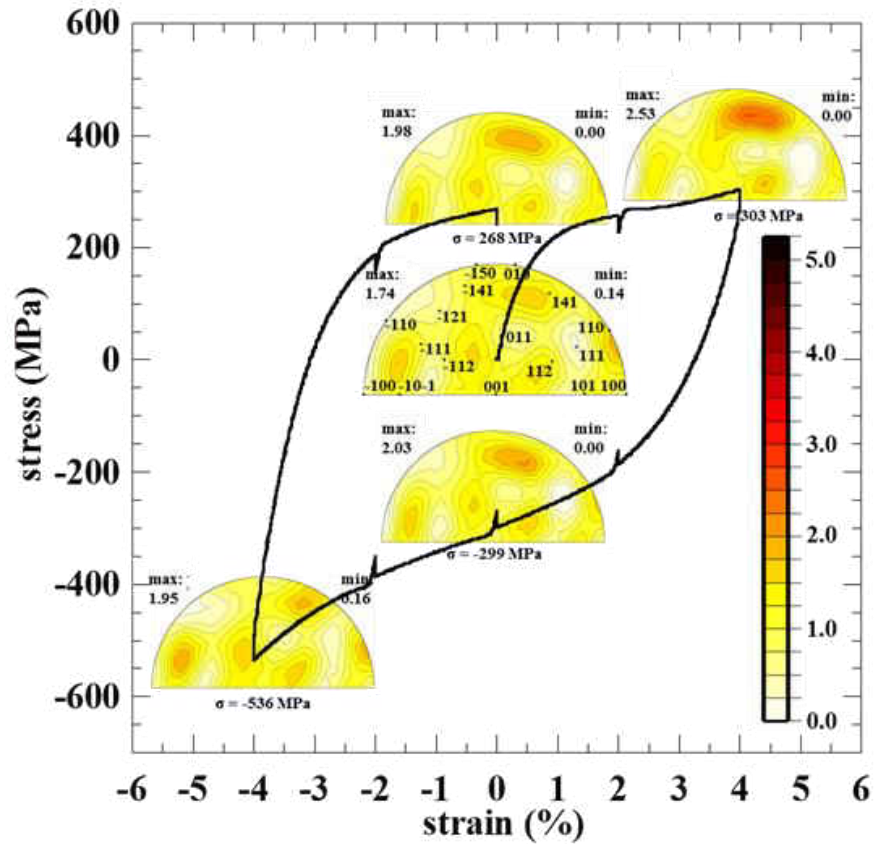
Figure 5.13: Inverse pole figures (IPFs) corresponding to diffracting planes $\Phi = 46.3°$ relative to the loading direction during the first cycle of isothermal tensile followed by compressive strain-controlled reverse loading of B19′ martensitic NiTi at room temperature. Note, the IPFs presented here were generated from Rietveld refinements of diffraction spectra captured by detector Bank 3 (as illustrated in Figure 5.1). For clarity in presentation, the scale chosen is unique to this figure.
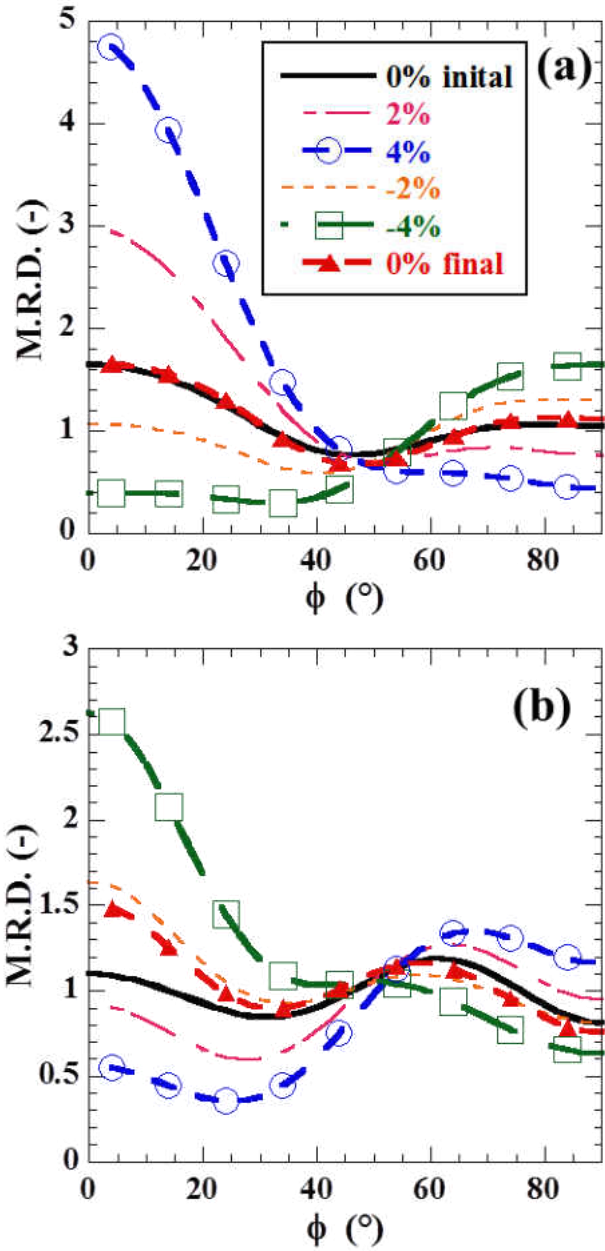
Figure 5.14: Axial distribution plot corresponding to the first cycle of tension followed by compression isothermal reverse loading of B19′ martensitic NiTi at room temperature: (a) 010 and (b) 111.

CHAPTER SIX: TEXTURE EVOLUTION DURING ISOTHERMAL, ISOSTRAIN AND ISOBARIC LOADING OF POLYCRYSTALLINE NITI

In this chapter, in situ neutron diffraction was used to provide insight into martensite variant structures during isothermal, isobaric, and isostrain loading in shape memory NiTi. Results show variant structures were equivalent for the corresponding strain and more importantly, the reversibility and equivalency was immediately evident in a variant structure that was first formed isobarically but then reoriented to a near random self-accommodated structure by isothermal deformation. Variant structures formed isothermally were not significantly affected by a subsequent thermal cycle under constant strain. In all loading cases, the resulting variant structure correlated with strain and did not correlate with stress.

6.1 Introduction

Shape memory alloys (SMAs) have the ability to recovery their pre-deformed shape against external loads thus enabling work output in actuator applications. However, the full scale commercialization of SMA enabled actuator technologies has been limited in the absence of a comprehensive understanding of these alloys under general loading conditions (combined with other reasons, e.g., limited understanding of the evolutionary response) and associated deformation processes. With recoverable strains exceeding 4%, near equiatomic NiTi has been the most extensively used system for SMA actuator technologies thus far. In shape memory NiTi the recovery process occurs by way of a reversible thermoelastic martensitic phase transformation from a monoclinic (B19') martensite phase to a cubic (B2) austenite phase [4, 5]. Previously, *in situ* neutron diffraction has been used extensively to correlate macroscopic behavior to associated deformation mechanism in polycrystalline shape memory NiTi [7, 16, 36,

37, 47, 63, 66]. A majority of these experiments have solely examined either isothermal [7, 16, 36, 47, 66] (deformation at constant temperature) or isobaric [7, 16, 37, 63] (thermal cycling to temperatures above and below the phase transformation temperatures under constant stress) loading while only a few build connections [7, 16] between the two loading paths. Furthermore, experiments examining isostrain (thermal cycling to temperatures above and below the phase transformation temperatures under constant strain) loading have been limited [40, 48] and could further our understanding of the use of SMAs in novel applications, e.g., reinforced composites, couplings, etc.

The overall objective of this work is thus to provide micromechanical and microstructural insight into the isothermal, isobaric, and isostrain loading of SMA with emphasis on providing connections between these loading paths. This is accomplished by recourse to subjecting a polycrystalline shape memory NiTi SMA to *in situ* neutron wherein information representative of the bulk including evolving texture, phase fractions, and lattice strains is determined in carefully selected experiments involving combined loading sequences. The results are analyzed and presented in the context of the reversible thermoelastic nature of the martensitic transformation in SMAs and its implications on the stability of these alloys.

6.2 Methods

The material used was the same binary NiTi alloy used in Chapter 5 and additional details can be found in Section 5.2.1 in Chapter 5. The following experiments were performed *in situ* in "time-of-flight" mode using SMARTS at LANL. Additional details regarding the experimental setups at SMARTS and VULCAN can be found in Section 2.2.1 in Chapter 2.

Two stress-free thermal cycles (i.e., isobaric loading at 0 MPa) between room temperature (RT) and 200 °C were performed prior to every experiment after the specimen was installed in the load frame. This was done to relieve any residual stresses produced by processing, machining or installation of the sample and to establish initially, a self-accommodated B19′. All isothermal loading was performed in strain control (at a strain rate of 10^{-4}) at SMARTS and displacement control (manually, while strain was monitored by extensometry) at VULCAN. It is implicit that prior to an isostrain or isobaric loading cycle the specimen was isothermally loaded (below the M_f temperature) to that strain or stress, respectively. A total of three experiments were performed as follows. Two experiments performed at SMARTS include: one compression-tension (i.e., compression followed by tension) isothermal loading cycle to ±4% strain, then back to 0% strain at RT; and one isostrain loading cycle at 2% tensile strain between 40 °C and 165 °C. Isobaric and isothermal loading was performed at VULCAN in one experiment in the following order: one isobaric loading cycle at 100 MPa tension between RT and 165 °C; compressive isothermal loading to -1.0% strain; two isobaric loading cycles at 0 MPa between RT and 165 °C; and isothermal loading to 3.9% tension at RT. Neutron diffraction spectra were acquired at select points throughout all experiments as shown in context of the results. To insure adequate statistics for analysis a hold time of 30 min and 15 min at SMARTS and VULCAN, respectively, was used to acquire each spectrum. Details regarding Rietveld refinement and IPFs can be found in Section 2.2.3 in Chapter 2.

6.3 Results and Discussion

A random self-accommodated martensite variant orientation was established as indicated by a maximum intensity of 1.78 (±0.2 of previous work with this particular alloy [36]) in the IPF at the initial condition (0 MPa stress and 0% strain) in Figure 6.1. Figure 6.1 shows the macroscopic response of NiTi specimen under isothermal compressive loading to -4% strain, followed by tensile loading to 4% strain, then compressive loading to 0% strain (from extensometry, as shown by the solid black line). The first segment (0 to -4% strain) of isothermal compressive loading has been well studied and partitioned into multiple loading regimes with corresponding deformation mechanisms by recourse to correlation of IPFs to macroscopic deformation [7, 37, 66], e.g., in this case elastic deformation (up to 200 MPa) and detwinning and variant conversion (occurring at stresses as low as 50 MPa). At a maximum compressive strain of -4% the specimen was within the end of the region in which detwinning and variant conversion was the dominant deformation mechanism although others, e.g., deformation twinning, slip and dislocation based plasticity, may be active to a limited degree. Direct evidence of preferred selection of martensite variants by variant reorientation and detwinning was observed as an increase in intensity at the 111 pole in the corresponding IPF. A maximum intensity (near the 111 pole) of 3.00 was observed and was comparable to a maximum intensity (near the same location) of 2.96 as observed in Ref. [3] at -3.7% strain. These variants preferentially selected in compression reoriented to a near random self-accommodated orientation when the deformation was reversed (from -4% to 0% strain) and the macroscopic strain approaches zero, thus indicating the reversibility of variant reorientation and detwinning processes (observed macroscopically by the onset and continuation of the detwinning and variant

reorientation stress plateau). Following this first load reversal at 0% strain residual texture was observed as an increase in intensity at the 010 and 111 poles and an increase in maximum intensity (near the 010 pole) from 1.78 to 1.93 when compared to the initial IPF.

When deformation was continued in tension to 4% strain preferred selection of martensite variants was observed as an increase in intensity at the -150 pole in the corresponding IPF. A maximum intensity (near the -150 pole) of 5.18 was observed and was comparable to a maximum intensity (near the same location) of 6.49 as observed in Ref. [3] in which the specimen was loaded directly from the initial to 5.3% strain. These variants preferentially selected in tension reoriented to a near random self-accommodated orientation when the deformation was reversed again and the macroscopic strain approaches zero, further demonstrating the reversibility of variant reorientation and detwinning processes. The amount of residual texture had increased at the 010 pole when compared to the IPF at 0% strain following the first load reversal as also indicated by an increase maximum intensity (near the 010 pole) from 1.76 to 2.30 when compared to the initial IPF. Overall, a similar texture (with residual texture) was observed at zero strain despite a significant difference in stress following the initial, 1st and 2nd deformation reversal (0MPa, 330 MPa and -234 MPa, respectively). In all cases of such isothermal loading (i.e., compression followed by tension and solely [36] compression or tension), the resulting variant structure correlated with the macroscopic uniaxial strain and did not correlate with the compressive or tensile state of stress. The residual texture observed at zero strain may be the result of some degree of compression and tension preferred variants pinned by dislocations which accumulated during the isothermal reverse loading process, slip and/or the early onset of deformation twinning. The accumulation of dislocations at both junction plane

areas and within the martensite twins have been observed by transmission electron microscopy in similar reverse loading experiments [55]. By recourse to IPFs, indirect evidence of slip has previously been captured as the slight rotation of the -150 to 010 poles during tension deformation [7]. Recent progress has been made towards quantifying the contributions of each these deformation mechanisms (i.e., elastic, detwinning/variant reorientation, deformation twinning and slip) to the overall strain using a micromechanical model based diffraction data analysis framework which shows all such mechanisms to be active to a limited degree within the limits studied here [8, 66].

Figure 6.2 shows the macroscopic response for one thermal cycle to temperatures above and below the phase transformation under a constant tensile strain (isostrain loading) of 2%. The initial IPF (not shown) at 0 MPa stress and 0% strain at RT with a maximum intensity of 1.91 was comparable to the initial IPF of Figure 6.1, thus indicating a self-accommodated starting B19′. The specimen was isothermal loaded in strain control to 2% strain (Points A to B) and variants preferentially selected in tension were consistent with results presented in Figure 6.1, as shown by the IPF corresponding to Point B at a stress of 262 MPa. This strain was held constant in strain control, then the specimen was thermally cycled from 40 °C to 165 °C (Points B to C) and blocking stress (maximum of 450 MPa) was observed as result of the phase transformation to B2 at Point C. Note, no significant texture change was observed in the B2 phase. When the specimen was cooled back to 40 °C (Point C to D) through the phase transformation the stress relaxed to 6 MPa. The IPF corresponding to Point D showed a similar variant structure to that of Point B with a small decrease in the maximum intensity from 3.57 to 3.20 near the -150 pole. Deformation processes associated with shape setting [40] (e.g., plastic deformation and recovery

processes) may be active to a limited degree and have contributed to the relaxation of stress and the slight decrease in texture. Overall, the macroscopic stress from the isothermal strain relaxed to near zero with no concomitant change in the variant structure following the first thermal cycle, thus representing the correlation between the resulting variant structure and the macroscopic strain during isostrain loading.

Figure 6.3 shows the IPFs corresponding to isothermal (indicated by solid arrows) and isobaric (indicated by dashed arrows) loading in the same experiment. The initial IPF (Point I) at 0 MPa stress and 0% strain at RT with a maximum intensity of 1.87 was comparable to the initial IPF of Figure 6.1. This indicates a self-accommodated starting B19′ and establishes a basis for comparisons between the IPFs generated from experiments at SMARTS (i.e., Figs. 1 and 2) and VULCAN (i.e., Fig. 3). The corresponding macroscopic position is given above each IPF in Fig. 3, and the macroscopic isothermal and isobaric paths are shown in Figs. 1 and 4, respectively. Note, the strain shown in Fig. 1 and Fig. 4 is shared. Initial isothermal loading at RT from 0 to 100 MPa (Point I to II) was dominated by elastic deformation mechanisms with limited detwinning and/or variant reorientation, as indicated by no significant change in the maximum intensity observed in the IPFs and was consistent with Refs. [2,5,9]. The specimen was held constant at a tensile stress of 100 MPa and thermally cycled between RT and 165 °C (i.e., isobaric loading from Point II to III) resulting in a tensile strain of 3.9 % (often referred to as transformation strain) at Point III, as shown by the dashed line in Fig. 4. Variants were preferentially selected as indicated by a maximum intensity of 5.83 near the -150 pole which compared well to variants preferentially selected in tension at the equivalent strain generated by isothermal deformation in Fig. 1 and Ref. [2].

From 3.9% strain (Point III) the specimen was isothermal deformed in compression at RT to -1.0% strain (Point VI), as shown by the dashed line in Fig. 1. Variant reorientation and detwinning was observed macroscopically in Fig. 1 as the onset (Point IV) and continuation of the stress plateau (Points IV through VI). The corresponding IPFs show that variants preferentially selected by tensile isobaric loading reoriented to a near random self-accommodated orientation with some residual texture during isothermal loading from Points III to VI. This behavior was consistent with deformation following the 2nd load reversal (4% to 0% strain) in Fig. 1. From Point VI the specimen was unloaded to 0 MPa resulting in -0.6% and maximum intensity of 2.65 in the corresponding IPF at Point VII. Then, two isobaric cycles at 0 MPa were performed between 30 °C and 165 °C which resulted in variant structure near random self-accommodated orientation with some residual texture at 0.5% strain, as shown macroscopically by the solid line in Fig.4. At Point VIII the specimen both macroscopically and microstructurally was near the initial state (Point I) with the exception of residual texture. The specimen was then isothermally loaded in tension to 3.9% at RT (Points VIII to IX, shown macroscopically in Fig. 1) and variants were preferentially selected as indicated by a maximum intensity of 5.32 near the -150 pole. This selection of variants was equivalent (as correlated by strain) to variant selection observed during isobaric loading (Points II to III in Fig. 3) and isothermal loading in Fig. 1 and Ref. [2].

6.4 Conclusions

Overall, the variant structures were equivalent for the corresponding strain and more importantly, the reversibility and equivalency was immediately evident in a variant structure that was first formed isobarically but then reoriented to a near random self-accommodated structure

by isothermal deformation. In all cases of such loading (tensile or compressive isothermal, isobaric or isostrain) the resulting B19′ variant structure correlated with the macroscopic uniaxial strain and did not correlate with the compressive or tensile state of stress. Based on the ability to select a particular variant structure for a given strain after a loading history (e. g., the 2nd load reversal following the 1st load reversal in Fig. 1 or Points VIII to IX following Points I through VIII in Fig. 3) it can be speculated that the results demonstrated in this letter could be obtained by following any order of loading path over multiple cycles with the exception of residual texture (the formation of which will likely saturate with cycling [10]). The foundation for this observed behavior lays in the fundamental reversibility of detwinning and variant reorientation processes in B19′ by both isothermal deformation and the phase transformation between B19′ and B2. These reversible deformation mechanisms dominant over the irreversible deformation mechanisms (within the limits investigated), the effects of which are minimized by the accommodative nature of B19′ as observed as the formation of residual texture.
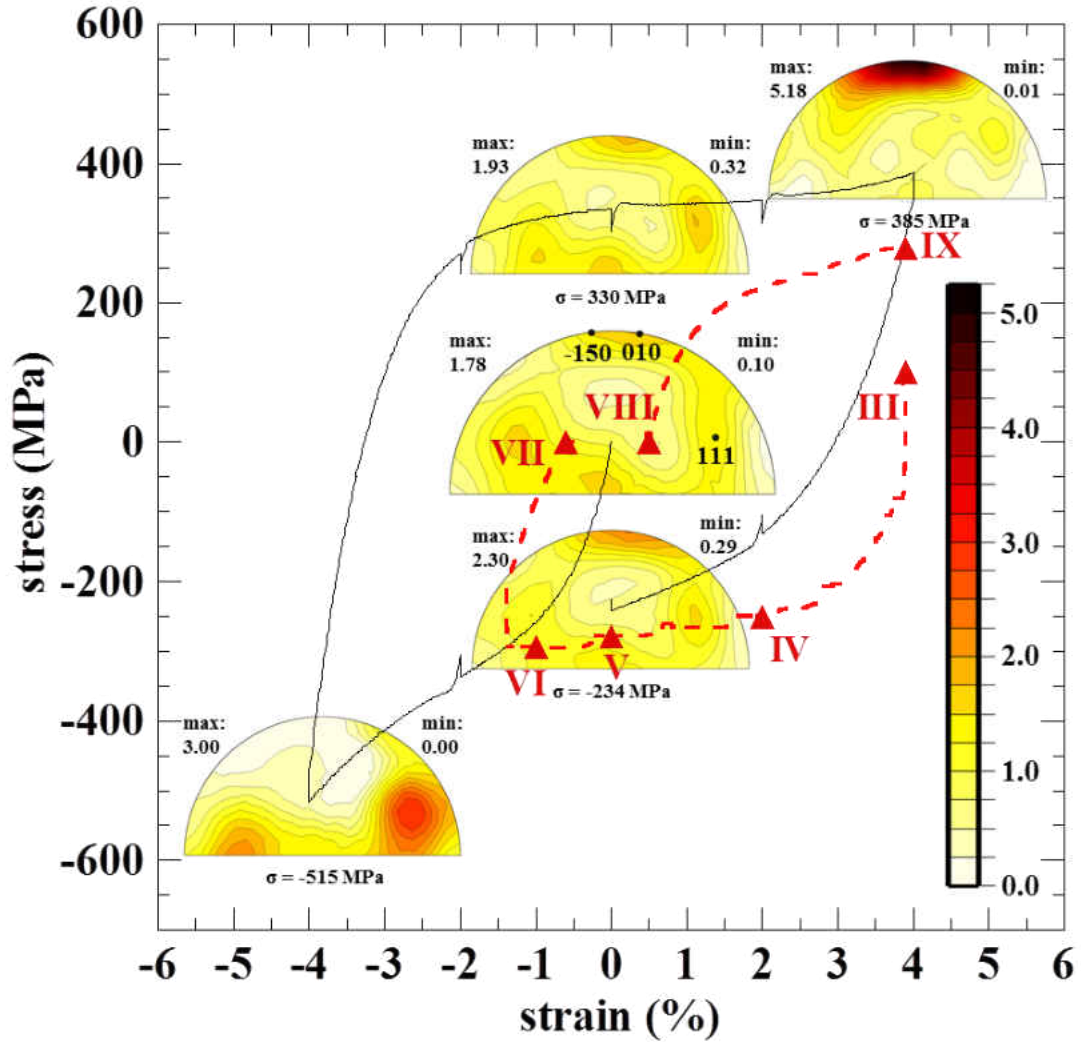
Figure 6.1: Inverse pole figures (IPFs) for the loading direction and corresponding macroscopic response of B19′ martensitic NiTi under isothermal compressive followed by tensile, then compressive reverse loading (as shown by the solid line). Also shown is the macroscopic isothermal path (as shown by the dashed line) corresponding to Points III-IX (as indicated by ▲) of FIG. 3. For clarity in presentation, the scale chosen is unique to this figure.
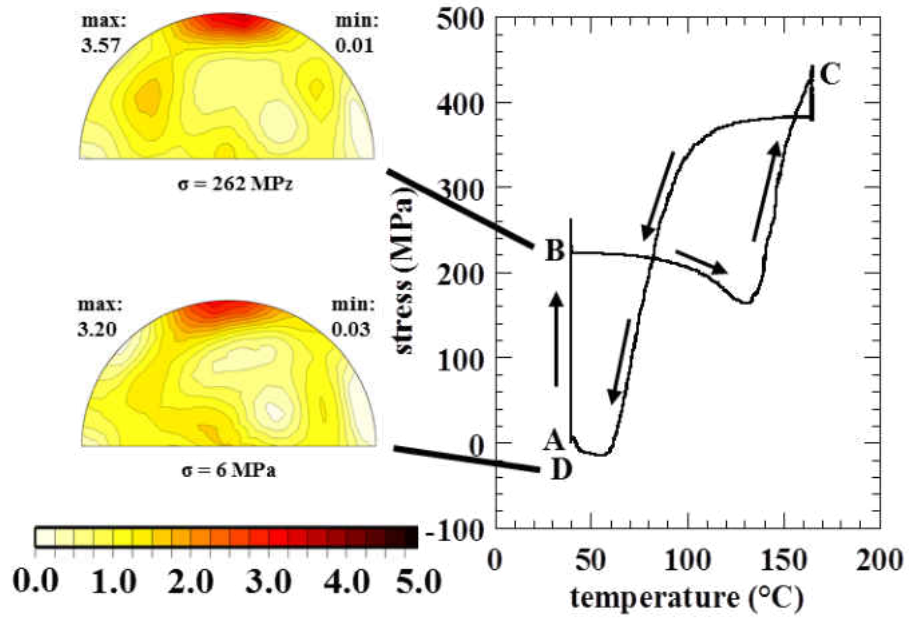
Figure 6.2: Inverse pole figures (IPFs) for before (Point B) and after (Point D) one thermal cycle to temperatures above and below the phase transformation under a constant strain of 2% and corresponding macroscopic response. For clarity in presentation, the scale chosen is unique to this figure.
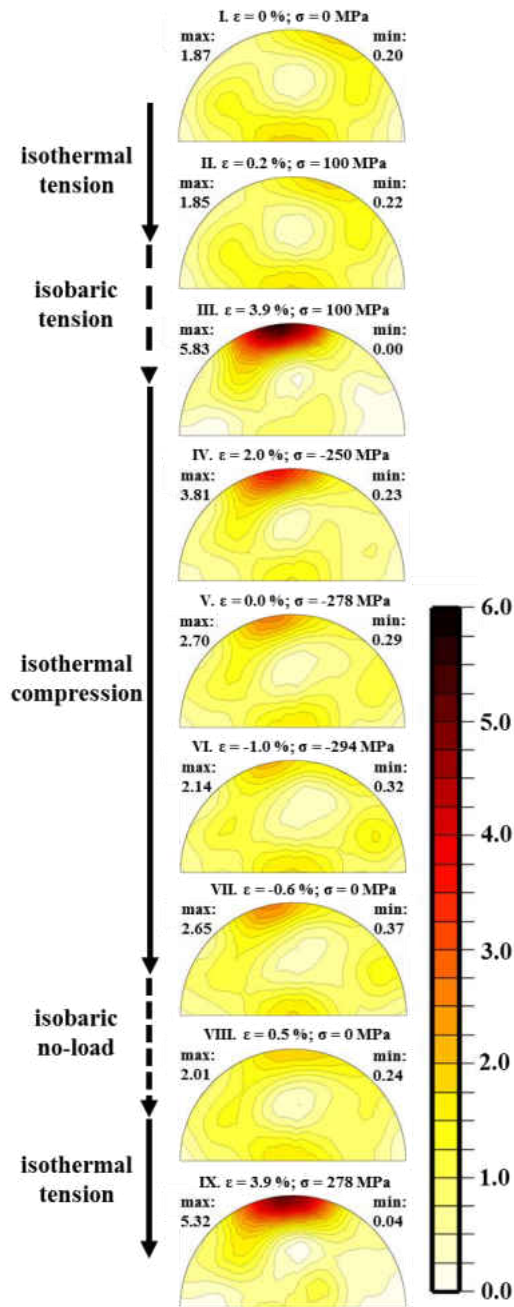
Figure 6.3: Inverse pole figures (IPFs) corresponding to mixed isothermal (indicated by solid arrows) and isobaric (indicated by dashed arrows) loading in the same experiment. During isobaric loading the sample was thermally cycled to temperatures above and below the room temperature, once from Points II to III and twice from Points VII to VIII. The corresponding macroscopic position is given above each IPF. For clarity in presentation, the scale chosen is unique to this figure.
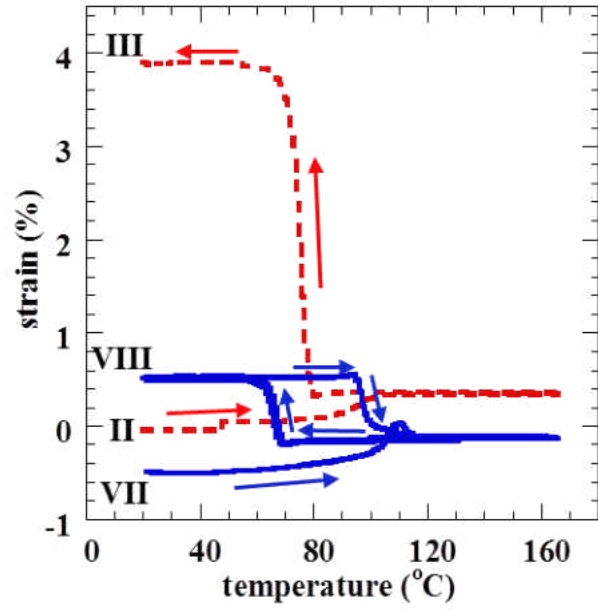
Figure 6.4: Macroscopic isobaric path corresponding to Points II-III (as shown by the dashed line) and Points VII-VIII (as shown by the solid line) from FIG. 3.

CHAPTER SEVEN: INVESTIGATION OF THE R-PHASE DURING STRESS- AND TEMPERATURE-INDUCED PHASE TRANSFORMATIONS

Superelastic polycrystalline NiTi (50.8 at.% Ni) was subjected to in situ neutron diffraction at the VULCAN diffractometer at Oak Ridge National Laboratory and the Spectrometer for MAterials Research at Temperature and Stress (SMARTS) at Los Alamos National Laboratory wherein the evolving texture, phase fractions and lattice strains were tracked. A fully-reversible, (i) thermally-induced phase transformation between the cubic B2 and trigonal P3 (R) phases between room temperature and 45°C in the unloaded condition and (ii) stress-induced phase transformation between the R and monoclinic B19' phases during isothermal tensile loading (up to 500 MPa) at room temperature were investigated. The experimentally measured strains correlated well with the single crystal Bain strains calculated from crystallographic theory for this alloy and allowed for the identification of specific R-phase variants. Experimental observations of reorientation/detwinning in the R-phase agreed well with predictions of variant conversion in respective R-phase variants (up to 200 MPa).

7.1 Introduction

Shape memory alloys (SMA) have the ability to recover large deformations against externally applied load by way of both a stress induce (superelasticity) or thermally induced (shape memory effect) phase transformation. The solid-state phase transformation in NiTi-based SMA can occur by way of transformation paths between cubic B2, trigonal P3 and/or monoclinic B19', phases commonly referred to as austenite, R-phase and martensite, respectively. With recoverable strains reaching up to 8%, the B2 to B19 is the more commonly investigated

transformation path, with the R-phase often being overlooked. However, the B2 to R-phase transformation has been shown to produce transformation strains on the order of 1% with excellent stability and reduced hysteresis [5, 53]. With the ability to provide stable actuation, the B2 to R-phase transformation, has promoted investigations seeking to develop R-phase actuators, e.g. in Ref. [3, 67]. Superelastic NiTi has been commonly used in biomedical applications which include self-expanding stents [68], self-tightening orthodontic wires and flexible eye glass frames, among others. In many of these applications, in absence of a full understanding, the presence of the R-phase has often been regarded as detrimental to the performance and fatigue life. Thus, the current investigation seeks to improve the fundamental understanding of R-phase with the goal of facilitating the development of R-phase actuators and improving the stability, fatigue life and durability of superelastic systems.

In previous work, Ref. [69] showed that four possible R-phase variants form during transformation from B2 as governed by the rhombohedral distortion angle α and that α is a function of temperature. Also, when transforming to R-phase under no-stress these variant produce zero macroscopic strain as the result of a self-accommodation and when stress is applied the most favorable variants form at the expense of others indicating deformation by detwinning. Since the R-phase, can detwin, reorient and undergo a thermally or stress-induced transformation it is difficult from macroscopic measurements to decouple elastic and inelastic contributions (from respective phases) to the overall deformation. Multiple investigations seeking to correlate the microstructural and macroscopic behavior R-phase have been performed by recourse to *in situ* neutron diffraction [14, 15, 70, 71]. Wherein, *in situ* neutron diffraction allows for lattice

strain, texture and phase fraction information, representative of the bulk, to be tracked during heating and loading of NiTi-based alloys.

Splitting of the $(110)_A$ austenite diffraction peak into $(1-10)_R$ and $(110)_R$ R-phase peaks was observed in neutron diffraction spectra acquired (in Refs. [15, 71]) during cooling through the phase transformation. In these studies, the dependence of α on temperature was also demonstrated experimentally as observed by the distance between R-phase peaks increasing with decreasing temperature. Ref. [14] showed reorientation and detwinning in R-phase as indicated by changes in R-phase peak intensity during tensile and compressive loading. Ref. [70] demonstrated methods for performing Rietveld refinement on R-phase in $Ni_{46.8}Ti_{50}Fe_{3.2}$ from which it was determined that the trigonal R-phase belongs to the $P3$ or $P\bar{3}$ space group. Plane-specific elastic moduli of R-phase were also determined by recourse to neutron diffraction at cryogenic temperatures in Ref. [15].

Most of these previous investigations were performed below the room temperature. This work seeks to investigate a fully-reversible, (i) thermally-induced phase transformation between the cubic B2 and trigonal P3 (R) phases between room temperature and 45°C in the unloaded condition and (ii) stress-induced phase transformation between the R and monoclinic B19' phases during isothermal tensile loading (up to 500 MPa) at room temperature, by recourse to *in situ* neutron diffraction.

7.2 Experimental Procedures

A commercially available, biomedical grade polycrystalline NiTi (nominal composition 50.8 at.% Ni) produced by Fort Wayne Metals (Fort Wayne, IN) was used for all experiments. Solid cylindrical dog-bone specimens (with a gauge diameter of 5.08 and length of 17.8 mm)

with threaded ends were machined from the as-received material and were heat treated at 350°C for 1 hour (in air furnace) then ice-quenched. The following experiments were performed *in situ* in "time-of-flight" mode using SMARTS at LANL. Additional details regarding the experimental setups at SMARTS and VULCAN can be found in Section 2.2.1 in Chapter 2.

One specimen (designated *S1*) was subjected to heating from 22 (room temperature) to 45°C under no-load. Neutron spectra were acquired at 22, 26, 30, 35 and 45°C. Then, *S1* was heated to 45°C and the specimen was isothermally loaded/unloaded to 7.2% tensile strain (565 MPa) in displacement control (at a rate of 0.004 mm/s). A second specimen (designated *S2*) was subjected five isothermal tensile loading/unloading cycles in displacement control (at a rate of 0.004 mm/s) to approx. 500 MPa stress at room temperature. During loading of specimens *S1* and *S2* Neutron diffraction were acquired at selected points. To insure adequate statistics for analysis a hold time of 15 min was used to acquire each spectrum. A third specimen (designated *S3*) was subjected to two isothermal tension-compression cycles between -0.325% and 0.675% strain at room temperature. Neutron data was acquired by continuous scanning. To insure adequate statistics a strain rate of 0.2 %/hour was maintained. Each reported neutron spectra represents statistics averaged over 15 min or 0.05 % strain. Rievteld refinement was implemented by GSAS [21] using methodology presented in Ref. [70] for analyzing R-phase.

7.3 Results and Discussion

7.3.1 Identification of R-phase Variants

Figure 7.1 shows normalized spectra acquired from lattice plane reflections with plane normals parallel to the loading direction corresponding to heating of specimen *S1* from room temperature to 45°C. Initially at room temperature, R-phase peaks were observed as indicated by

the black vertical dashed lines. To facilitate the following calculations these peaks were indexed on both the trigonal R-phase and parent B2 lattice, as labeled in black and blue, respectively. Upon heating to 45°C, R-phase transformed to B2 austenite. The B2 peak locations are indicated by red vertical dashed lines and the corresponding indices are labeled in red. The B2 phase to R-phase transformation occurs by way elongating the B2 cube along one of its (111) axis by a rhombohedral distortion angle α (as was previously done in Ref. [69]). Thus, a total of 4 variants can be formed during this transformation. The transformation matrix between the B2 and R-phase lattice is given by:

$$
B = \begin{bmatrix} \sqrt{2}\sin(\alpha/2) & 0 & 0 \\ 0 & \sqrt{2}\sin(\alpha/2) & 0 \\ 0 & 0 & \sqrt{3-4\sin^2(\alpha/2)} \end{bmatrix} \tag{7.1}
$$

Using the measured $(100)_R$ and $(110)_R$ peaks, α was determined to be 89.45° at room temperature. Note, α is dependent on temperature and α=90° above the A_f temperature. Using α=89.45°, the transformation strains between B2 and R-phase were calculated using the relationship given by Equation (7.1) for all 4 variants. The Matlab script used to perform this calculation can be found in Appendix A-2. These calculations are summarized in Table 1 in the along the $<111>_{B2}$, $<110>_{B2}$ and $<100>_{B2}$ directions. The following strains (as labeled in Figure 1) were measured between B2 and R-phase peaks: $\varepsilon_{111}^A = 0.86\%$, $\varepsilon_{111}^B = -0.40\%$, $\varepsilon_{110}^A = 0.37\%$ and $\varepsilon_{110}^B = -0.42\%$. Upon comparison to Table 7.1 it becomes apparent that ε_{111}^A corresponds to

variant A and ε_{111}^{B} corresponds to variant B, C or D. Similarly, ε_{110}^{A} corresponds to variant A or B and ε_{110}^{B} corresponds to variant C or D.

Figure 7.2a shows three distinct regions of different moduli (distinguished by red dashed vertical lines, labeled I, II and III) and strains, in which neutron data is indicated by (·) points 1-5. Figure 7.2b shows normalized spectra corresponding to reflections from lattice planes with plane normals parallel to the loading direction for points 1-3. In Figure 7.2b, R-phase variants A, B, C and D are indicated by red arrows. Upon loading from ε=0.0% (point 1) to ε=1.0% (point 3) variant B, C or D reorient and detwin to form variant A (as indicated by change in peak intensity). Conversion strains between the R-phase variants are calculated and summarized in Table 1. Conversion from variants B, C, D to A will yield up to 1.2759% strain in the $\langle 111 \rangle_{B2}$. This was consistent with the 1.0% macroscopic strain measured by extensometry. Note, that a similar reorientation occurred w.r.t. the $\langle 110 \rangle_{B2}$ with respective corresponding variants (not shown here). Variant reorientation and detwinning of R-phase was determined to be the dominate deformation mechanism in Region I and continued into Region II. Elastic deformation of R-phase predominantly contributed to the overall deformation in Region II. A modulus of elasticity of around 30 GPa was measured in Region II. This modulus was lower than values previously reported for the R-phase (i.e., 70 GPa in Ref. [72]), suggesting detwinning/variant reorientation in the R-phase and early onset of a R-phase to B19' phase transformation.

From ε=1.5% (point 3) to ε=2.5% (point 5) the R-phase to B19' phase transformation begins as observed by the stress plateau at approx. 300 MPa. The macroscopic stress plateau was consistent with the observation of B19' martensite peaks in the normalized spectra (not shown here), thus indicating the primary deformation mechanism in Region III was the phase

transformation from R-phase to B19'. Note, that some B2 austenite was present in the system in the unloaded state and transformed to the R-phase or B19' phase upon loading. However, the phase volume fraction under no-load at room temperature was shown by recourse to Rietveld refinement to be less than 20% B2 austenite.

7.3.2 Strain-controlled Reverse Loading of R-phase

To further demonstrate reorientation and detwinning of R-phase variants in this system, two isothermal tension-compression cycles between -0.325% and 0.675% strain at room temperature. The strain limits were chosen such that the variant and reorientation of R-phase would be the domininant mechanism during loading (as defined by region I in Figure 7.2a). Figure 7.3 shows the macroscopic stress-strain response corresponding during the second cycle of strain-controlled isothermal reverse loading cycles between -0.325 and 0.675% strain of specimen *S3* at room temperature. The observed stress platues both loading and unloading indicate that reorientation and detwinning processes are the dominant deformation mechansims. Additionally, the observation that two cycles overlap inidcates that variant reorientation and detwinning in R-phase is isothermally reversible.

To investigate this further, Figure 7.4a shows normalized intensity of $(111)_R$ and $(11\text{-}1)_R$ peaks (corresponding to R-phase variants A and B, C or D, respectively) acquired from planes perpendicular to loading axis corresponding to the macroscopic response shown in Figure 7.3. Note, that peak intensities are normalized their respective intensities at zero strain. Upon loading from zero to 0.675% strain, $(111)_R$ and $(11\text{-}1)_R$ peak intensities increased and decreased, respectively, indicating the preferred tensile selection of variant A at the expense of variants B, C or D. As loading was reversed from 0.675% to -0.325% strain, $(11\text{-}1)_R$ and $(111)_R$ peak

intensities increased and decreased, respectively, indicating the preferred compression selection of variant B, C or D at the expense of variants A. Table 7.1 shows that variant A and variants B, C or D produce tensile and compressive Bain strains, respectively, w.r.t. the $<111>_{B2}$ direction. Therefore the result that variant A and variants B, C or D preferentially select under tensile and compressive loading, respectively (in the polycrystalline aggregate), is consistent with the notion that when stress is applied the most favorable variants form at the expense of others. This result has previously been shown in R-phase in Ref. [69] and for B19′ in Chapter 5 of this dissertation.

Figure 7.4b shows normalized intensity of $(111)_R$ and $(11\text{-}1)_R$ peaks (corresponding to R-phase variants A and B, C or D, respectively) acquired from planes parallel to loading axis corresponding to the macroscopic response shown in Figure 7.3. Upon tensile loading from zero to 0.675% strain, $(111)_R$ and $(11\text{-}1)_R$ peak intensities decreased and increased, respectively, indicating the preferred selection of variant B, C or D at the expense of variants A under a compressive stress state governed by Poisson contraction. Upon compressive loading from zero to -0.325% strain, $(11\text{-}1)_R$ and $(111)_R$ peak intensities decreased and increased, respectively, indicating the preferred selection of variant A at the expense of variants B, C or D under a tensile stress state governed by Poisson expansion.

During the entire loading sequence the intensities of both peaks track nearly the same path as observed during loading, thus indicating the reversibility of variant reorientation and detwinning processes. At zero strain, both peak intensities returned to their respective initial values (within error), despite significant differences in stress observed macroscopically between loading and unloading stress plateaus (as shown in Figure 7.3).This indicates that variant reorientation and detwinning in R-phase correlates well with macroscopic strain and does not

with stress. This result was also observed during variant reorientation and detwinning of B19′ in shape memory NiTi in Chapters 5 and 6 of this dissertation.

7.3.3 Stress-induced Transformation from R-phase to B19′

The stress-induced transformation from R-phase to B19′ was also investigated here. Figure 5 shows selected normalized diffraction spectra acquired from lattice planes perpendicular to the loading direction that correspond to the 5th cycle of isothermal loading and unloading (to 500 MPa) of specimen *S2* at room temperature. Prior to the cycle (at -44MPa) the specimen was shown to be primarily R-phase (with up to 20% vol. fraction of B2) by comparison to Figure 7.1 and Rietveld refinement. When loaded to a maximum stress of 500 MPa all available R-phase transformed to the B19' phase (within detectable limits), as indicated by the solid pink line in Figure 7.5. Upon unloading and returning to the initial state, a similar spectrum indicating mostly R-phase was observed (as indicated by the solid black and red lines in Figure 7.5). This result established the reversibility of the stress phase transformation between R-phase to B19' at room temperature under the experimental conditions investigated.

Previously used methodology (see Refs. [4, 5, 44], among others and Section 5.4 in Chapter 5) was used to calculate the B2 to B19′ transformation strains for the 12 Correspondent Variant Pairs (CVPs) of B2 to B19′ transformation in the B2 basis along the $<111>_{B2}$, $<110>_{B2}$ and $<100>_{B2}$ directions (see Table 7.2). Note, the B2 and B19′ lattice parameters used in these calculations were acquired from Rietveld refinements performed in this study. The difference of B2 to R-phase (Table 7.1) and B2 to B19' transformation strains were taken to yield the R-phase to B19' transformation strains. The results are shown in Table 7.2, for transformation from R-phase variant A and variant B to the 12 CVPs of B19′. The Matlab script used to perform this

calculation can be found in Appendix A-3. The calculations show that theoretical transformations paths exist from R-phase to B19′ that can yield more strain then the largest strain obtainable between B2 and B19′, as highlighted by yellow.

To directly compare the R-phase to B19′ with the B2 to B19′ stress-induced transformation specimen *S1* was heated to 45°C then isothermally loaded and unloaded to 565 MPa. Figure 7.6a shows the macroscopic stress-strain response during isothermal loading and unloading up to 565 MPa of specimen *S1* at 45°C. Figure 6b shows the corresponding normalized spectra acquired from lattice plane reflections with plane normals parallel to the loading direction. During loading from 0 to 169 MPa (points 1 to 2), elastic deformation of B2 is observed as linear elastic response in Figure 6a and as indicated by an equivalent $(111)_A$ peak shift (with limited change of peak intensity) in Figure 6b. When loading was continued from 169 to 326 MPa (point 2 to 3) stress-induced transformation from B2 to R-phase was observed as indicated by a large peak shift in Figure 7.6b. Note, that the $(111)_R$ peak (corresponding to R-phase variant A) preferentially forms from the $(111)_A$ peak as governed by the applied tensile state of stress. As loading was continued from 326 to 395 MPa, elastic deformation of R-phase was observed as indicated by the shifting (with limited change of peak intensity) of the $(111)_R$ peak. When loaded to a maximum stress of 565 MPa all available R-phase transformed to the B19′ phase (within detectable limits), as indicated by the solid red line in Figure 7.6b.

The aforementioned transformation from B2 to B19′ with an intermediate R-phase step was shown on the reverse transformation, when the specimen was unloaded to zero (from points 6 to 9). The isothermal stress-strain response demonstrating the direct stress-induced phase transformation from R-phase to B2 at room temperature is also shown in Figure 6a for

comparison. The stress-induced phase transformation yielded only slightly more (within error) recoverable strain at 45°C (from B2 to R-phase to B19') than at room temperature (from R-phase to B19'). This result was consistent with the theoretically calculated single-crystal strains presented in Table 7.2.

7.4 Conclusions

Biomedical grade superelastic NiTi was investigated by recourse to *in situ* neutron diffraction performed during various heating and loading sequences. Experimentally measured strains correlated well with the single crystal Bain strains calculated from crystallographic theory for this alloy and allowed for the identification of specific R-phase variants. Experimental observations of reorientation and detwinning in the R-phase agreed well with predictions of variant conversion in respective R-phase variants (up to 200 MPa). A fully-reversible stress-induced phase transformation between the R and monoclinic B19' phases during isothermal tensile loading (up to 500 MPa) at room temperature was observed and investigated. The stress-induced phase transformation between R and monoclinic B19' was compared to the stress-induced phase transformation B2 and monoclinic B19' both experimentally and by recourse to crystallographic theory for this alloy. It was demonstrated that theoretical transformations paths exist from R-phase to B19′ that can yield more strain then the largest strain obtainable between B2 and B19′. Experimentally there was little difference in strain between the two transformation paths.

From these results it can be inferred that the R-phase to B19′ transformation can be utilized as effectively as the more commonly used B2 to B19′ transformation, in superelastic devices. Given that the R-phase has the ability to reorient and detwin, the R-phase to B19′

transformation has the added benefit of reduced stress and strain mismatch often observed between B2 and B19′ during transformation. Reducing stress and strain mismatch between respective phases could reduce the formation of plasticity formed during cycling through the phase transformation and extend the lifecycle of superelastic devices.

7.5 Tables

Table 7.1: B2 to R-phase Bain strains and R-phase variant conversion strains (%) calculated along the <111>$_{B2}$, <110>$_{B2}$ and <100>$_{B2}$ directions.

	Transformation Strain (%)				Variant Conversion Strain (%)		
Variant	<111>$_{B2}$	<110>$_{B2}$	<100>$_{B2}$	Variant Conversion	<111>$_{B2}$	<110>$_{B2}$	<100>$_{B2}$
A	0.9554	0.4788	0	A→B	1.2759	0	0
B	-0.3205	0.4788	0	A→C or D	1.2759	0.9576	0
C	-0.3205	-0.4811	0	B→C or D	0	0.9576	0
D	-0.3205	-0.4811	0	C→D	0	0	0

Table 7.2: B2 to B19′ transformation and R-phase (variants A and B) to B19' transformation strains (%) calculated along the <111>$_{B2}$, <110>$_{B2}$ and <100>$_{B2}$ directions.

	B2 to B19′ strain (%)			R-phase variant A to B19′ strain (%)			R-phase variant B to B19′ strain (%)		
B19′ variant	<111>$_{B2}$	<110>$_{B2}$	<100>$_{B2}$	<111>$_{B2}$	<110>$_{B2}$	<100>$_{B2}$	<111>$_{B2}$	<110>$_{B2}$	<100>$_{B2}$
1	-3.1	4.1	-3.6	-4.01	3.62	-3.59	-2.73	3.62	-3.59
1′	-3.1	-4.4	-3.6	-4.01	-4.88	-3.59	-2.73	-4.88	-3.59
2	10.3	4.1	-3.6	9.37	3.62	-3.59	10.65	3.62	-3.59
2′	-0.5	-4.4	-3.6	-1.42	-4.88	-3.59	-0.14	-4.88	-3.59
3	-0.5	-4.4	3.3	-1.42	-4.88	3.35	-0.14	-4.88	3.35
3′	10.3	4.1	3.3	9.37	3.62	3.35	10.65	3.62	3.35
4	-3.1	-4.4	3.3	-4.01	-4.88	3.35	-2.74	-4.88	3.35
4′	-3.1	4.1	3.3	-4.01	3.62	3.35	-2.74	3.62	3.35
5	-0.5	9.1	3.3	-1.42	8.66	3.35	-0.14	8.66	3.35
5′	10.3	9.1	3.3	9.37	8.66	3.35	10.65	8.66	3.35
6	-3.1	-2.8	3.3	-4.01	-3.27	3.35	-2.74	-3.27	3.35
6′	-3.1	-2.8	3.3	-4.01	-3.27	3.35	-2.74	-3.27	3.35

7.6 Figures
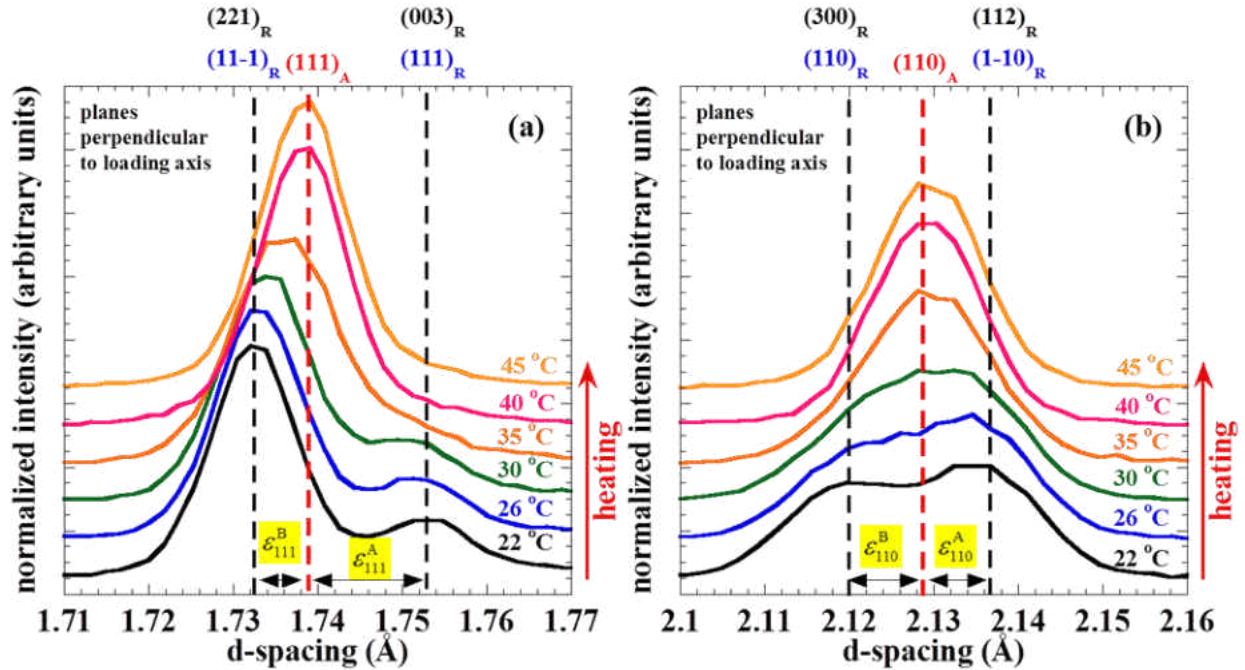
Figure 7.1: Selected normalized diffraction spectra acquired from lattice planes perpendicular to the loading direction that corresponde to isothermal loading and unloading at room temperature on cycle 5: (a) planes near 111 austenite; and (b) planes near 110 austenite.
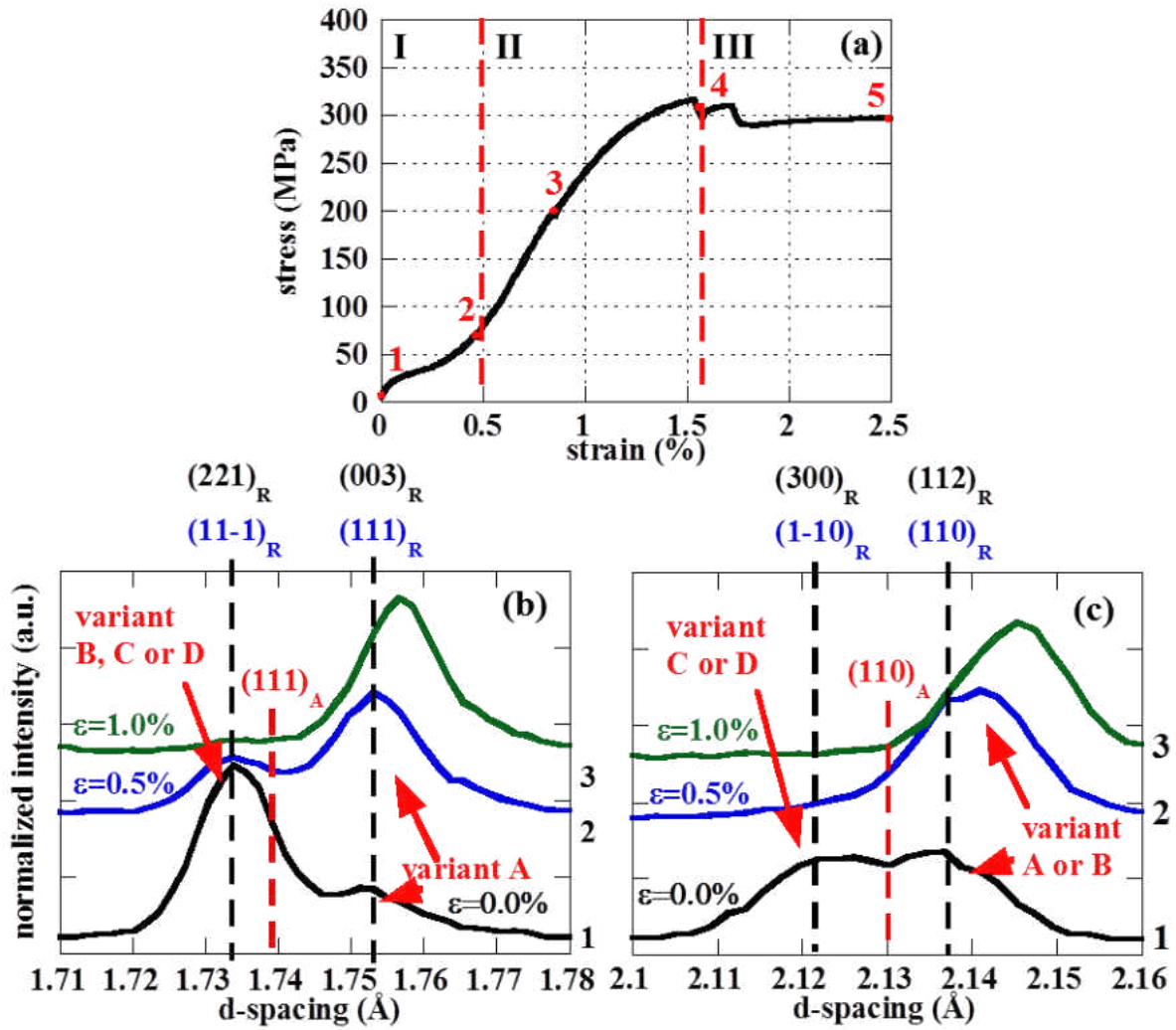
Figure 7.2: First cycle of uniaxial loading of superelastic NiTi at room temperature: (a) applied tensile stress vs. strain measured by exstensometry; and (b) corresponding normalized spectra acquired from lattice plane reflections with plane normals parallel to the loading direction (peaks near 111 austenite).
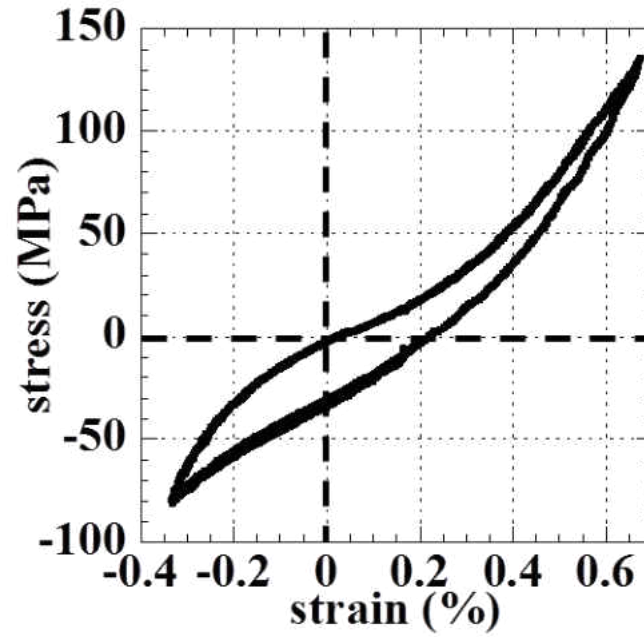
Figure 7.3: Macroscopic stress-strain response corresponding to two strain-controlled isothermal reverse loading cycles between -0.325 and 0.675% strain of R-phase in superelastic NiTi at room temperature.
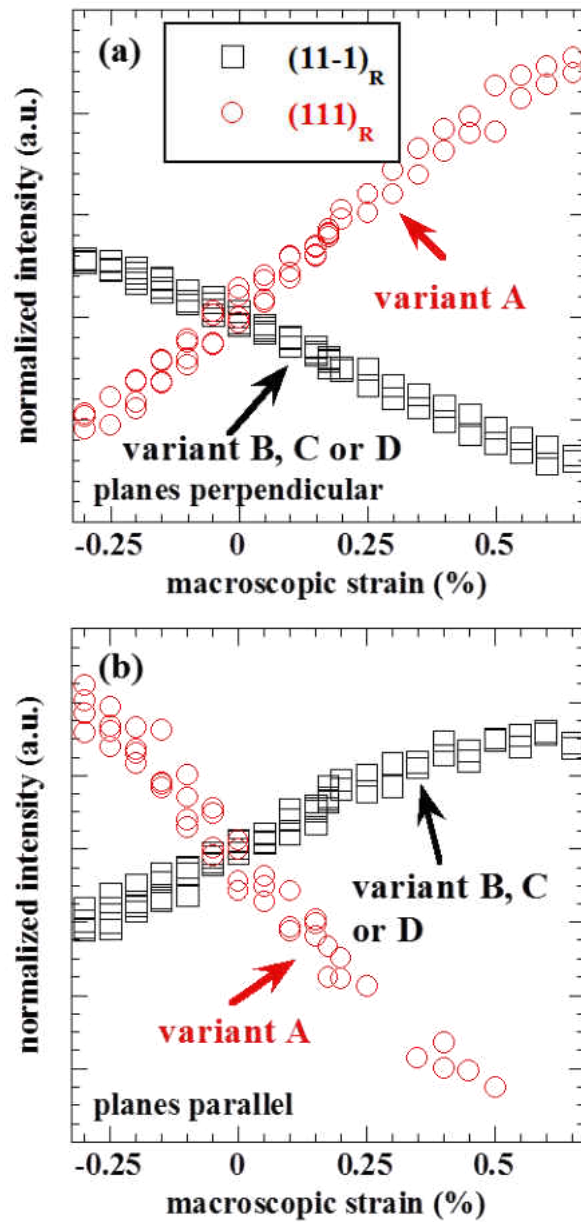
Figure 7.4: Normalized intensity of selected R-phase peaks acquired during strain-controlled isothermal reverse loading cycles between -0.325 and 0.675% strain of R-phase in superelastic NiTi at room temperature (i.e., corresponding to the macroscopic response shown in Figure 3) for: (a) planes perpendicular and (b) planes parallel to the loading axis. Note, that the intensity was normalized at zero strain.
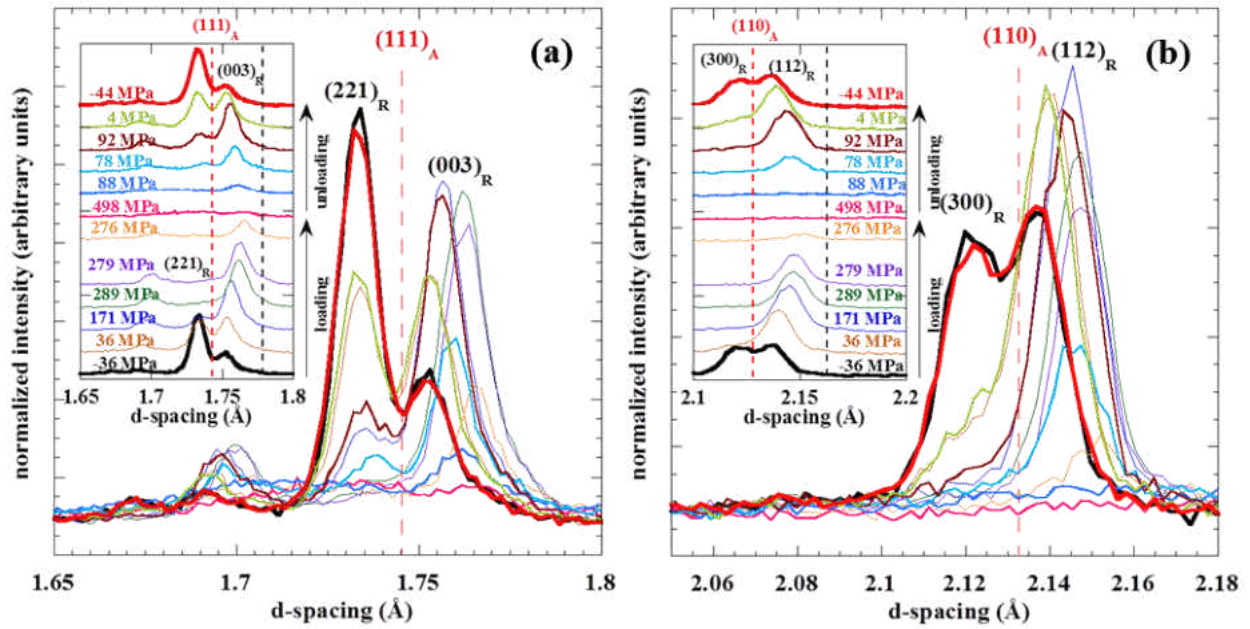
Figure 7.5: Selected normalized diffraction spectra acquired from lattice planes perpendicular to the loading direction that correspond to isothermal loading and unloading (to 500 MPa) at room temperature on cycle 5: (a) planes near 111 austenite; and (b) planes near 110 austenite.
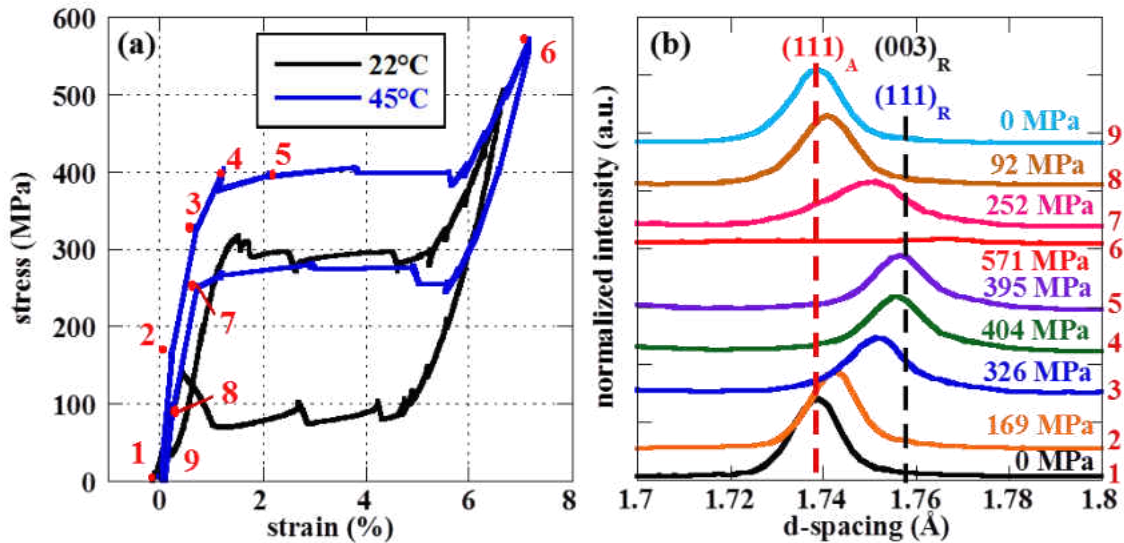
Figure 7.6: Isothermal loading and unloading up to 565 MPa of superelastic NiTi at 45°C: (a) applied tensile stress vs. strain measured by extensometry (the room temperature case is also shown for comparison); and (b) corresponding normalized spectra acquired from lattice plane reflections with plane normals parallel to the loading direction (peaks near 111 austenite).

118

CHAPTER EIGHT: NEUTRON DIFFRACTION MAPPING OF TEXTURE AND PHASE FRACTIONS IN HETEROGENOUS STRESS STATES DURING UNAXIAL/TORSIONAL LOADING OF SUPERELASTIC NITI

By recourse to in situ neutron diffraction during uniaxial/torsional loading and heating, thermoelastic deformation mechanisms in non-uniform states of stress in superelastic NiTi were spatially mapped. The preferred selection of R-phase variants formed by variant reorientation and detwinning processes were equivalent for the corresponding strain (in tension and compression) and the selection of such variant structures was reversible by isothermal loading. R-phase variant selection was consistent between uniaxial and torsional loading when the principal stress directions of the stress state were considered (for the crystallographic directions considered here). R-phase variants were tracked and the similarity in general behavior between uniaxial and torsional loading, in spite of the implicit heterogeneous stress state associated with torsional loading, pointed to the ability of the reversible thermoelastic transformation in NiTi to accommodate both stress and strain mismatch associated with deformation.

8.1 Introduction

Neutron diffraction provides an attractive alternative to electron and x-ray based diffraction techniques in which penetration depths can be limited to at most several microns (or millimeters in the case of x-rays from a synchrotron source) below the surface. The increased penetration depth of neutrons (up to several centimeters) allows for microstructural and micromechanical characterization representative of the bulk in polycrystalline materials. Furthermore, *in situ* neutron diffraction can provide residual and internal strain, crystallographic texture and phase fraction information during heating/cooling and mechanical loading. Recent

119

advances in diffraction based imaging have provided three-dimensional (3D) mappings of such information under heterogeneous states of stress observed during multi-axial loading. Examples of such investigations include the mapping of *hkl*-specific lattice strains in a 12L14 steel alloy [1] and a metastable 304L stainless steel that undergoes a strain induced phase transformation [73] – under tensile and torsional loading. Given the success of these recent investigations, the current study applies such diffraction techniques (specifically those utilized in Ref. [1]) to a hitherto not fully understood material systems that continuously evolve with changes in externally applied multi-axial stress. The ability to spatially map these real-time changes in crystallographic texture, internal strain and volume fractions of transforming crystallographic phases in the bulk in polycrystalline alloys while controlling the applied multi-axial stress, using *in situ* neutron diffraction, is a unique aspect of this work.

Shape memory alloys (SMAs) are materials that provide such an opportunity for study wherein shape recovery (up to 8% uniaxial strain in polycrystalline alloys) occurs against external uniaxial stress (up to 500 MPa) by means of a reversible thermoelastic solid state phase transformation.[4, 5] In NiTi, the phase transformation typically occurs between cubic B2, trigonal R and monoclinic B19', phases which are commonly referred to as austenite, R-phase and martensite, respectively. One particular SMA of interest is superelastic NiTi due to its successful use in biomedical applications including stents [68], orthodontic wires and eye glass frames, among others. In many of these applications, the presence of the R-phase can significantly alter the overall behavior of the SMA and its role is not fully understood [5, 53]. The R-phase, like martensite can detwin, reorient and undergo a thermal or stress induced transformation [13, 14]. For these reasons, it is difficult from ordinary macroscopic

measurements to decouple elastic and inelastic contributions (from their respective phases) to the overall deformation. *In situ* neutron diffraction is ideally suited to probing these microstructural and micromechanical changes while they occur under external stress fields. Furthermore, the R-phase has not been extensively studied when compared to the martensite and austenite phases. A better understanding of the R-phase can even aid in the development of R-phase actuators (e.g., in[3]) with reduced hysteresis and superior stability [15, 67, 72].

Despite SMAs typically operating under multi-axial stress states in applications, most previous *in situ* neutron diffraction based investigations on SMAs have been limited to homogenous stress states as a result of uniaxial loading [7, 9, 15, 16, 36, 43, 67, 71, 74-77]. Multi-axial loading and the accompanying heterogenous stress state during neutron diffraction has the added benefit of offering hiterto unexplored mechanistic insight in these alloys especially given that shear is expected to significantly affect deformation in the various phases and the phase transformation itself [4]. The selection of the various mechanisms (elasticity, plasticity, twinning and stress-induced transformation) to accommodate the mismatch in a heterogeneous stress state is also of interest. Thus, the current investigation spatially maps thermoelastic deformation mechanisms in non-uniform states of stress during multi-axial loading of superelastic NiTi by recourse to both conventional and recently advanced 3D resolved *in situ* neutron diffraction techniques.

8.2 Methods

The material used for all experiments was the same commercially available material used in Chapter 7 and additional details can be found in Section 7.2 in Chapter 7. All

thermomechanical testing was performed *in situ* using neutron diffraction at ORNL on the following instruments.

VULCAN Engineering Diffractometer:

The " VULCAN diffractometer at SNS was used to perform unaxial loading and heating experiments. Additional details regarding the experimental setups at SMARTS and VULCAN can be found in Section 2.2.1 in Chapter 2. Uniaxial tension/compression specimens, with a gauge diameter of 5.08 and length of 17.8 mm, were loaded using an axial torsion gripping system designed for an existing MTS load frame with maximum axial and torsional load capacities of 100kN and 400N·m, respectively. All heating was performed using an induction heater.

One specimen (designated *S1*) was subjected to heating from 22 to 45°C under no-load. Neutron spectra were acquired at 22, 26, 30, 35 and 45°C. To insure adequate statistics for analysis a hold time of 15 min was used to acquire each spectrum. A second specimen (designated *S2*) was subjected to compression-tension cyclic loaded between -0.325% and 6.75% strain at room temperature. Neutron data was acquired by continuous scanning. To insure adequate statistics a strain rate of 0.2 %/hour was maintained. Each reported neutron spectra represents statistics averaged over 15 min or 0.05 % strain.

Neutron Residual Stress Mapping Facility (NRSF2):

NRSF2 at HFIR was utilized to provide spatial resolved measurements in hetereogenous stress states during torsional loading. Additional details regarding the experimental setups at SMARTS and VULCAN can be found in Section 2.2.2 in Chapter 2. NRSF2 utilizes a Stoica-Popavici monochromotator and a wavelength of $\lambda=2.275$ Å was selected for all experiments.

Tension/torsion specimens were loaded using a portable axial torsion load frame with maximum axial and torsional load capacities of 50kN and 12N·m, respectively. Further details regarding the experimental setup can be found in Ref. [1]. All of the following experiments were performed at room temperature.

One specimen (designated *S3)*, with a gauge diameter of 7.00 mm and length of 50.8 mm, was subjected to torsional loading up to 550 MPa. Axial stress was maintained at 5 MPa for the duration of the experiment. A gauge volume of 2 x 2 x 2 mm^3 was established using gadolinium slits. Figure 8.2a shows the cross-section of the gauge volume within the specimen. The load frame was tilted to 43° (about the x-axis) to produce reflections from lattice planes near perpendicular to the directions of maximum (location 1, $Q_{-\theta z}$) and minimum (location 2, $Q_{+\theta z}$) normal stress. Neutron diffraction spectra were acquired at carefully selected shear stresses (as shown in the context of the results) at locations 1 and 2. To insure adequate statistics for analysis a hold time of 30 and 60 min was used to acquire each spectrum at a 2theta angle of 81.5° and 96°, respectively.

A second specimen (designated *S4*) with a gauge diameter of 5.08 mm and length of 50.8 mm, was subjected to torsional loading up to 500 MPa. Axial stress was maintained at 5 MPa for the duration of the experiment. A gauge volume of 0.5 x 20 x 0.5 mm^3 (width x height x width) was established using gadolinium slits. Figure 8.4a shows the cross-section of the gauge volume within the specimen. The load frame was positioned vertical, with the height of the gauge volume aligned with the length of the sample, to produce reflections from lattice planes perpendicular to the radial (location 1-5, Q_{radial}) and hoop (location 6, Q_{hoop}) directions of the specimen. Neutron diffraction spectra were acquired at carefully selected shear stresses (as

shown in context of the results) at each of the 6 locations. To insure adequate statistics for analysis a hold time of 10 min was used to acquire each spectrum at a 2theta angle of 81.5°.

8.3 Results and Discussion

Four biomedical grade superelastic NiTi (nominal composition 50.8 at.% Ni) cylindrical samples were investigated using *in situ* neutron diffraction at stress and temperature. Two samples (denoted *S1* and *S2*) were heated from room temperature to 45°C and compression-tension cyclically loaded between ±0.5% strain, respectively, at the "time-of-flight" VULCAN diffractometer at the SNS at ORNL. Two samples (denoted *S3* and *S4*) were subject to pure torsional loading (up to 550 MPa) with varying diffraction orientations and geometries (in order to investigate the principal, hoop and radial directions, respectively) using the Neutron Residual Stress Mapping Facility (NRSF2) at the steady-state High Flux Isotope Reactor (HFIR) at ORNL. More details regarding sample preparation, experimental setups and procedures can be found in the methods section.

Figure 8.1a shows a section of normalized neutron diffraction spectra acquired from crystallographic planes perpendicular to the length of the sample during cooling from 45°C to 22°C in sample *S1* under no applied load. The austenite to R-phase transformation occurs by elongating the B2 austenite cubic lattice along a (111) triad axis [14, 69, 71], resulting in the formation of a total of four possible variants during this transformation. One variant (henceforth designated variant A) corresponds to the elongated triad of the cube. The other three variants (henceforth designated variant B, C or D) correspond to the three contracted triads. This was observed experimentally in Figure 8.1a by the splitting of the $(111)_A$ austenite peak into $(11\text{-}1)_R$ and $(111)_R$ R-phase peaks during cooling from 45°C. At room temperature the system was

determined by Rietveld refinement [78] to be primarily R-phase with up to approximately 20 volume % austenite. Rietveld refinements were performed with phase volume fractions constrained to be equal between both spectra acquired from lattice planes perpendicular (with diffraction vector $Q_\parallel$ parallel to the loading axis) and parallel (with diffraction vector $Q_\perp$ perpendicular to the loading axis) to the length of the sample. The relative intensities (ratio of peak intensities from normalized spectra) of the $(11\text{-}1)_R$ and $(111)_R$ peaks were found to be 0.28 and 0.19 corresponding to $Q_\parallel$ and $Q_\perp$, respectively, which was comparable to that of sample *S2* (found to be 0.29 and 0.20 corresponding to $Q_\parallel$ and $Q_\perp$, respectively) following heat treatment prior to loading. In both cases the R-phase was formed by cooling from austenite under no-load and was thus considered to be the self-accommodated microstructure [5]. Note the self-accommodated R-phase microstructure in this system was not random and had fiber texture along the length of the samples (as indicated by unequal intensities between $Q_\parallel$ and $Q_\perp$, respectively). The intrinsic texture in this system was formed during processing and has been observed in comparable NiTi systems following similar processing [79].

The experimentally measured strains determined from peak positions (ε_1=0.86% and ε_2=-0.4%, as seen in Figure 8.1a) correlated well with the single crystal Bain strains calculated (as done previously in Ref. [69] using a distortion angle α determined from respective B2 and R-phase *hkl* peak positions measured in this work) from crystallographic theory for this alloy. The Bain strain associated with R-phase variant A and either B, C, or D w.r.t. the $\langle 111 \rangle_{B2}$ direction was found to be $\varepsilon_{111}^A = 0.96\%$ and $\varepsilon_{111}^B = -0.32\%$, respectively and allowed for the identification of these specific R-phase variants. By comparing crystallographic theory to experiment it was

apparent that the $(111)_R$ and $(11\text{-}1)_R$ peaks correspond to R-phase variant A and either B, C or D, respectively. In the following discussion, variants A and B, C or D refer to R-phase variants w.r.t. the $\langle 111 \rangle_{B2}$ direction and by evoking symmetry, variants B, C or D will be referred to as variant B unless otherwise stated (e.g., in Chapter 7). Details of the Bain strain calculations for the $(111)_A$ to R-phase transformation (as shown in Figure 8.1a) as well as for the $(110)_A$ to R-phase transformation (not shown here) can be found in Section 7.3.1 in Chapter 7.

Figure 8.1b shows a section of normalized neutron diffraction spectra acquired during isothermal uniaxial tension-compression (between -0.325% and 0.675% macroscopic strain) reverse cyclic loading of R-phase at room temperature in sample *S2*. At zero macroscopic strain, the relative diffracted peak intensities corresponding to variant A and variant B, Y_A/Y_B, was found to be 0.32 and 0.23 corresponding to $Q_\parallel$ and $Q_\perp$, respectively, which was indicative of a self-accommodated R-phase (as arrived at in Figure 8.1a, by cooling through the phase transformation under no-load). The relative peak intensities at approximately 0% strain were arbitrarily chosen as the references (i.e., $Y_0^A/Y_{zero}^A = 1$ and $Y_0^B/Y_{zero}^B = 1$ at 0% strain) for the normalization of relative peak intensities discussed in the following discussion. Thus the relative R-phase peak intensites are normalized w.r.t. to the self-accommodated microstructure and zero macroscopic strain. During loading in compression (from zero to -0.375% macroscopic strain) the peak intensity corresponding to variant A decreases at the expense of the peak intensity corresponding to variant B indicating reorientation and/or detwinning of R-phase variants. Note, increases in R-phase relative peak intensities may also be attributed to the formation R-phase from austenite under stress. However, the amount of austenite at room temperature was limited

to at most 20% volume fraction. Thus the major contribution to relative peak intesnity changes in the R-phase was attributed to reorientation and/or detwinning of R-phase variants.

As deformation was continued to -0.325% strain, the relative diffracted peak intensity corresponding to variant B ($Y^B_{-0.325}/Y^B_{zero}$) increased to 1.286, while the relative peak intensity corresponding to variant A ($Y^A_{-0.325}/Y^A_{zero}$) decreased to 0.452. This provided direct evidence of the preferred selection of R-phase B variants under compressive tensile loading. These B variants are preferentially selected in compression and susequnetly reorient to a near random self-accommodated distribution (as indicated by $Y^A_0/Y^A_{zero} = 1.012$ and $Y^B_0/Y^B_{zero} = 1.011$) when the deformation was reversed (from -0.325% to 0% strain) and the macroscopic strain approached 0%, pointing to the reversibility of the variant reorientation and detwinning processes. When deformation was continued in tension to 0.675% strain, preferred selection of R-phase variants was observed as an increase and decrease in relative peak intensities corresponding to variants A and B to 2.261 and 0.296, respectively. This provided direct evidence that variant A was the preferred R-phase variant under uniaxial tensile loading. These variants are preferentially selected in tension and reorient to a near random self-accommodated distribution when the deformation was reversed and the macroscopic strain approached 0%, again, validating the reversibility of variant reorientation and detwinning processes. Analogous preferred variant selection [36] under tension and compression and the isothermal reversibility of variant selection [65] by variant reorientation and/or detwinning of B19′ variants has been observed in martensitic NiTi.

The aforementioned R-phase variants tracked during uniaxial loading and heating at VULCAN were investigated in the principal stress directions during pure torsional loading at

NRSF2. Figure 8.2a shows the cross-section of cylindrical specimen *S3* and the two diffraction gauge volumes with the load frame tilted to 43° (about the x-axis). Note the load frame was titled to 43° during the experiment and was assumed to be tilted near to the ideal 45° when referring to the planes of maximum and minimum normal stress in the following discussion. This configuration produced reflections representative of the principal, hoop and radial stress directions under negative (location 1, with plane normals along the direction of minimum normal stress, or diffraction vector $Q_{-\theta z}$) and positive (location 2, with plane normals along the direction of maximum normal stress or diffraction vector $Q_{+\theta z}$) shear stresses. To facilitate the following discussion, the directions corresponding to maximum tensile and compressive stress will henceforth be referred to as the "tensile direction" and "compressive direction", respectively. Shear stresses shown in Figure 8.2b and c represent the maximum applied shear stress at the surface of the cylindrical NiTi sample. Figure 8.2b shows sections of normalized spectra from lattice planes perpendicular to the compressive direction (location 1) under pure torsional loading up to 500 MPa. From 0 to 300MPa, the intensity of the diffraction peak corresponding to variant B increased with shear stress and there was no detectable change in the diffraction peak corresponding to variant A. Figure 8.2c shows sections of normalized spectra from lattice planes perpendicular to the tensile direction (location 2) under pure torsional shear loading up to 550 MPa. The intensity of the diffraction peak corresponding to variant A increased with shear stress while that of variant B decreased. Thus, variant reorientation and detwinning was directly observed under torsional loading with preferred selection of variant A and variants B in the tensile and compressive directions, respectively.

Generally, the tension-compression asymmetry observed in the preferred selection of specific R-phase variants was consistent between uniaxial and torsional loading when the principal directions of the stress state were considered (for the crystallographic directions investigated here). At the maximum shear stress under torsional loading (as indicated by the red lines, in Figure 8.2b and c), the R-phase peak intensities' had decreased, but were still observable as the complete transformation to B19′ martensite had not occurred. This result was expected as the diffraction volumes used (at location 1 and 2 in Figure 8.2a) covered a large portion of the radius of the sample and thus represented reflections averaged over a heterogeneous stress state.

Figure 8.3a shows a section of normalized spectra from lattice planes perpendicular to the tensile direction (at location 2 in Figure 8.2a). On loading from -110 MPa to 100 MPa, the $(200)_R$ peak shifted to the right (indicating lattice strain) with negligible change in peak intensity (indicating minimal detwinning and variant reorientation). This result is consistent expected from crystallographic theory. The $(200)_R$ peak forms by an invariant transformation from the $(200)_A$ peak along the $\langle 100 \rangle_{B2}$ direction and variant conversion is not possible in this crystallographic direction (as described in detail in Chapter 7). At a maximum shear stress of 550 MPa the $(030)_M$ martensite peak was observed (as depicted by the red line). The $(030)_M$ martensite was undetectable in the compressive direction (at location 1 in Figure 8.1a) at a maximum shear stress of 550 MPa. The formation of $(030)_M$ martensite in the tensile direction and not in the compressive direction under torsional loading is indicative of preferred selection of B19′ variants in martensitic NiTi. Furthermore, $(030)_M$ martensite has previously been observed as a preferred variant formed under uniaxial tension [36, 63, 65]. This result suggests that martensite variant selection, like R-phase variant selection, is consistent between uniaxial and torsional loading

129

when the principal directions of the stress state were considered. However, this result cannot be deemed conclusive as only one of 12 correspondent variant pairs of B19′ martensite was considered here.

Figure 8.3b shows strains (indicated by ■) and Full Width at Half Maximum (FWHM, indicated by ●) determined from changes in d-spacing and peak breadth, respectively, of the $(200)_R$ peaks shown in Figure 8.3a. Results shown in Figure 8.3b summarize and facilitate the above discussion regarding the $(200)_R$ peaks shown in Figure 8.3a. An increasing linear relationship between shear stress and lattice strain for the $(200)_R$ peak was observed indicative of tensile strain. The relationship remains linear above 100 MPa when the $(200)_R$ peak begins to decrease as shown in Figure 8.3a. Thus, the $(200)_R$ decreased due to the phase transformation from R-phase to martensite with no contributions from variant and reorientation of R-phase variants. An increasing linear relationship between the FWHM and shear stress was observed and partly attributed to peak broadening caused by the averaging of strain over a heterogeneous stress state and stress-induced martensite.

In order to further investigate the heterogeneity of the stress state under torsional loading, diffraction peak intensities corresponding to variant B were spatially resolved (using a refined gauge volume) in the radial and hoop directions during pure torsional loading at NRSF2. Figure 8.4a shows the cross-section of cylindrical specimen *S4* with the six diffraction gauge volumes. The load frame was positioned vertical to produce reflections from lattice planes perpendicular to the radial (location 1-5, Q_{radial}) and hoop (location 6, Q_{hoop}) directions of the specimen. Note, strains in these directions are negligible under pure torsional loading, however phase fraction and texture evolution can still be observed as changes in peak intensity. Figure 8.4b shows the

normalized peak intensity (arbitrary units) corresponding to variant B as a function of the radial (mm) distance from the center of the sample to the center of the spatially resolved diffraction volumes (1 through 5) shown in Figure 8.4a. The shear stresses for which neutron data are presented in Figure 8.4b and labeled I-VIII are shown in Figure 8.4c. Figure 8.4c shows the macroscopic stress-strain response under pure torsional loading (up to 500 MPa) of sample *S4* at room temperature. All stresses shown represent the applied shear stress at the surface of the specimen.

The peak intensity at spatial locations 1-6 denoted as Y_i^{I} is shown in Figure 8.4b (as indicated by the black dashed line) and depicts the absorption profile in the initial condition (under no applied load). The data was corrected for absorption, normalized to point (1,I) and is defined as follows:

$$NI_i^j = \frac{Y_1^{\mathrm{I}}}{Y_i^{\mathrm{I}}} \cdot \frac{Y_i^j}{Y_1^j} \tag{1}$$

where subscript *i* increments through spatial locations 1-6, superscript *j* increments through shear stress values I-VIII, I is the uncorrected integrated intensity and *NI* is the normalized intensity shown in Figure 8.4b. The increase in peak intensity from points I to III corresponds to the preferred selection of variant B in the radial direction by R-phase detwinning and variant reorientation. Furthermore, the intensity increases with radius (points 1-5) corresponding to increasing stress. From Points III-VI the peak intensity decreases with stress due to transformation of detwinned/reoriented R-phase to B19′. At a maximum shear stress of 500 MPa (shown as Point VI) the peak intensity varies from 1 to 0 from the center of the cylinder to near the surface of cylinder corresponding to near zero stress at the center to maximum stress near the

surface. This is consistent with torsional loading, however the distribution of stress cannot be assumed to be linear with radius. From Points VI-VII the peak intensity remains unchanged indicating mostly elastic unloading of martensite.

Locations 5 and 6 are the same radial distance from the center of the sample. Location 5 corresponds to reflections from lattice planes perpendicular to the radial direction, while location 6 corresponds to reflections from lattice planes perpendicular to the hoop direction. During loading from 0 to 150 MPa (shown as points I-III) the intensity at locations 5 and 6 evolves differently with increasing shear stress. Following the onset of the phase transformation from R to B19′ (points IV-VI); the peak intensity at locations 5 and 6 evolves similarly with shear stress. This result suggests that preferred variant selection in the R-phase is different between the radial and hoop directions during torsional loading. This result is not expected during uniaxial loading in which lattice planes in both the radial and hoop are parallel to the loading direction (i.e., have plane normal in the $Q_\perp$ direction) and are under a homogenous compressive stress state governed by a reduction due to Poisson's ratio.

The aforementioned deformation mechanisms (i.e., elastic deformation, variant reorientation and detwinning in the R-phase and phase transformation from R-phase to martensite) investigated by recourse to *in situ* neutron diffraction are typically observed as changes in moduli in the macroscopic response. Figure 8.4c provides a connection between the diffraction results presented and the macroscopic behavior. Note extensometry could not be used due the large deformations associated with the experiment. Therefore, the shear strain shown in Figure 8.4c was calculated at the surface from the angle of twist measured at the grips and the effective gauge length of the cylindrical specimen. Deformation caused by loading from 0 to 200

MPa (points I to IV) is attributed to elastic deformation and detwinning and variant reorientation of R-phase. Point IV represents the onset of the phase transformation from R-phase to martensite. Deformation caused by loading from 200 to 500 MPa (points IV to VI) is attributed to the phase transformation from R-phase to martensite with additional but limited contributions from variant reorientation and detwinning and elastic deformation of martensite. Deformation caused by unloading from 500 MPa to 0 MPa (points V to VIII) is attributed to the reverse phase transformation from martensite to R-phase with additional but limited contributions from variant reorientation and detwinning and elastic recovery of martensite and R-phase. Loading/unloading up to 500 MPa was shown to be mostly recoverable here, however other irrecoverable mechanisms, e.g., dislocation based plasticity and deformation twinning maybe active to a limited degree.

8.4 Conclusions

Superelastic NiTi was investigated by recourse to *in situ* neutron diffraction during uniaxial and torsional loading. The experimentally measured strains correlated well with the single crystal Bain strains calculated from crystallographic theory for this alloy and allowed for the identification of specific R-phase variants. The identified variants were tracked in the principal stress, radial and hoop directions and spatially resolved measurements were made in a heterogeneous stress state observed during torsional loading. The aforementioned experiments are considered here together and the following conclusions were made with regards to the multiaxial loading of superelastic NiTi.

1. The preferred selection of R-phase variants formed by variant reorientation and detwinning processes were equivalent for the corresponding strain (in tension and

133

compression) and the selection of such variant structures was reversible by isothermal loading.

2. R-phase variant selection was consistent between uniaxial and torsional loading when the principal stress directions of the stress state were considered (for the crystallographic directions considered here).

3. Variant reorientation and detwinning and phase fractions correlated well with shear stress, which varied from zero at the center of the cylinder to a maximum near the surface under torsional loading.

Conclusion (1) has previously been demonstrated for B19′ in martensitic shape memory NiTi [65]. Limited results presented here suggest that B19′ variant selection abide with conclusions (2) and (3), however, these results cannot be deemed conclusive as only one of 12 correspondent variant pairs of B19′ martensite was considered. The results presented here, track for the first time R-phase variants in a spatially resolved mode in NiTi during multi-axial loading. The similarity in behavior between uniaxial and torsional loading, in spite of the implicit heterogeneous stress state associated with torsional loading points to ability of the reversible thermoelastic transformation in NiTi to accommodate both stress and strain mismatch associated with deformation. This accommodation is necessary to ensure reversibility of the transformation (whether thermal or stress-induced) and the observed results thus validate the fundamental nature of thermoelastic martensitic transformations.

8.5 Figures
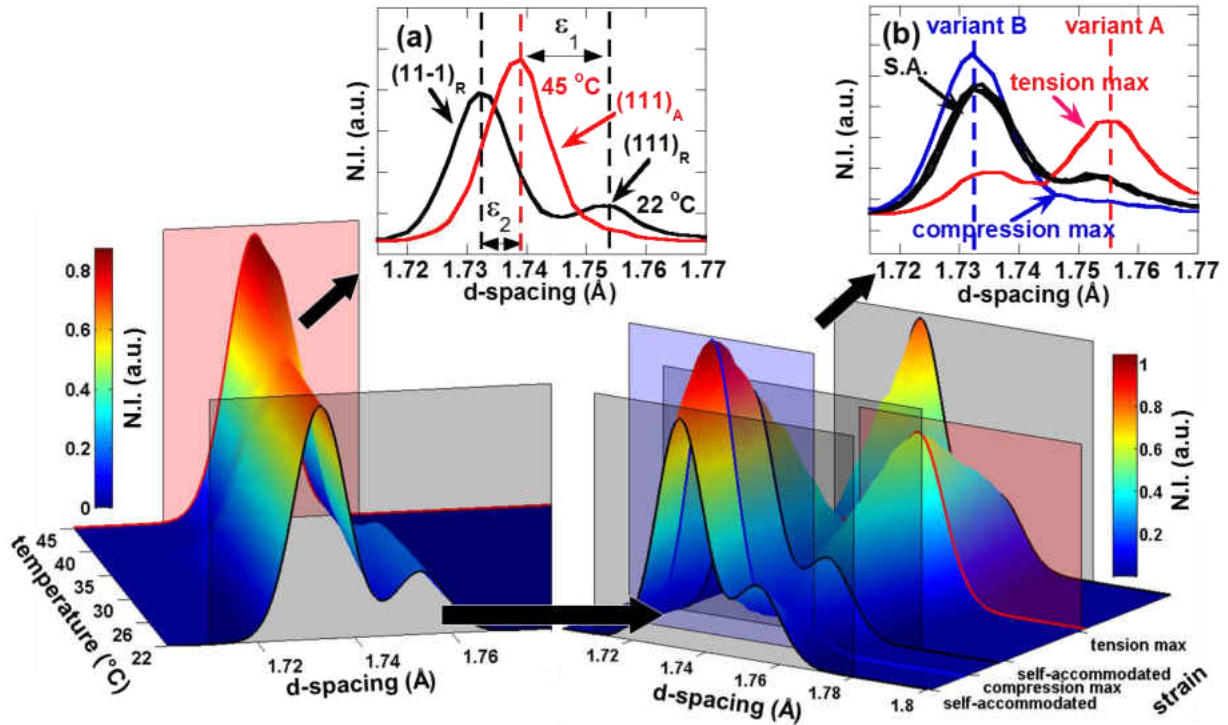
Figure 8.1: Section of normalized neutron diffraction spectra acquired during (a) cooling from cubic austenite (B2) to trigonal R-phase in the absence of an applied external load and (b) isothermal uniaxial tension-compression reverse cyclic loading of trigonal R-phase at room temperature, in NiTi. Red corresponds to cubic austenite and black to the trigonal R-phase in (a). Black corresponds to self-accommodated (0%), blue to maximum compressive (-0.325%) and red to maximum tensile (0.675%) strains in (b). Reflections are from crystallographic planes perpendicular to the length of the sample. R-phase variants A and B in (b) were identified by correlating measured strains ε_1 and ε_2 in (a) to Bain strains (for the B2 to R-phase transformation in NiTi) determined from crystallographic theory.
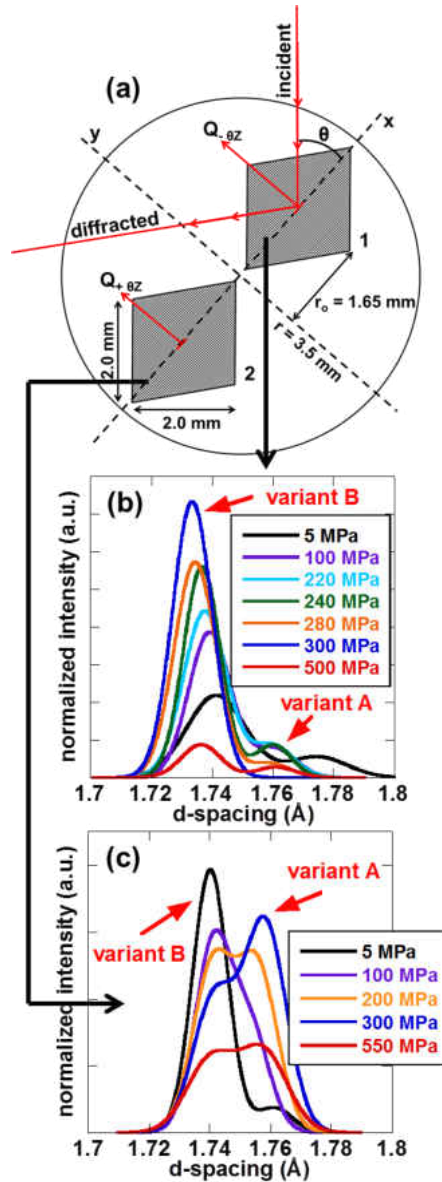
Figure 8.2: Neutron diffraction spectra from planes in the principle stress directions under pure torsional loading at room temperature: (a) cross-section of cylindrical specimen with the two diffraction gauge volumes. The load frame was tilted to 43° (about the x-axis) to produce reflections from lattice planes near perpendicular to the directions of maximum (location 1, $Q_{-\theta z}$) and minimum (location 2, $Q_{+\theta z}$) normal stress. Also, shown are the corresponding sections of normalized neutron diffraction spectra acquired from (b) location 1 and (c) location 2. All stresses shown represent the applied shear stress at the surface the specimen. Variants A and B (as identified in Figure 8.1) are shown to preferentially select in the $Q_{-\theta z}$ ("tensile") and $Q_{+\theta z}$ ("compressive") directions as demonstrated in (c) and (b), respectively, under torsional loading.

136
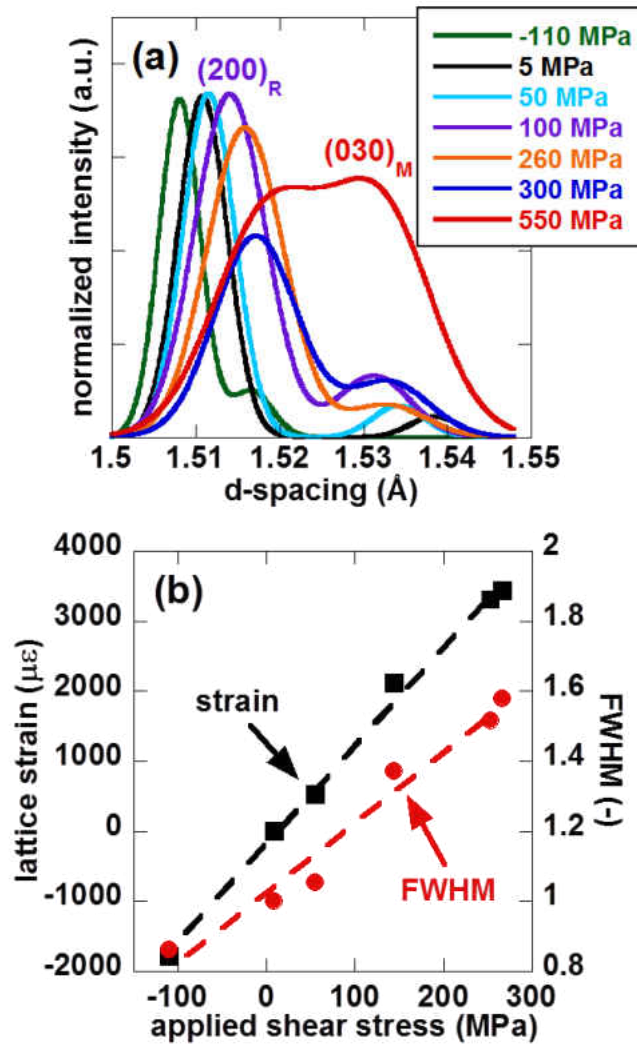
Figure 8.3: (a) Section of normalized neutron diffraction spectra acquired at location 1 (shown in Figure 2a) for reflections from lattice planes perpendicular to the direction of maximum normal stress ($Q_{-\theta z}$, "tensile direction") under pure torsional loading at room temperature. (b) Strains (indicated by ■) and Full Width at Half Maximum (FWHM, indicated by ●) determined from changes in d-spacing and peak breadth, respectively, of the $(200)_R$ peaks shown in (a). All stresses shown represent the applied shear stress at the surface the specimen.
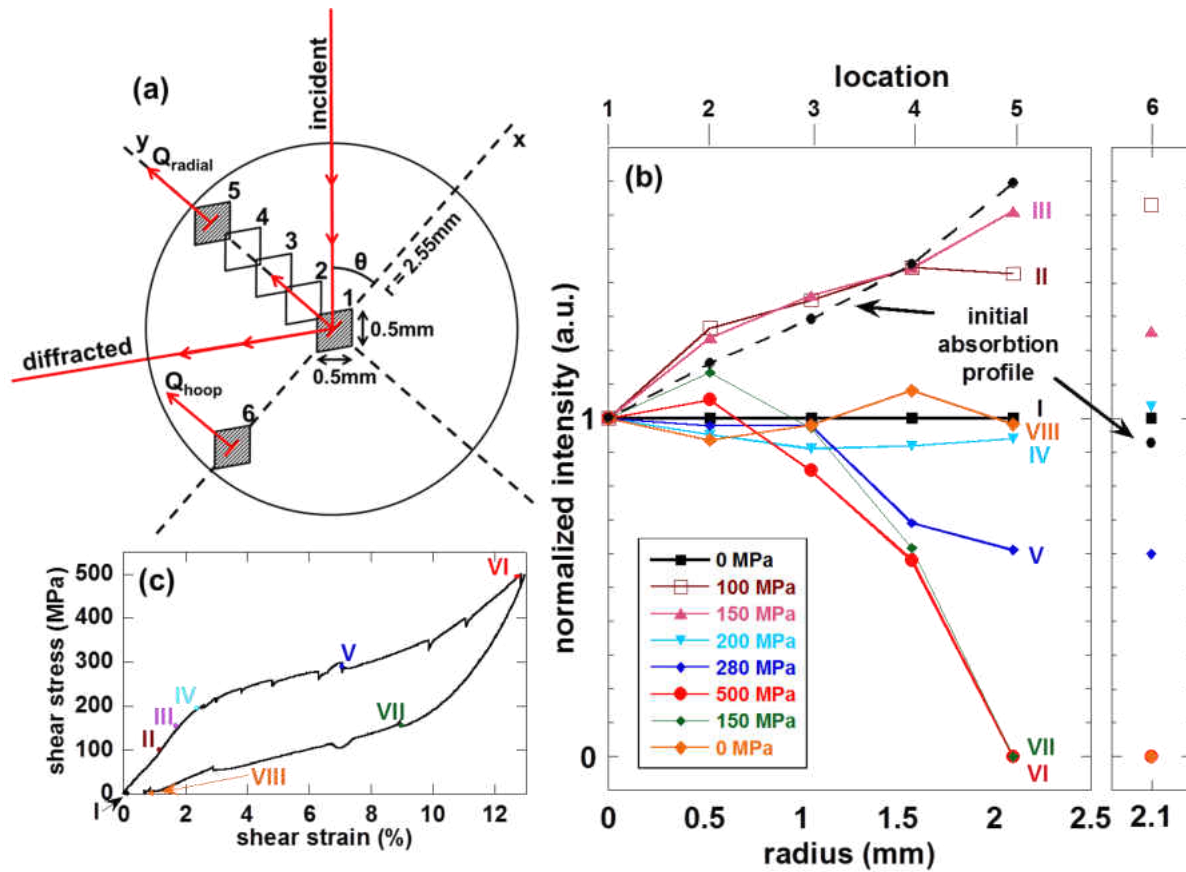
Figure 8.4: Analyses of neutron diffraction spectra corresponding to radial and hoop directions under pure torsional loading at room temperature: (a) cross-section of the cylindrical specimen with the six diffraction gauge volumes. The load frame was positioned vertical to produce reflections from lattice planes perpendicular to the radial (location 1-5, Q_{radial}) and hoop (location 6, Q_{hoop}) directions of the specimen. (b) Normalized intensity of the peak corresponding to variant B as a function of the radial (mm) distance from the center of the sample to the centroid of the diffraction volumes. All diffraction peaks were normalized to an absorption profile acquired under no applied load. (c) The macroscopic stress-strain response (stresses for which neutron data is presented are labeled I-VIII). All stress values shown represent the applied shear stress at the surface the specimen.

138

CHAPTER NINE: CONCLUSIONS

The content of this dissertation consist of a compilation of papers divided into chapters and each chapter contains its own conclusions. This final chapter provides a summary of the conclusions in a manner that highlights the impact of this dissertation.

SMAs are materials that provided a unique opportunity for study wherein shape recovery (up to 8% uniaxial strain in polycrystalline alloys) occurs against external uniaxial stress (up to 500 MPa) by means of a reversible thermoelastic solid state phase transformation. In NiTi, the phase transformation typically occurs between cubic B2, trigonal R and monoclinic B19', phases which are commonly referred to as austenite, R-phase and martensite, respectively. The ability to do work while transforming from one phase to another due to a temperature change enables their use as high-force actuators in automotive and aerospace applications with both sensory and actuation functions. One particular SMA of interest is superelastic NiTi due to its successful use in biomedical applications including stents, orthodontic wires and eye glass frames, among others. In many of these applications, the presence of the R-phase can significantly alter the overall behavior of the SMA and its role is not fully understood. The R-phase, like martensite can detwin, reorient and undergo a thermal or stress induced transformation. For these reasons, it is difficult from ordinary macroscopic measurements to decouple elastic and inelastic contributions (from their respective phases) to the overall deformation. *In situ* neutron diffraction is ideally suited to probing these microstructural and micromechanical changes while they occur under external stress fields. Furthermore, the R-phase has not been extensively studied when compared to the martensite and austenite phases. A better understanding of the R-phase can even aid in the development of R-phase actuators with reduced hysteresis and superior stability.

Despite SMAs typically operating under multi-axial stress states in applications, most previous *in situ* neutron diffraction based investigations on SMAs have been limited to homogenous stress states as a result of uniaxial loading. Multi-axial loading and the accompanying heterogeneous stress state during neutron diffraction has the added benefit of offering hiterto unexplored mechanistic insight in these alloys especially given that shear is expected to significantly affect deformation in the various phases and the phase transformation itself. The selection of the various mechanisms (elasticity, plasticity, twinning and stress-induced transformation) to accommodate the mismatch in a heterogeneous stress state is also of interest. Thus, the current investigation spatially mapped thermoelastic deformation mechanisms in non-uniform states of stress during uniaxial and multi-axial loading of shape memory and superelastic NiTi by recourse to both conventional and recently advanced 3D resolved *in situ* diffraction techniques. Towards this goal, *in situ* neutron diffraction experiments were performed at Los Alamos and Oak Ridge National Laboratories and synchrotron x-ray diffraction experiments were performed at Deutsches Elektronen-Synchrotron (DESY) in Hamburg, Germany. SMA spring actuators were also used to experimentally validate the ability of a recently developed model to predict the evolutionary deformation response under multi-axial loading conditions. All experiments are considered here together and the following conclusions were made with regards to multiaxial loading and heating of shape memory and superelastic NiTi.

1.) SMA spring actuators were used to experimentally validate the ability of a recently developed model to predict the evolutionary deformation response under multi-axial loading conditions. With a heterogeneous stress state that evolves with cycling, SMA

spring actuators provided a "worst case" scenario for SMA model validation. Under complex and evolving stress states the boundary conditions imposed are expected to have significant effects on SMA behavior. This successful experimental validation of the simulated response of SMA spring actuators proved the feasibility of modeling and designing SMA actuators, in complex forms, to operate under a multiaxial state of stress for an extended number cycles. The effects of boundary conditions (i.e., rotationally constrained and unconstrained) SMA spring actuators were experimentally captured, thus highlighting their need to be considered during the modeling and design process.

2.) *In situ* neutron diffraction was used to provide insight into martensite variant structures during isothermal, isobaric, and isostrain loading in shape memory NiTi. Results show variant structures were equivalent for the corresponding strain and more importantly, the reversibility and equivalency was immediately evident in a variant structure that was first formed isobarically but then reoriented to a near random self-accommodated structure by isothermal deformation. Variant structures formed isothermally were not significantly affected by a subsequent thermal cycle under constant strain. In all loading cases, the resulting variant structure correlated with strain and did not correlate with stress.

3.) During uniaxial/torsional loading and heating, thermoelastic deformation mechanisms in non-uniform states of stress in superelastic NiTi were spatially mapped. The preferred selection of R-phase variants formed by variant reorientation and detwinning processes were equivalent for the corresponding strain (in tension and compression) and the selection of such variant structures was reversible by isothermal loading. R-phase variant

selection was consistent between uniaxial and torsional loading when the principal stress directions of the stress state were considered (for the crystallographic directions considered here). R-phase variants were tracked and the similarity in general behavior between uniaxial and torsional loading, in spite of the implicit heterogeneous stress state associated with torsional loading, pointed to the ability of the reversible thermoelastic transformation in NiTi to accommodate both stress and strain mismatch associated with deformation.

Overall, various thermomechanical combinations of heating and loading sequences in SMAs yielded the same final texture (preferred selection of variants), which highlights the ability to take different paths yet still obtain the desired actuator response while minimizing irrecoverable deformation mechanisms. Based on the ability to obtain a texture for a given strain after varying loading and heating histories, it can be inferred that the results presented in this dissertation could be obtained by following any sequence of loading and heating over multiple cycles. Therefore, the loading and heating path which minimizes the activation of irrecoverable processes and most efficiently produces the desired response should be considered in the design and fabrication process of SMA actuators and superelastic devices. Such loading and heating paths have implications for minimizing the number of cycles required to train an SMA, which limits the amount of work required for stabilizing their evolutionary response thereby increasing the fatigue life and overall durability of the SMA. This finding is valuable to the aerospace and medical device industries where SMAs find current application.

APPENDIX: MATLAB SCRIPTS

Mapping of B2 to B19′ Bain strains in monoclinic IPF

```matlab
clear all; clc;

%B19' monoclinic lattice parameters
a=2.91;
b=4.65;
c=4.13;
gam= 97.57;

gamma=(gam/360)*2*pi; %monoclinic angle

%B2 cubic lattice parameters

d_100B2=3.03;

% coordinate transformation matrix; metric for B19' space for monoclinic
G=[a b*cos(gamma) 0;...
    0 b*sin(gamma) 0;...
    0 0 c];

% transformation matrix

B=[a/d_100B2 b*cos(gamma)/(sqrt(2)*d_100B2) 0;...
    0 b*sin(gamma)/(sqrt(2)*d_100B2) 0;...
    0 0 c/(sqrt(2)*d_100B2)];

h=0;

% stereographic projection of transformation strains into monoclinic IPF

for i=-5:5;
    for j=0:10;
        for k=0:10;
            if i==0 && j==0 && k==0;
                break
            end
            h=h+1;
            v=[i;j;k];
            v_hkl(h,:)=v;
            v=v/norm(v);
            p=inv(G)*v; %% inverse of the metric yields normal space
            p=p/norm(p);
            x(h)=p(1)/(1+abs(p(3))); %stereographic projection
            y(h)=p(2)/(1+abs(p(3))); %stereographic projection

            e(h)=(norm(B*v)-norm(v))/norm(v)*100; %% transformation strain
for a given hkl

        end
    end
```

```matlab
end

%plotting of IPF
ti = -1:.01:1; bi=0:.01:1;
[XI,YI] = meshgrid(ti,bi);
ZI = griddata(x,y,e,XI,YI);
contourf(XI,YI,ZI,20)
colorbar
colormap(flipud(hot))
colormapeditor
```

B2 cubic to R-phase Bain strain calculations

```matlab
clear all; clc;

alpha=89.45; %bain angle (degrees)

alp=(alpha/360)*2*pi;

%Bain distortion matrix
B=[sqrt(2)*sin(alp/2) 0 0;...
    0 sqrt(2)*sin(alp/2) 0;...
    0 0 sqrt(3-4*sin(alp/2)^2)];

%coordinate transformation matrix
R_a=[1/sqrt(2) -1/sqrt(6) -1/sqrt(3);... %variant A
    1/sqrt(2) 1/sqrt(6) 1/sqrt(3);...
    0 -2/sqrt(6) 1/sqrt(3)];

R_b=[1/sqrt(2) 1/sqrt(6) 1/sqrt(3);... %variant B
    -1/sqrt(2) 1/sqrt(6) 1/sqrt(3);...
    0 -2/sqrt(6) 1/sqrt(3)];

R_c=[-1/sqrt(2) -1/sqrt(6) -1/sqrt(3);... %variant C
    1/sqrt(2) -1/sqrt(6) -1/sqrt(3);...
    0 -2/sqrt(6) 1/sqrt(3)];

R_d=[-1/sqrt(2) -1/sqrt(6) -1/sqrt(3);... %variant D
    -1/sqrt(2) 1/sqrt(6) 1/sqrt(3);...
    0 2/sqrt(6) -1/sqrt(3)];

%shape strain matrix (T)
T(:,:,1)=R_b*B*inv(R_b);

T(:,:,2)=R_c*B*inv(R_c);

T(:,:,3)=R_a*B*inv(R_a);

T(:,:,4)=R_d*B*inv(R_d);

%transformation strain

v=[1 1 2;1 1 2;1 0 1];

for j=1:3;
    for i=1:4;
        e(i,j)=(norm(T(:,:,i)*v(:,j))-norm(v(:,j)))/norm(v(:,j))*100;
    end
end
```

B2 cubic to B19′ monoclinic Bain strain calculations

```matlab
clear all; clc;


%B19' monoclinic lattice parameters
a=2.902;
b=4.138;
c=4.646;
bet= 96.554;


beta=(bet/360)*2*pi; %monoclinic angle

%B2 lattice parameters

d_100B2=3.01;


d_110B2=d_100B2/sqrt(2);


%deformation matrix

G=[a/d_100B2 0 -c*sin(beta-pi/2)/(2*d_110B2);...
   0 b/(2*d_110B2) 0;...
   0 0 c*cos(beta-pi/2)/(2*d_110B2)];

%rotation matrices for each variant

R_A(:,:,1)=[1 0 0;...                       %variant 1
   0 1/sqrt(2) -1/sqrt(2);...
   0 1/sqrt(2) 1/sqrt(2)];


R_A(:,:,2)=[-1 0 0;...                      %variant 1'
   0 -1/sqrt(2) -1/sqrt(2);...
   0 -1/sqrt(2) 1/sqrt(2)];


R_A(:,:,3)=[1 0 0;...                       %variant 2
   0 -1/sqrt(2) -1/sqrt(2);...
   0 1/sqrt(2) -1/sqrt(2)];


R_A(:,:,4)=[-1 0 0;...                      %variant 2'
   0 1/sqrt(2) -1/sqrt(2);...
   0 -1/sqrt(2) -1/sqrt(2)];


R_A(:,:,5)=[0 -1/sqrt(2) 1/sqrt(2);...      %variant 3
   1 0 0;...
   0 1/sqrt(2) 1/sqrt(2)];


R_A(:,:,6)=[0 1/sqrt(2) 1/sqrt(2);...       %variant 3'
   -1 0 0;...
   0 -1/sqrt(2) 1/sqrt(2)];
```

```matlab
R_A(:,:,7)=[0 1/sqrt(2) 1/sqrt(2);...          %variant 4
    1 0 0;...
    0 1/sqrt(2) -1/sqrt(2)];

R_A(:,:,8)=[0 -1/sqrt(2) 1/sqrt(2);...          %variant 4'
    -1 0 0;...
    0 -1/sqrt(2) -1/sqrt(2)];

R_A(:,:,9)=[0 1/sqrt(2) 1/sqrt(2);...          %variant 5
    0 -1/sqrt(2) 1/sqrt(2);...
    1 0 0];

R_A(:,:,10)=[0 -1/sqrt(2) 1/sqrt(2);...          %variant 5'
    0 1/sqrt(2) 1/sqrt(2);...
    -1 0 0];

R_A(:,:,11)=[0 1/sqrt(2) -1/sqrt(2);...          %variant 6
    0 1/sqrt(2) 1/sqrt(2);...
    1 0 0];

R_A(:,:,12)=[0 -1/sqrt(2) -1/sqrt(2);...          %variant 6'
    0 -1/sqrt(2) 1/sqrt(2);...
    -1 0 0];

%transformation strain

v=[1 1 1;1 1 0;1 0 0];

for j=1:3;
    for i=1:12;
        e_A(i,j)=(norm(R_A(:,:,i)*G*inv(R_A(:,:,i))*v(:,j))-
norm(v(:,j)))/norm(v(:,j))*100;
    end
end
```

REFERENCES

[1] Woracek R, Bunn J R, Penumadu D and Hubbard C R 2012 Method to determine *hkl* strains and shear moduli under torsion using neutron diffraction *Applied Physics Letters* **100** 191904-5

[2] Benafan O, Padula S A, Skorpenske H D, An K and Vaidyanathan R 2014 Design and implementation of a multiaxial loading capability during heating on an engineering neutron diffractometer *Review of Scientific Instruments* **85** 103901

[3] Benafan O, Notardonato W U, Meneghelli B J and Vaidyanathan R 2013 Design and development of a shape memory alloy activated heat pipe-based thermal switch *Smart Materials and Structures* **22** 105017

[4] Bhattacharya K (ed) 2003 *Microstructure of Martensite: Why It Forms and How It Gives Rise to the Shape-Memory Effect?* (New York: Oxford University Press)

[5] Otsuka K and Wayman C M (ed) 1999 *Shape Memory Materials* (Cambridge: Cambridge University Press)

[6] Lagoudas D C (ed) 2008 *Shape memory alloys: modeling and engineering applications* (Springer Verlag)

[7] Benafan O, Padula II S A, Noebe R D, Sisneros T and Vaidyanathan R 2012 Role of B19' martensite deformation on the stability of NiTi two-way shape memory effect *Journal of Applied Physics* **112** 093510

[8] Stebner A P, Vogel S C, Noebe R D, Sisneros T, Clausen B, Brown D W, Garg A and Brinson L C 2013 Micromechanical quantification of elastic, twinning, and slip strain partitioning exhibited by polycrystalline, monoclinic nickel-titanium during large uniaxial deformations measured via in-situ neutron diffraction *Journal of the Mechanics and Physics of Solids* **61** 2302-2330

[9] Benafan O, Noebe R D, Padula Ii S A, Garg A, Clausen B, Vogel S and Vaidyanathan R 2013 Temperature dependent deformation of the B2 austenite phase of a NiTi shape memory alloy *International Journal of Plasticity* **51** 103-121

[10] Benafan O, Noebe R D, Padula II S A, Brown D W, Vogel S and Vaidyanathan R 2014 Thermomechanical cycling of a NiTi shape memory alloy - macroscopic response and microstructural evolution *International Journal of Plasticity* **56** 99-118

[11] Hebda D A and White S R 1995 Effect of training conditions and extended thermal cycling on nitinol two-way shape memory behavior *Smart materials and structures* **4** 298

[12]   Wang Z, Zu X, Feng X and Dai J 2002 Effect of thermomechanical treatment on the two-way shape memory effect of NiTi alloy spring *Materials Letters* **54** 55-61

[13]   Miyazaki S and Otsuka K 1986 Deformation and transition behavior associated with the R-phase in Ti-Ni alloys *Metallurgical and Materials Transactions A* **17A** 53-63

[14]   Šittner P, Landa M, Lukáš P and Novak V 2006 R-phase transformation phenomena in thermomechanically loaded NiTi polycrystals *Mechanics of Materials* **38** 475-492

[15]   Krishnan V B, Shmalo S B, Rathod C R, Bourke M A M and Vaidyanathan R 2010 Low temperature deformation of the R-phase in a NiTiFe shape memory alloy *Applied Physics Letters* **97** 091910-3

[16]   Benafan O, Noebe R D, Padula II S A, Gaydosh D J, Lerch B A, Garg A, Bigelow G S, An K and Vaidyanathan R 2013 Temperature dependent behavior of a polycrystalline NiTi shape memory alloy around the transformation regime *Scripta Materialia* **68** 571-574

[17]   An K, Skorpenske H D, Stoica A D, Ma D, Wang X and Cakmak E 2011 First *in situ* lattice strains measurements under load at VULCAN *Metallurgical and Materials Transactions A* **42** 95-99

[18]   Benafan O, Padula S A, Skorpenske H D, An K and Vaidyanathan R 2014 Design and implementation of a multiaxial loading capability during heating on an engineering neutron diffractometer *Review of Scientific Instruments* **85** -

[19]   Hutchings M T, Withers P J, Holden T M and Lorentzen T (ed) 2005 *Introduction to the Characterization of Residual Stress by Neutron Diffraction* (Taylor & Francis)

[20]   Von Dreele R B 1997 Quantitative texture analysis by Rietveld refinement *Journal of Applied Crystallography* **30** 517-525

[21]   Larson A C and Von Dreele R B 2004 General Structure Analysis System (GSAS) *Los Alamos National Laboratory Report LAUR 86-748*

[22]   Wessel P and Smith W H F 1995 New verison of the generic mapping tools *EOS Transactions American Geophysical Union* **76**

[23]   Dhakal B, Nicholson D E, Saleeb A F, Padula II S A and Vaidyanathan R 2016 Three-dimensional deformation response of a NiTi shape memory helical-coil actuator during thermomechanical cycling: experimentally validated numerical model *Smart Materials and Structures* **25** 095056

[24]   Bhattacharya K and James R D 2005 The material is the machine *Science* **307** 53-54

[25] Calkins F T and Mabe J H 2010 Shape memory alloy based morphing aerostructures *Journal of Mechanical Design* **132** 111012

[26] Calkins F T and Mabe J H 2016 Flight test of a shape memory alloy actuated adaptive trailing edge flap *ASME 2016 Conference on Smart Materials, Adaptive Structures and Intelligent Systems* (2016) American Society of Mechanical Engineers

[27] Hartl D J, Lagoudas D C, Calkins F T and Mabe J H 2010 Use of a Ni60Ti shape memory alloy for active jet engine chevron application: I. Thermomemchanical characterization *Smart Materials and Structures* **19** 015020

[28] Mabe J H, Calkins F T and Butler G W 2002 Boeing's variable geometry chevron, morphing aerostructure for jet noise reduction *47th AIAA/ASME/ASCE/AHS/ASC Structures, Structural Dynamics and Materials Conference* (Newport, Rhode Island, 2002)

[29] Mabe J 2008 Variable area jet nozzle for noise reduction using shape memory alloy actuators *Journal of the Acoustical Society of America* **123** 3871-3871

[30] Nicholson D E, Bass M A, Mabe J H, Benafan O, Padula S A and Vaidyanathan R 2016 Heating and loading paths to optimize the performance of trained shape memory alloy torsional actuators *ASME 2016 Conference on Smart Materials, Adaptive Structures and Intelligent Systems* (2016) American Society of Mechanical Engineers

[31] Scholten W D, Patterson R, Chapelon Q, Hartl D J, Strganac T W and Turner T L 2017 Experimentation and computational analysis of an SMA-based slat-cove filler for noise reduction in a high lift wing *25th AIAA/AHS Adaptive Structures Conference* (2017) 0732

[32] Saleeb A F, Padula II S A and Kumar A 2011 A multi-axial, multimechanism based constitutive model for the comprehensive representation of the evolutionary response of SMAs under general thermomechanical loading conditions *International Journal of Plasticity* **27** 655-687

[33] Saleeb A F, Dhakal B, Hosseini M S and Padula II S A 2013 Large scale simulation of NiTi helical spring actuators under repeated thermomechanical cycles *Smart Materials and Structures* **22** 094006

[34] Ma J, Karaman I and Noebe R D 2010 High temperature shape memory alloys *International Materials Reviews* **55** 257-315

[35] Nicholson D E, Padula II S A, Noebe R D, Benafan O and Vaidyanathan R 2014 Thermomechanical behavior of NiTiPdPt high temperature shape memory alloy springs *Smart Materials and Structures* **23** 125009

[36]   Qiu S, Clausen B, Padula II S A, Noebe R D and Vaidyanathan R 2011 On elastic moduli and elastic anisotropy in polycrystalline martensitic NiTi *Acta Materialia* **59** 5055-5066

[37]   Qiu S, Krishnan V B, Padula S A, Noebe R D, Brown D W, Clausen B and Vaidyanathan R 2009 Measurement of the lattice plane strain and phase fraction evolution during heating and cooling in shape memory NiTi *Applied Physics Letters* **95** 141906-3

[38]   Padula S A, Qiu S, Gaydosh D, Noebe R, Bigelow G, Garg A and Vaidyanathan R 2012 Effect of upper-cycle temperature on the load-biased, strain-temperature response of NiTi *Metallurgical and Materials Transactions A* **43** 4610-4621

[39]   Manchiraju S, Gaydosh D, Benafan O, Noebe R, Vaidyanathan R and Anderson P M 2011 Thermal cycling and isothermal deformation response of polycrystalline NiTi: Simulations vs. experiment *Acta Materialia* **59** 5238-5249

[40]   Benafan O, Padula II S A, Noebe R D, Brown D W, Clausen B and Vaidyanathan R 2013 An *in situ* neutron diffraction study of shape setting NiTi shape memory alloy *Acta Materialia* **61** 3585

[41]   Ancker C J and Goodier J N 1958 Pitch and curvature corrections for helical springs *Journal of Applied Mechanics* 466-487

[42]   Padula II S A, Gaydosh D J, Saleeb A F and Dhakal B 2014 Transients and evolution in NiTi *Experimental Mechanics* **54** 709-715

[43]   Benafan O, Noebe R D, Padula II S A, Brown D W, Vogel S and Vaidyanathan R 2014 Thermomechanical cycling of a NiTi shape memory alloy-macroscopic response and microstructural evolution *International Journal of Plasticity* **56** 99-118

[44]   Ye B, Majumdar B S and Dutta I 2009 Texture development and strain hysteresis in a NiTi shape-memory alloy during thermal cycling under load *Acta Materialia* **57** 2403-2417

[45]   Benafan O, Brown J, Calkins F T, Kumar P, Stebner A P, Turner T L, Vaidyanathan R, Webster J and Young M L 2014 Shape memory alloy actuator design: CASMART collaborative best practices and case studies *International Journal of Mechanics and Materials in Design* **10** 1-42

[46]   Hartl D J and Lagoudas D C 2007 Aerospace applications of shape memory alloys *Proceedings of the Institution of Mechanical Engineers, Part G: Journal of Aerospace Engineering* **221** 535-552

[47] Benafan O, Noebe R D, Padula II S A, Garg A, Clausen B, Vogel S and Vaidyanathan R 2013 Temperature dependent deformation of B2 austenite in a NiTi shape memory alloy *International Journal of Plasticity* **51** 103-121

[48] Benafan O, Noebe R D, Halsmer T J, Padula II S A, Bigelow G S, Gaydosh D J and Garg A 2016 Constant-strain thermal cycling of a Ni50. 3Ti29. 7Hf20 high-temperature shape memory alloy *Shape Memory and Superelasticity* 1-10

[49] Bourke M A M, Dunand D C and Ustundag E 2002 SMARTS - A spectrometer for strain measurement in engineering materials *Applied Physics Letters* **74** S1707

[50] Von Dreele R 1997 Quantitative texture analysis by Rietveld refinement *Journal of Applied Crystallography* **30** 517-525

[51] Liu Y, Xie Z and Van Humbeeck J 1999 Cyclic deformation of NiTi shape memory alloys *Materials Science and Engineering: A* **273–275** 673-678

[52] Miyazaki S, Otsuka K and Wayman C M 1989 The shape memory mechanism associated with the martensitic transformation in Ti·Ni alloys—I. Self-accommodation *Acta Metallurgica* **37** 1873-1884

[53] Otsuka K and Ren X 2005 Physical metallurgy of Ti-Ni-based shape memory alloys *Progress in Materials Science* **50** 511-678

[54] Yamauchi K, Ohkata I, Tsuchiya K and Miyazaki S (ed) 2011 *Shape Memory and Superelastic Alloys: Technologies and Applications* (Woodhead Publishing)

[55] Xie Z L, Liu Y and Van Humbeeck J 1998 Microstructure of NiTi shape memory alloy due to tension–compression cyclic deformation *Acta Materialia* **46** 1989-2000

[56] Wagner M F X and Windl W 2008 Lattice stability, elastic constants and macroscopic moduli of NiTi martensites from first principles *Acta Materialia* **56** 6232-6245

[57] Xie Z L and Liu Y 2004 HRTEM study of <011> type II twin in NiTi shape memory alloy *Philosophical Magazine* **84** 3497-3507

[58] Ezaz T, Sehitoglu H and Maier H J 2011 Energetics of twinning in martensitic NiTi *Acta Materialia* **59** 5893-5904

[59] Nishida M, Ii S, Kitamura K, Furukawa T, Chiba A, Hara T and Hiraga K 1998 New deformation twinning mode of B19′ martensite in Ti-Ni shape memory alloy *Scripta Materialia* **39** 1749-1754

[60] Benafan O, Noebe R D and Halsmer T J 2016 Static rock splitters based on high temperature shape memory alloys for planetary explorations *Acta Astronautica* **118** 137-157

[61] Benafan O, Garg A, Noebe R D, Bigelow G S, Padula S A, Gaydosh D J, Schell N, Mabe J H and Vaidyanathan R 2014 Mechanical and functional behavior of a Ni-rich Ni 50.3 Ti 29.7 Hf 20 high temperature shape memory alloy *Intermetallics* **50** 94-107

[62] Benafan O, Garg A, Noebe R D, Skorpenske H D, An K and Schell N 2017 Deformation characteristics of the intermetallic alloy 60NiTi *Intermetallics* **82** 40-52

[63] Ye B, Majumdar B S and Dutta I 2007 Texture memory and strain-texture mapping in a NiTi shape memory alloy *Applied Physics Letters* **91** 061918-061918-3

[64] Saburi T and Nenno S 1981 *Solid Phase Transformations* (Warrendale, PA, 1981) TMS-AIME

[65] Nicholson D E, Benafan O, Padula II S A and Vaidyanathan R 2017 Texture evolution during isothermal, isostrain and isobaric loading of polycrystalline shape memory NiTi *Applied Physics Letters* **In Review**

[66] Stebner A P, Brown D W and Brinson L C 2013 Young's modulus evolution and texture-based elastic–inelastic strain partitioning during large uniaxial deformations of monoclinic nickel–titanium *Acta Mater.* **61** 1944-1966

[67] Krishnan V B, Bewerse C, Notardonato W U and Vaidyanathan R 2008 A thermal conduction switch based on low hysteresis NiTiFe shape memory alloy helical springs *AIP Conference Proceedings: Advances in Cryogenic Engineering Materials* **986** 3-9

[68] Mehta A, Gong X Y, Imbeni V, Pelton A R and Ritchie R O 2007 Understanding the deformation and fracture of nitinol endovascular stents using *in situ* synchrotron X-Ray microdiffraction *Advanced Materials* **19** 1183-1186

[69] Miyazaki S and Wayman C 1988 The R-phase transition and associated shape memory mechanism in Ti-Ni single crystals *Acta metallurgica* **36** 181-192

[70] Krishnan V, Manjeri R M, Clausen B, Brown D and Vaidyanathan R 2008 Analysis of neutron diffraction spectra acquired in situ during mechanical loading of shape memory NiTiFe at low temperatures *Materials Science and Engineering: A* **481** 3-10

[71] Lukáš P, Šittner P, Neov D, Novák V, Lugovyy D and Tovar M 2002 R-phase phenomena in neutron diffraction investigations of thermomechanically loaded NiTi polycrystals *Materials science forum* (2002) Trans Tech Publ **404** 835-840

[72]   Manjeri R M 2009 Low temperature and reduced length scale behavior of shape memory and superelastic NiTi and NiTiFe alloys *University of Central Florida* Orlando, FL

[73]   Woracek R, Penumadu D, Kardjilov N, Hilger A, Boin M, Banhart J and Manke I 2014 3D mapping of crystallographic phase distribution using energy-selective neutron tomography *Advanced Materials* **26** 4069-4073

[74]   Qiu S, Krishnan V B, Padula II S A, Noebe R D, Brown D W, Clausen B and Vaidyanathan R 2009 Measurement of the lattice plane strain and phase fraction evolution during heating and cooling in shape memory NiTi *Applied Physics Letters* **95** 141906

[75]   Vaidyanathan R, Bourke M A M and Dunand D C 1999 Phase fraction, texture and strain evolution in superelastic NiTi and NiTi-TiC composites investigated by neutron diffraction *Acta Materialia* **47** 3353-3366

[76]   Vaidyanathan R, Bourke M A M and Dunand D C 1999 Analysis of neutron diffraction spectra acquired *in situ* during stress-induced transformations in superelastic NiTi *Journal of Applied Physics* **86** 3020-3029

[77]   Vaidyanathan R, Bourke M A M and Dunand D C 2001 Texture, strain, and phase-fraction measurements during mechanical cycling in superelastic NiTi *Metallurgical and Materials Transactions A* **32** 777-786

[78]   Von Dreele R B, Jorgensen J D and Windsor C G 1982 Rietveld refinement with spallation neutron powder diffraction data *Journal of Applied Crystallography* **15** 581-589

[79]   Cai S, Schaffer J E, Ren Y and Yu C 2013 Texture evolution during nitinol martensite detwinning and phase transformation *Applied Physics Letters* **103** 241909